Electron-Enhanced Atomic Layer Deposition (EE-ALD)

by

Zachary C. Sobell

BS, University of California Los Angeles, 2017

A thesis submitted to the

Faculty of the Graduate School of the

University of Colorado in partial fulfillment

of the requirement for the degree of

Doctor of Philosophy

Department of Chemistry

2022

Committee Members:

Dr. Steven George

Dr. Tanja Cuk

Dr. Michael Marshak

Dr. Niels Damrauer

Dr. Michael McGehee

ABSTRACT

Sobell, Zachary C. (Ph.D., Chemistry; Department of Chemistry)

Electron-Enhanced Atomic Layer Deposition (EE-ALD)

Thesis directed by Professor Steven M. George

As dimensions in semiconductor manufacturing continue to shrink, new deposition techniques are needed. To address the needs of next-generation devices a suite of deposition and etching processes are required. Thermal atomic layer deposition (ALD) has played a growing role in semiconductor manufacturing for several decades, but the thermal energy needed for ALD is often incompatible with back end of line (BEOL) manufacturing constraints. ALD relies on a series of sequential self-limiting surface reactions, often broken into an (A) and (B) half reactions. Electron-enhanced ALD (EE-ALD) utilizes low energy electrons as an ALD (B) reactant to minimize the deposition temperature and open new dimensions of thin film growth.

This dissertation first focuses on Co EE-ALD with cobalt tricarbonyl nitrosyl ($Co(CO)_3NO$) and low energy electrons from an electron gun. The electron gun was later replaced by an in-house designed hollow cathode plasma electron source (HC-PES) as an upgraded electron source. The HC-PES allowed for a >10x reduction in cycle times, >1000x increase in electron flux, and a >10x increase in deposition area over the electron gun. The HC-PES is also chemically insensitive and can operate at pressures of several mTorr. A comparison of Co EE-ALD with the electron gun versus with the HC-PES was made.

The superior properties of the HC-PES allowed for the introduction of a reactive background gas (RBG) which enabled the deposition of high-quality, low resistivity TiN from

tetrakisdimethylamido titanium (TDMAT) and ammonia (NH_3) as the RBG. The NH_3 RBG is hypothesized to interact with the low energy electrons to create radicals near the surface. These radicals greatly enhance film composition by creating volatile compounds with the impurities. In situ Auger Electron Spectroscopy (AES) was used to probe film compositions for TiN grown with and without NH_3 RBG. AES confirms a remarkable decrease in carbon content with the use of NH_3 RBG. Ex situ XPS confirmed the film purity with a C and O content of < 2 at% each.

ACKNOWLEDGEMENTS

This research was performed as part of the ASCENT (Applications and Systems Driven Center for Energy-Efficient Integrated Nanotechnologies) SRC JUMP Center. This work was supported in part by the Semiconductor Research Corporation (SRC) and DARPA. This work was also partially supported by the Naval Research Laboratory base program. I would like to thank Kenneth Smith and Don David from the University of Colorado Integrated Instrument Development Facility for their construction of the HC-PES and computer interfacing. I would also like to thank Dr. Sadegh Yazdi and the Facility for Electron Microscopy of Materials at the University of Colorado at Boulder (CU FEMM) for the TEM sample preparation and high-resolution STEM and STEM-EDS mapping and analysis. I would like to acknowledge Woodruff Scientific for the modeling and construction of the electron steering optics and thank Blaine Johs from Filmsense and Marcel Junige for fruitful discussions regarding ellipsometric modeling. I would like to thank Andrew Cavanagh for performing XPS analysis.

In addition:

Thanks to my advisor Dr. Steve George for his insight and direction,

Thanks again to Dr. Andrew Cavanagh for always having a fresh perspective,

Thanks to all the George Group members for their companionship and assistance,

Thanks to my collaborators who have kept my research relevant,

Thanks to my family for believing in me, and

Thanks to my partner, Jess, for her endless support.

Table of Contents

List of Tables

List of Figures

1 Introduction

1.1 Chemistry

1.1.1 Atomic Layer Deposition

Atomic layer deposition (ALD) is a precision deposition technique. It relies on a series of self-limiting surface reactions to deposit a thin, conformal, pinhole-fee film. The self-limiting nature of ALD is responsible for the high conformality, low roughness, and several other beneficial aspects of ALD.[1-3] As a precursor (A) is introduced into the reaction chamber it reacts with any available reactive surface sites. As those sites are consumed the remaining precursor will find any available reactive surface sites to occupy. Given that precursor A will not react with itself, this allows for an excess of precursor to be introduced while only depositing one monolayer of material. The next precursor (B) may be introduced after precursor A has had sufficient time to react with all available surface sites and for the remaining precursor A to be pumped from the chamber. Sufficient pumping ensures there will not be a gas-phase reaction of precursor A and precursor B. Such a gas-phase reaction leads to CVD, and negates the benefits of ALD. Precursor B should behave in the same way as precursor A, reacting with all available surface sites (Figure 1-1)

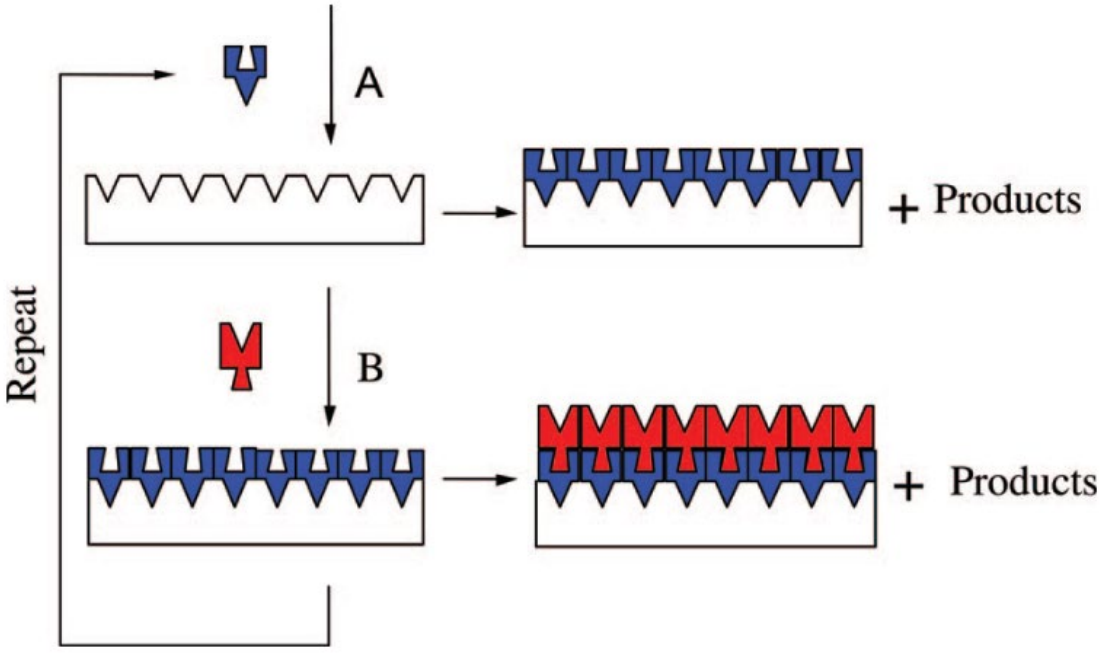

Figure 1-1. Schematic representation of ALD using self-limiting surface chemistry and an AB binary reaction sequence.[1]

before being pumped from the reaction chamber. This behavior ensures that, given a sufficient supply of precursor, all available reactive surface sites will be consumed on each half reaction. This in turn ensures that the deposition proceeds at a uniform rate over the whole surface, regardless of topography, leading to a uniform thickness of deposited material over the whole surface. The excellent conformality of ALD allows for high aspect ratio (HAR) structures to be coated in a way that no other deposition process can match.[1] The higher the aspect ratio the longer the cycle times may be. More time is required for the precursor to diffuse into the HAR structures during the precursor dosing and more time is required for excess precursor to be pumped from the HAR structures during the pumping or purging phase. The self-limiting reactions of each precursor also allow for Ångstrom-level thickness control. Since one monolayer of material is deposited each half-reaction, the deposition thickness can be precisely

controlled down to a monolayer, usually on the order of a few Ångstroms. Each cycle deposits the same thickness as the last, regardless of precursor dose, so the thickness endpoint can be achieved repeatably. The self-limiting reactions lead to smooth films as well. Any valleys will tend to be filled in from the sides as the conformal film deposits leading to smoother films as the deposition continues.[4]

Most ALD chemistries are based on binary processes.[5] One such process is alumina (Al_2O_3) deposition from trimethyl aluminum (TMA) and water (H_2O). The strong Al-O bonds formed in the reaction create a large negative ΔH which drives the reaction forward.[1, 6] The earliest reports of alumina ALD date to the 80s and 90s.[7] Alumina ALD can be carried out over a wide range of temperatures, but high-quality films are typically grown at T > 100 °C. Alumina ALD proceeds according to the reactions

$$\text{(A)}\quad AlOH^* + Al(CH_3)_3 \rightarrow AlOAl(CH_3)_2^* + CH_4 \qquad \text{(Eq. 1.1)}$$

$$\text{(B)}\quad AlCH_3^* + H_2O \rightarrow AlOH^* + CH_4 \qquad \text{(Eq 1.2)}$$

where * denotes a surface species.[1] In Eq. 1.1 a hydroxyl terminated surface is exposed to trimethyl aluminum (TMA). A lone pair on the surface -OH oxygen attacks the electropositive Al center in TMA forming a strong Al-O bond. Surface -OH protons are transferred to the $-CH_3$ ligands on the reacted TMA to make CH_4 which is pumped out if the chamber with excess unreacted TMA. This continues until no more -OH groups are available for reaction at which point the chemistry stops, or self-limits. The result of Eq. 1.1 is a surface covered primarily in CH_3 groups from the TMA. In Eq 1.2 the $-CH_3$ terminated surface is exposed to water (H_2O). The Al-CH_3 bonds are cleaved in favor of more strong Al-O bonds, again through attack by the O in H_2O. This continues until there are no more available $-CH_3$ groups for reaction. A proton

from the introduced water reacts with the methyl groups on the surface, and again leaves as CH_4.The surface returns to the starting state shown in Eq. 1.1, namely -OH terminated. The reaction can be run in this way utilizing separate A-B reactions until the desired thickness is achieved.

ALD has many advantages, but it is also a slow process. The precursors used often have a high sticking coefficient and are hard to pump from the chamber leading to long cycle times. The deposited thickness per deposition cycle (growth per cycle, GPC) is often low which further slows the deposition process down. ALD is a thermal process, and often the thermal energy needed to afford a clean reaction product requires high temperatures. Given that one of the major applications of ALD is semiconductor device manufacturing these high temperatures can be detrimental. A non-thermal process with similar desirable traits would be a welcome tool in semiconductor manufacturing. One possibility is the addition of electrons as a reactant to drive the breaking of bonds rather than reliance on thermal energy.

1.1.2 Focused Electron Beam Induced Deposition and Electron-Matter Interaction

Focused electron beam induced deposition (FEBID) is the most closely related field of deposition to EE-ALD. FEBID typically proceeds in a high vacuum environment in a modified scanning electron microscope (SEM).[8-9] The high energy electrons (10s to 100s of keV) emitted from the SEM filament are used to dissociate adsorbed precursor molecules and induce deposition.[10] The precursor is injected into the apparatus by a gas injection system (GIS) directed at the substrate under the electron beam (Figure 1-2).

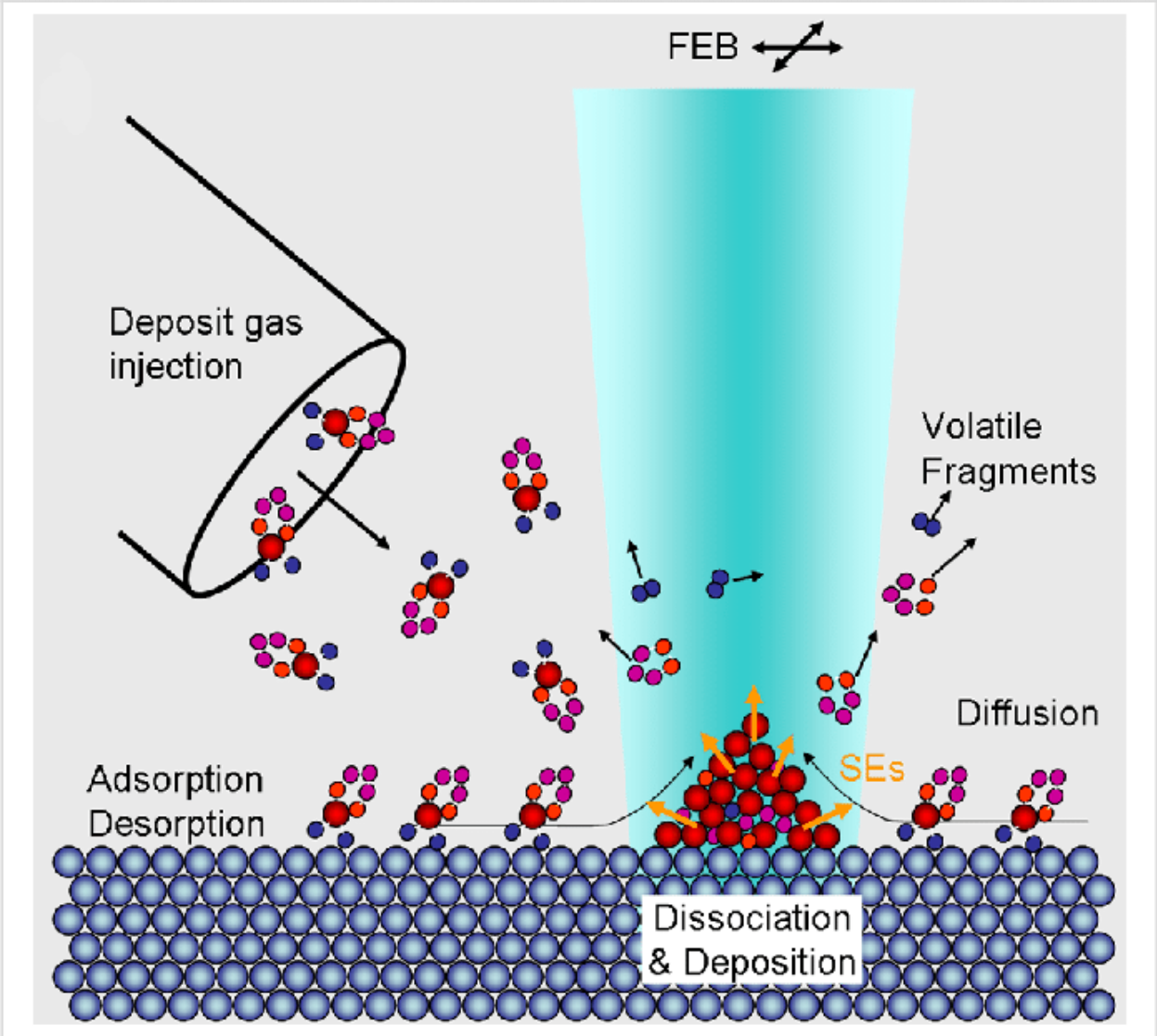

Figure 1-2. Sketch of focused electron beam induced deposition (FEBID). This is an electron-assisted chemical growth technique giving rise to high-resolution patterning in a single step. The precursor molecules are locally dissociated by a scanning electron microscope.[11]

Steering and focusing optics are used to raster the electron beam to direct deposition in a direct-write fashion. The electron beam can be rastered over an area to create thin films, or be directed to create more complicated 3D structures in a process akin to 3D printing.[11-15] The high energy electron beam can be focused tightly, reducing the spot size of the beam, allowing for feature

deposition on the scale of nm.[16] This enables direct write technology for specialized uses like EUV mask repair.[17-18] FEBID is often used before FIB cutting samples for cross sectional SEM (XSEM) to quickly deposit an SiC_xO_y or Pt(C) mask to protect the sample from accidental ion beam milling. This is accomplished by leaking an Si or Pt containing precursor into the SEM while the electron beam is on.[19-21] As the electron beam interacts with the introduced precursors they are decomposed, leaving a deposit behind wherever the beam strikes. For simple molecules (e.g. $Fe(CO)_5$) this can lead to pure deposits, but for most molecules the interaction leads to incomplete decomposition and highly impure deposits.[8, 13, 20, 22] The Si deposited this way is actually SiO_xC_y, and the Pt is heavily contaminated with C. This is due to nonselective bond breaking by the e-beam. Electron bombardment alone are not sufficient to remove C and O from many films after those elements are incorporated post e-beam irradiation.[23-24] Slow, direct write deposition and highly impure deposits are two of the main hurdles to FEBID being a widely adopted deposition tool.

The primary energy electrons are thought to not be the primary driver of decomposition due to the broad deposits that result from highly focused electron beams.[11] Instead, low energy (0-30 eV) secondary electrons created at the surface by the high energy primary electron beam are thought to be the primary drivers of FEBID growth.[11-12] There are several proposed mechanisms for this that fall broadly under two categories; electron stimulated desorption (ESD) and electron induced decomposition (EID). Two main mechanisms for ESD are the Menzel-Gomer-Redhead (MGR)[25] mechanism (Figure 1-3)

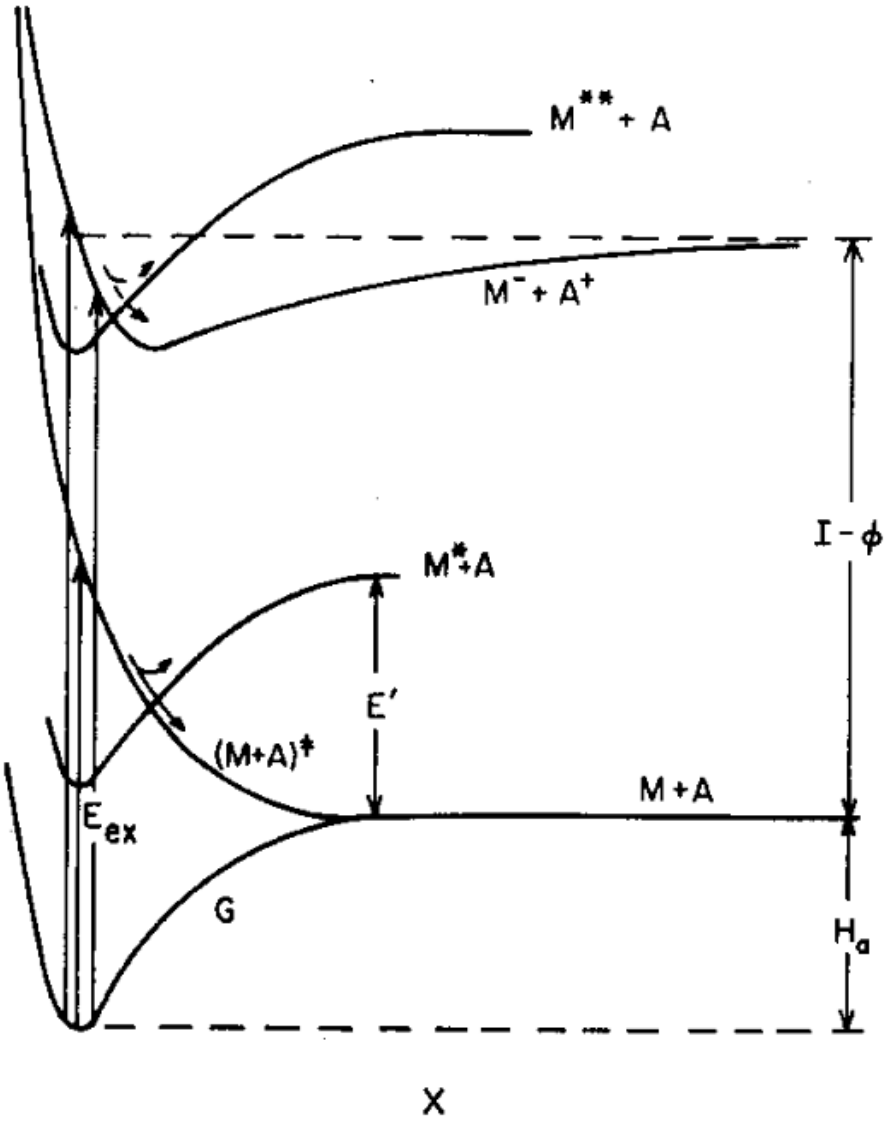

Figure 1-3. Potential-energy diagram for adsorption. Bonding state M+A, antibonding state $(M+A)^{‡}$, ionic state M-+A+. Two excited copies of the bonding state M*+A, and M**+A, are shown intersecting the antibonding and ionic curves, respectively. Vertical arrows indicate some of the possible transitions, and dashed arrows the subsequent possibilities for desorption in the excited states or transitions to the bonding state. E_x is the excitation for the transition to the antibonding state indicated by the middle vertical arrow, and E' the electronic excitation of the system after transition to the bonding curve M*+A. I, ionization potential of A, Φ, work function of M.[25]

and the Auger mechanism, or Knotek-Feibelman (KF)[26-27] mechanism (Figure 1-4).

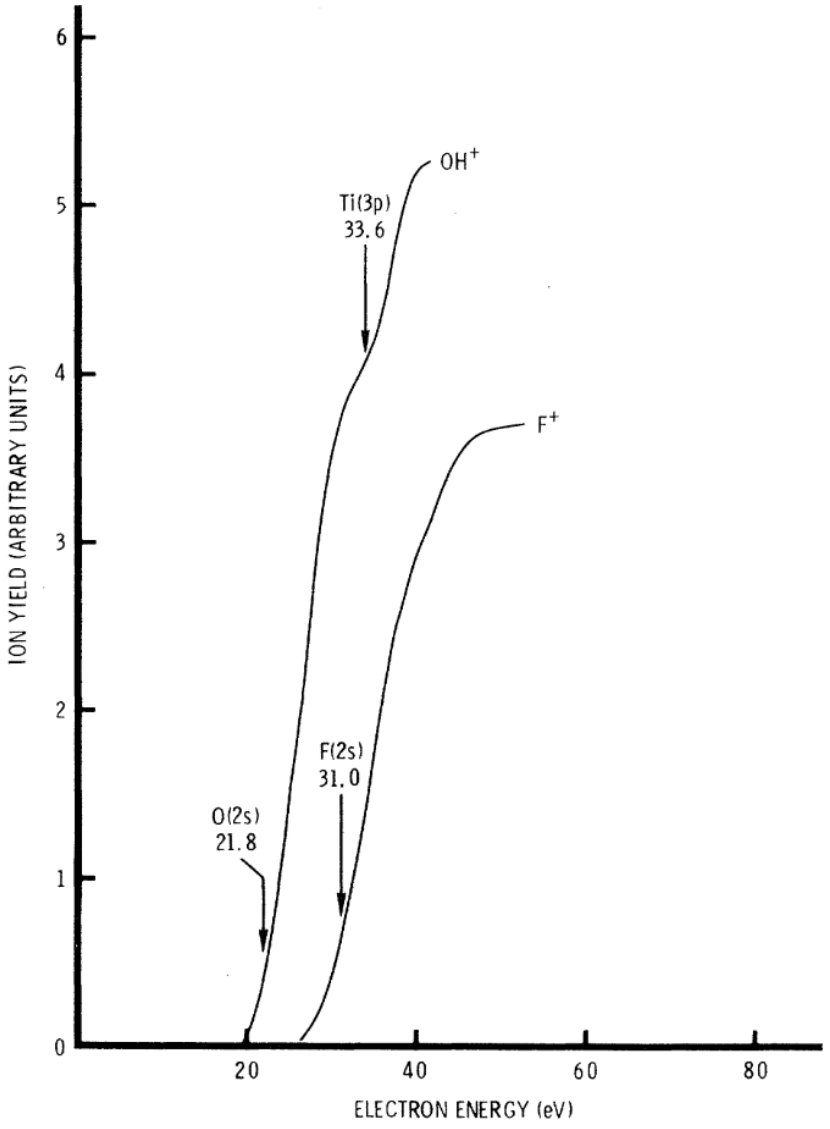

Figure 1-4. OH^+ and F^+ ion yield vs incident electron energy for TiO_2 surface. The arrows denote the LEELS peak energies corresponding to core-hole excitations. Note that OH^+ thresholds occur at both the O(2s) and Ti(3p) excitation energies.[27]

The MGR mechanism describes the promotion of a bonding electron to an antibonding or nonbonding state by an energetic electron. As a result, the effective potential between the surface atom and the bulk solid becomes repulsive and the surface atom desorbs. The relatively small desorption cross sections observed for hydrogen, oxygen, carbon dioxide, and barium on

tungsten are used to argue that there is an electronic transition to a repulsive state that can lead to desorption, but a competing relaxation pathway gives rise to the observed desorption cross sections. The KF theory was described as a direct refutation of the MGR theory. The KF theory cites the desorption of highly electronegative elements such as O, which typically bind with a -1 or -2 charge, as O^+ as problematic for the MGR theory. Additionally, the authors of the KF paper do not see desorption onset for O on TiO_2, WO_3, or V_2O_5 at the MGR predicted 15-20 eV electron energy. The KF process was created to explain these observed differences.

The KF process is hypothesized to proceed by an Auger process, described as follows. An incident electron knocks out a core electron from an atom on or near the surface. This electron vacancy is filled by an electron in a higher energy shell. To conserve energy, another electron, typically a valence electron, must be ejected from the system with energy equal to the difference between the inner shell electron and the higher energy shell electron, minus the binding energy of the ejected electron. In the case of TiO_2 there are no Ti valence electrons. If a core hole is created on a Ti atom both electrons required for the Auger process may be bonding electrons. This leaves a neutral surface O, which is likely to desorb. Furthermore, a double Auger mechanism may explain the loss of O^+ directly. The KF hypothesis cites the ESD energy dependance that corresponds closely with core electron energies as evidence for an Auger-like mechanism.

EID brings four other mechanisms into the picture. For a more complete discussion of the topic see Thorman et al.[11] In brief, the two most fundamental mechanisms are: dissociative electron attachment (DEA), where a very low (~0 eV) electron is captured, leading to a repulsive state and dissociation, similar to the MGR mechanism, and dissociative ionization (DI), where an incident electron knocks a bonding electron out of the system leading to another repulsive state

and dissociation. Of note is the operating window for the four processes, namely < 100 eV. This is the general range of secondary electron energies, not the energies of the primary beam in FEBID. It is worth noting that the energy overlap between maximal secondary electron yield and the DEA process energy window is the greatest.

Low energy electrons of ~100 eV interact with matter more readily than high energy electrons. This can be seen in several situations. Firstly, the so-called electron universal curve compares electron energy and electron mean free path in several materials.[28] The electron mean free path is shortest at electron energies of ~100 eV. This means that at very low or very high energies there is a smaller chance that the electron will interact with any given atom. Another well-known instance this phenomenon pops up is in mass spectrometry. The electron energy used in the ionizer region of a mass spectrometer is ~100 eV due to the maximal electron cross section for ionization occurring around this energy.[29] This further explains the observation that the low energy secondary electrons are the primary drivers of deposition in FEBID.

1.1.3 Electron-Enhanced Atomic Layer Deposition and Chemical Vapor Deposition

Given that the low energy (<100 eV) electrons are the primary drivers of electron induced deposition, EE-ALD was developed to expand upon the FEBID technique. Initially an electron flood gun and later a hollow cathode plasma electron source (HC-PES) was used to flood the surface with low energy electrons directly. This technique is different from FEBID in several ways. Firstly, as mentioned, low energy electrons were used directly. Secondly, the half-reactions were split like a thermal ALD process. This means that the precursor adsorption was separated from the ESD in an A-B manner (Eq. 1.1 and Eq 1.2). This allows for more conformal growth in the limit of long electron exposures and much faster deposition over a macroscopic area. Silicon EE-ALD from disilane (Si_2H_6) is a model system for EE-ALD.[30] Si dangling

bonds present during steady state Si deposition act as an adsorption site for disilane in step A (Figure 1-5).

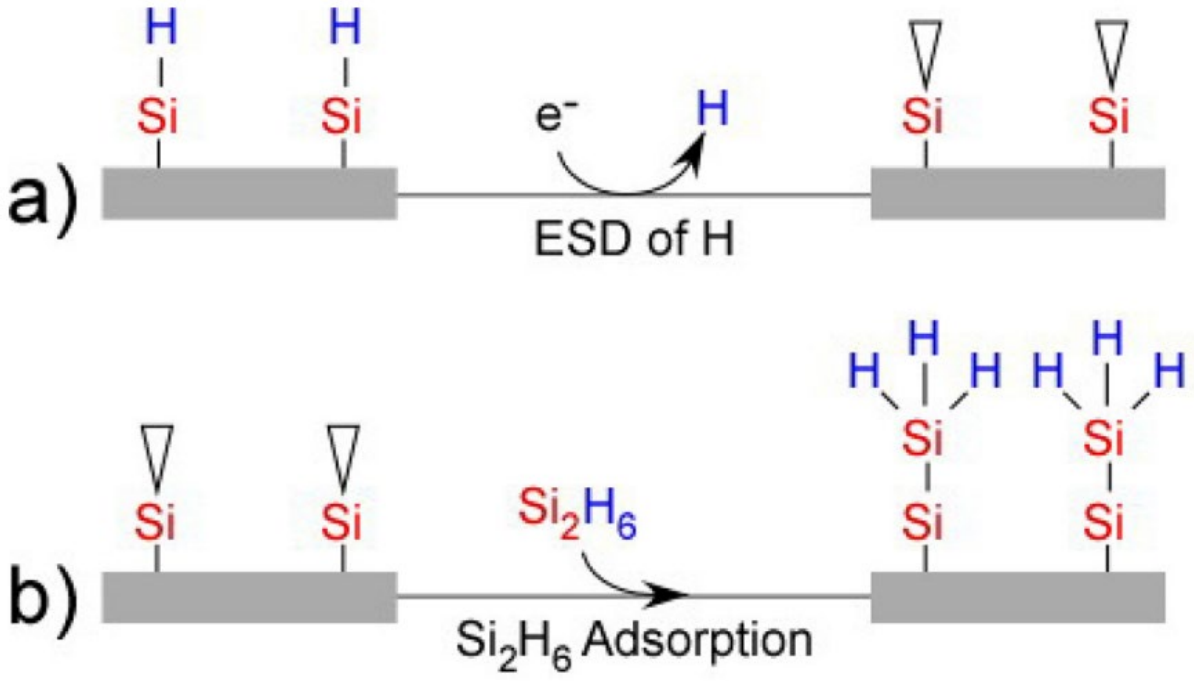

Figure 1-5. Proposed growth mechanism for Si EE-ALD using disilane as the reactant.[30]

Growth rate calculations suggest the disilane dissociatively adsorbs, leaving a H-terminated surface. Excess disilane is pumped from the chamber. In step B low energy electrons desorb the surface H through an ESD process leaving behind Si dangling bonds. The dangling bonds represent the starting surface and allow the entire deposition process to be repeated as needed. Without the removal of the surface H in step B no disilane adsorption can occur. The highly reactive dangling bonds left after the ESD process are a crucial driver of the deposition. This process bridges the gap between ALD and FEBID, offering several advantages of both while minimizing many disadvantages.

Disilane is a simple molecule, and there is no possibility of unwanted fragmentation.[30] More complicated molecules like tetrakisdimethylamido titanium (TDMAT) have many bonds that can be broken, leading to the buildup of carbonaceous material in the films, greatly affecting purity. This is well documented in FEBID as well. [8, 13, 20, 22] TDMAT is an appealing molecule for Ti-based film deposition due to its wide availability, high vapor pressure, and lack of halogen or oxygen atoms. One possible solution to the deposition of highly impure films is the introduction of a reactive background gas (RBG) into the deposition chamber during at least the electron exposure.[19, 31-33] The interaction between the low-energy electrons and the RBG is hypothesized to create radicals, especially at or near the surface, which aid in the removal of unwanted atoms in the film. The RBG must be chosen carefully because it can become incorporated into the film as well. For example, TDMAT and low energy electrons with an ammonia (NH_3) RBG cleans up almost all the C produced by unwanted ESD reactions while ensuring the resulting TiN film remains fully nitridated. The H from NH_3 is likely fully desorbed and therefore not incorporated into the film. Radiolabeling experiments would determine whether N from NH_3 or TDMAT is incorporated into the film. An O_2 RBG will also remove C from the film, but it will remove N as well, and the O will also be incorporated into the film resulting in a high quality TiO_2 film.

Not all systems show strong adsorption of the precursor molecules under EE-ALD with RBG conditions. This results in extremely low growth per cycle (GPC). One possible remedy for this is the simultaneous introduction of RBG, electrons, and precursor into the chamber. To control growth and allow sufficient time for the RBG and electrons to fully affect the desired change in the film the precursor can be pulsed against a background of electrons and RBG. This process does not share the advantages of ALD such as precise thickness control and conformality

but does allow for the rapid deposition of myriad materials from a limited number of precursors and RBGs. Like thermal CVD processes, EE-CVD has two limiting modes.[34] The growth may be limited by the mass transfer of precursor onto the sample in the limit of high electron flux and low precursor exposure. In this regime, the electrons decompose the precursor as fast as it adsorbs onto the substrate. As the precursor exposure increases a new regime predominates. In this regime the electron beam will not be able to decompose the precursor as fast as it impinges on the surface and some of the precursor molecules will approach the substrate, not find an open adsorption site, and leave. EE-ALD is discussed in great detail in Sections 2, 3, and 4.

1.2 Equipment

The reaction vessel has evolved significantly since the beginning of this dissertation.[35-36] When this project began the reaction vessel was a UHV chamber with a base pressure of $\sim 5 \cdot 10^{-10}$ torr. The electron source was a hot filament electron gun with an electron current measured at the sample of 10s of μA. A load lock was used to minimize air exposure during sample loading and unloading. The sample stage platform faced the load lock, and the sample was transferred to the platform with a sample transfer arm. The electron gun was moved in front of the sample stage platform with a manual z-actuator. Electron exposures and purge times were several minutes, due to the low flux of the electron gun and the extreme sensitivity of the electron gun filament to contamination while warm. The UHV environment was necessary to ensure minimal unwanted adsorbates on the electron activated surface post electron exposure due to these long cycle times. The electron gun is discussed in greater detail in Section 2.

The electron gun suffered reliability issues due to precursor deposition on the filament despite the aforementioned precautions, and so it was replaced with a more robust hollow cathode plasma electron source (HC-PES) (Figure 1-6).

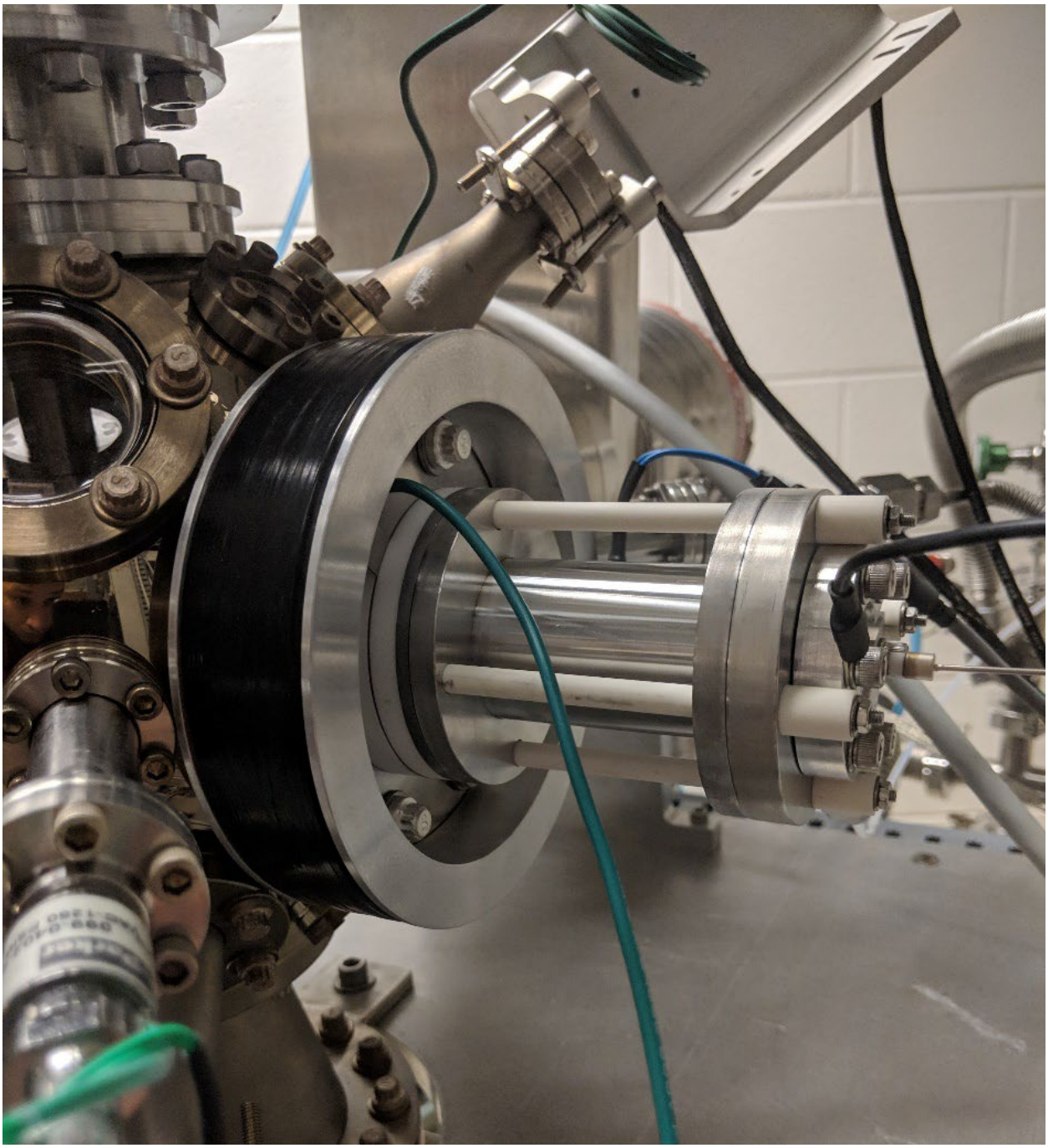

Figure 1-6. Newly installed HC-PES with first generation electron optics. Note the precursor dosing valve in the lower left and the in situ ellipsometer mounting bracket in the upper right.

The HC-PES was too large to be moved in line with the sample stage platform, so it was mounted behind it. The sample stage assembly was then mounted on a rotating flange. The

flange was sealed with two graphite-impregnated Teflon seals. Due to the rotation, the seals leak atmosphere into the vacuum at an unacceptable rate. To mitigate this, the seals were differentially pumped. The first seal was exposed to atmospheric pressure on the outside. In between the two seals was a cavity pumped with a small ion pump. This ion pump removed any leaked species from the cavity between the two seals, minimizing the pressure differential between the outside of the inner seal and the inside of the reaction chamber. This produced a pressure rise on rotation that was below the detection limit of the chamber instrumentation (Figure 1-7).

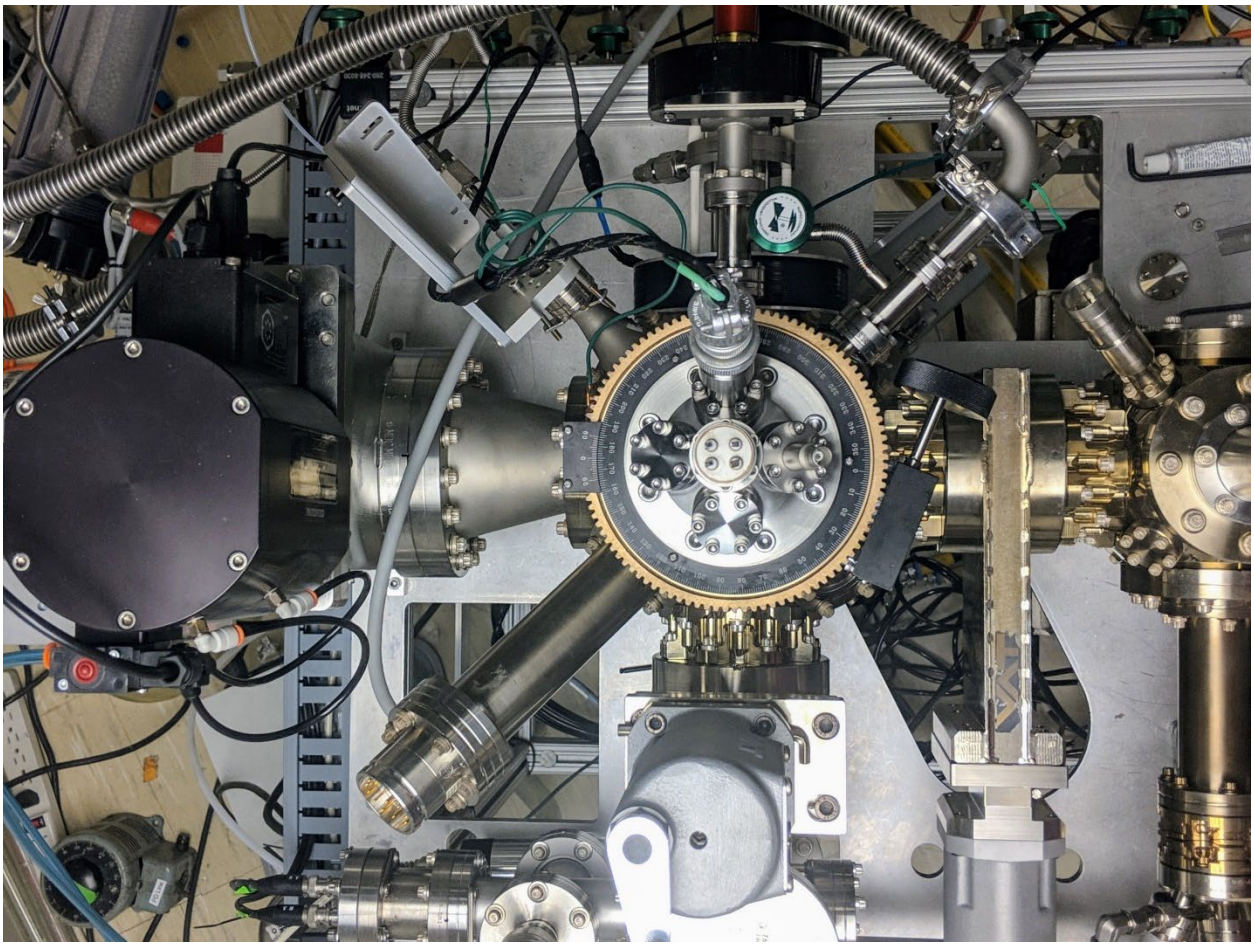

Figure 1-7. Top-down view of the reactor used in this work before the installation of the final electron optics. Turbopumps at 9 O'clock, ellipsometer mount at 10:30, HC-PES and rotating stage ion pump at 12, Auger chamber at 3, load lock at 6, RGA mount at 7:30, and rotating sample stage center.

The HC-PES has electron fluxes measured at the sample ~1000 times higher than the electron gun (Figure 1-6). This reduces electron exposure times by an equivalent amount. The HC-PES was also chemically insensitive, which reduced the need for lengthy purge times. These factors together reduce the cycle times from 10s of minutes to 10s of seconds or shorter. The HC-PES is sealed with rubber O-Rings to allow for easy disassembly and cleaning. These seals create small leaks into the reaction chamber. The base pressure of the chamber is now almost an order of

magnitude higher than when it was used with the electron gun. The rate of adsorption of gasses onto the sample is directly proportional to pressure. A 10 fold increase in pressure is negated by a 10 fold decrease in cycle time. Given the decrease in cycle times with the HC-PES is greater than 10 fold the overall contamination from residual gasses in the chamber is decreased.

Eventually a reactive background gas (RBG) was introduced into the chamber during the entirety of the deposition cycle. This was only possible with the HC-PES and its chemical insensitivity and ability to run at pressures of several mTorr. The RBG drastically decreased the level of impurities in deposited films and allowed for compositional tuning by changing the RBG and maintaining the same precursor. The HC-PES is discussed in greater detail in Section 3 and the use of reactive background gas is discussed in greater detail in Section 4.

1.3 Characterization

1.3.1 Ellipsometry

Ellipsometry was the primary tool used in this work for determining film thickness and some film properties. In situ real time ellipsometry was performed with a 4-wavelength ellipsometer from Filmsense (FS-1). Modeling was performed with the Filmsense software package (FS-1 for Windows) to determine film thickness, resistivity, and optical constants n (refractive index) and k (extinction coefficient). The four wavelengths of the in situ ellipsometer were 465 nm, 525 nm, 595 nm, and 635 nm. The beam angle was ~ 54 degrees as defined by the reactor window geometry.

Ellipsometry utilizes the change in polarization between an emitted beam (source) of known polarization and a detector after reflecting the beam obliquely off a sample of interest. The change in polarization can be defined as

$$\rho = \frac{R_P}{R_S} = \tan(\psi)\, e^{i\cdot\Delta} \qquad \text{(Eq. 1.3)}$$

where R_p is the change of polarization for p-polarized and R_s is the change of polarization for s-polarized light (Figure 1-8).[37]

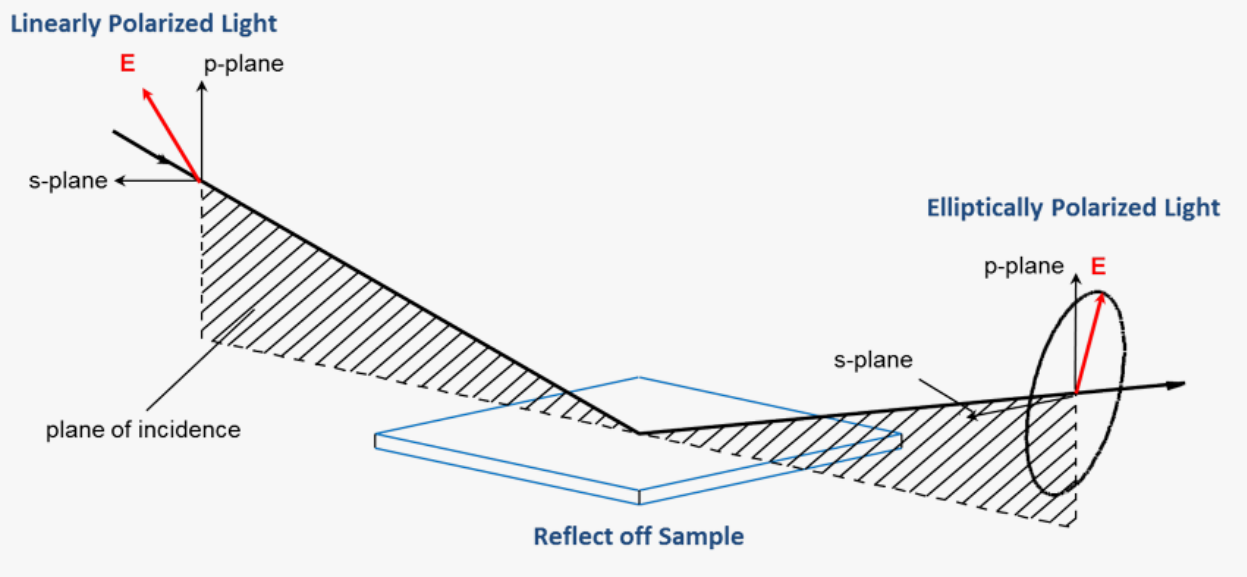

Figure 1-8. Representation of the change in polarization in the s- and p-plane of a linearly polarized light beam after interacting with a sample.[38]

This ratio can further be defined to include Psi and Delta, the amplitude ratio and phase difference, respectively. As the polarized light from the source is reflected off the sample the polarization angle (phase) changes, as does the light intensity (amplitude). The phase changes due to different solutions to Maxwells equations at the air-sample interface for horizontally and vertically polarized light, and the amplitude changes due to absorption of light by an absorbing film. Using physics beyond the scope of this introduction a model of the film can be constructed which explains the phase and amplitude changes. One such model is the so-called Drude model, which accounts for the interaction of polarized light with the free electrons in a metallic conductor. By careful modeling of the absorption of low energy photons the Drude model can

provide estimates of sample resistivity for metallic films.[9, 39-40] There is some difficulty in modeling the Drude absorption with only four discrete wavelengths as is the case for the in situ ellipsometer, but the data gathered from the FS-1 generally agree closely with the resistivity data gathered from other instruments, including 4-point probe.

Ex situ ellipsometric measurements were taken with a spectroscopic ellipsometer (M-2000, J.A. Woollam) with a wavelength range of 240 to 1000 nm. The large range of low energy frequencies from the M-2000 is important to fully capture the Drude adsorption and create an accurate model for the resistivity of metallic samples. The data from the M-2000 was analyzed in the accompanying CompleteEASE software. The default incident angle was 70°, however in practice the incident angle was varied from 60° to 80° for variable angle spectroscopic ellipsometry (VASE) to allow more accurate model fitting.

1.3.2 Auger Electron Spectroscopy

Auger Electron Spectroscopy (AES) was used to determine in situ surface composition. The AES instrument used in this work was a microCMA (RBD Instruments) with a primary beam energy of 3 keV. Data was collected from 100 to 800 eV. AES measurements involve accelerating an electron beam toward the sample of interest at high energy. The primary electron beam has a chance to eject a core electron on impact with the material being bombarded. This vacancy must be filled. An electron from a higher lying orbital can fall to fill this vacancy. To conserve energy, another electron can be ejected from the atom. The ejected electron will have a characteristic energy depending on the atomic identity, the energy level of the core electron initially knocked out, and the energy level of the energy-conserving electron. The energy of the ejected electron can be written as

$$E_{Eject} = E_A - E_B - E_C \quad \text{(Eq. 1.4)}$$

where E_A is the energy level of the core electron, E_B is the energy level of the electron which fills the core state, and E_C is the energy level of the ejected electron, all with respect to vacuum.[41] X-ray notation is often used to describe the origin of the electronic transitions that give rise to an AES peak. Shells with a principal quantum number (n) of 1, 2, and 3 are assigned letters K, L, and M. Electrons A, B, and C (Eq. 1.4) are assigned a letter from x-ray notation corresponding to their orbital of origin, for example an oxygen KLL peak. The inelastic background of an AES scan increases as the sampled energy increases, resulting in small, often hard to measure peaks from Auger transitions. To create a flatter background from which to measure peak heights AES data is reported as d(N)/dE versus electron energy.

AES is a surface sensitive technique.[41] The interaction volume of the primary beam with the sample of interest is large, on the order of a few microns (Figure 1-9).

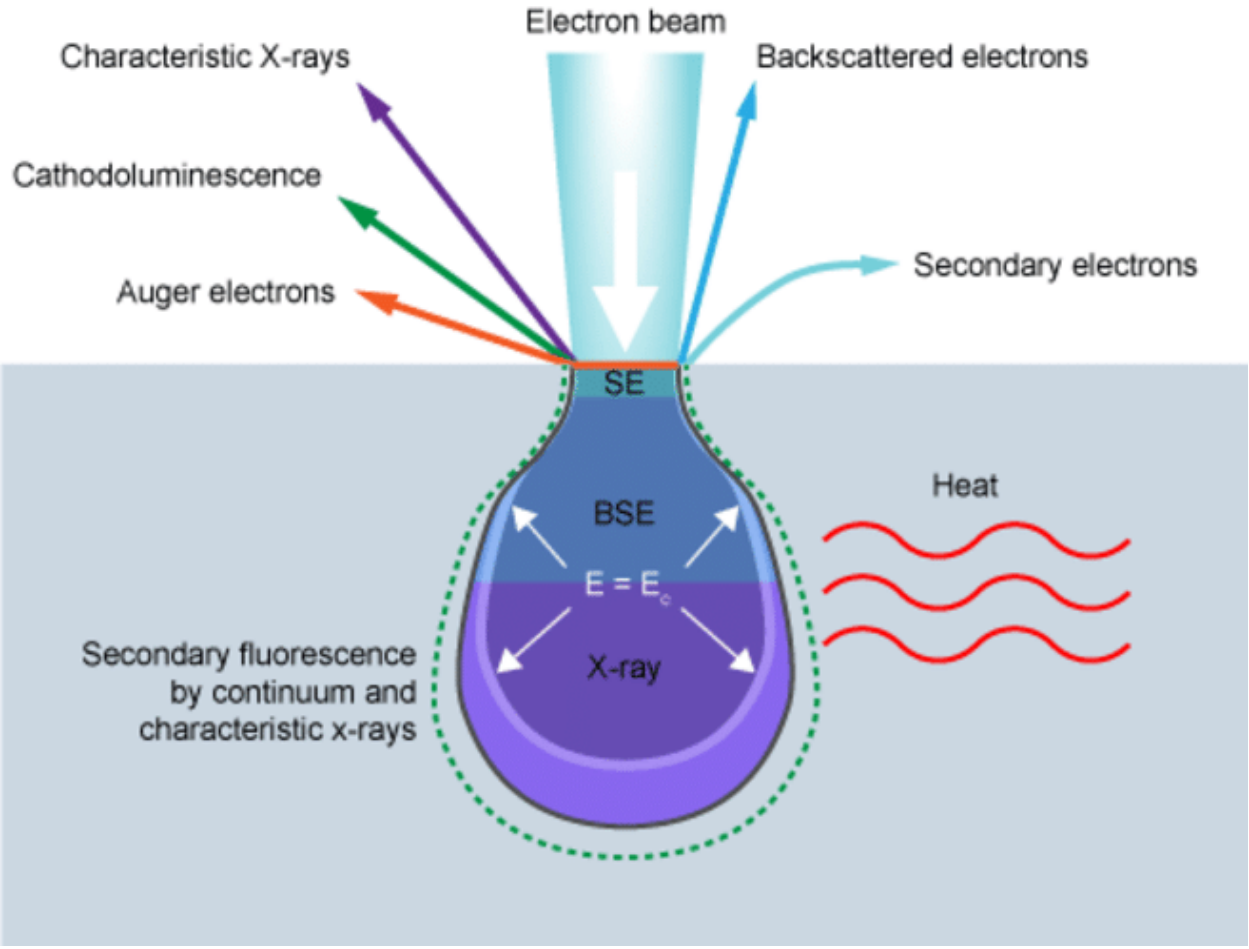

Figure 1-9. Interaction volume of a focused electron beam on a sample.[42]

This is because the high energy primary beam has a large mean free path. The Auger electrons are low energy, on the order of a few hundred eV. They have a much shorter mean free path, so only the electrons created near the surface can make it to the analyzer. This allows for sampling of the top few nm of a film. In practice, the AES used in this work had an attenuation length of ~3 nm.

1.3.3 X-Ray Reflectivity

X-ray reflectivity (XRR) was used to determine film thickness, roughness, and density for some films and multilayers grown by EE-ALD.[43] XRR requires uniform film properties over

the beam spot size. The beam is narrow, but due to the shallow incidence angle the beam spot size is several cm long. Samples grown by EE-CVD were typically not uniform enough to be properly measured by XRR. The X-ray tool used for this work was a Bede D1 from Jordan Valley Semiconductors with radiation from Cu Kα (λ=1.540 Å). The X-ray tube filament voltage was 40 kV and the current was 30 mA. X-rays with a wavelength of 1.540 Å are separated by a monochromator, and directed toward the sample at an angle ϕ. The specular reflection is detected at the same angle ϕ. The angle ϕ is typically scanned from 0 to 7000 arcseconds, or ~1.94° (Figure 1-10).

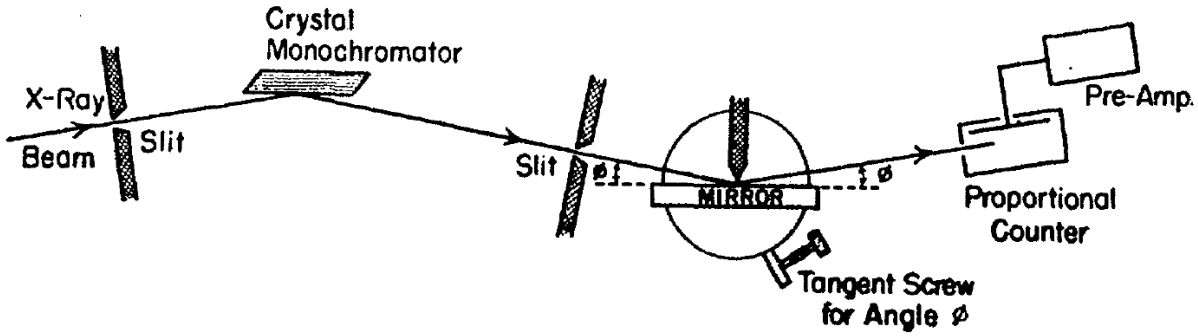

Figure 1-10. Diagram representing the experimental XRR geometry in this work.[44]

The intensity of the detected x-rays first reaches a global maximum at the so-called critical angle, or the angle of total internal reflection, then decreases in intensity in an oscillating manner as the incident angle ϕ increases. The critical angle corresponds to the maximum reflected x-ray intensity. The critical angle can be used to calculate the electron density of the material, and therefore the gravimetric density if the chemical formula of the material is known. The oscillating intensity as the angle ϕ increases are called Kiessig fringes. They arise due to constructive and destructive interference in the film increasing and decreasing the reflected X-

ray intensity respectively. The fringes allow the film thickness to be modeled. The frequency of the fringes increases as the film thickness increases. Film stacks will produce overlapping fringes, often with different frequencies. The film thicknesses as measured by ellipsometry and XRR are typically in excellent agreement. Non-uniform films may have small measured thickness discrepancies between XRR and ellipsometry based on the area of the film measured. Surface and interfacial roughness also affect the reflected x-ray intensity. Rougher films will scatter more X-rays, decreasing the intensity of the specularly reflected x-rays as the angle ϕ increases faster than smooth films. As such, XRR can be used to model interfacial roughness.

The critical angle, fringe spacing, and intensity decay can be used to model the film or film stack. A genetic algorithm was used to evolve the XRR model to reach a minimal fit error for the experimental data (Jordan Valley REFS). An estimate of the film stack and film thicknesses was used as a starting point for the algorithm. 500-2000 generations were used to fit the model to the data. Densities were reported relative to the identities of the films in the model. Non-uniform films typically had higher fit errors than uniform films and were often not able to be modeled. Films that showed no Kiessig fringes were not modeled using the XRR modeling software.

1.3.4 X-Ray Diffraction

X-ray diffraction (XRD) was used to investigate the crystallinity of the films. The tool used for XRD was described above in X-Ray Reflectivity (Section 1.3.3). XRD relies on satisfying the Bragg equation,

$$n\lambda = 2\mathrm{d}\sin\theta \qquad \text{(Eq. 1.5)}$$

where n is an integer, λ is the X-ray wavelength (1.540 Å), d is the plane spacing in the crystal structure, and θ is the incident angle (Figure 1-11).[45]

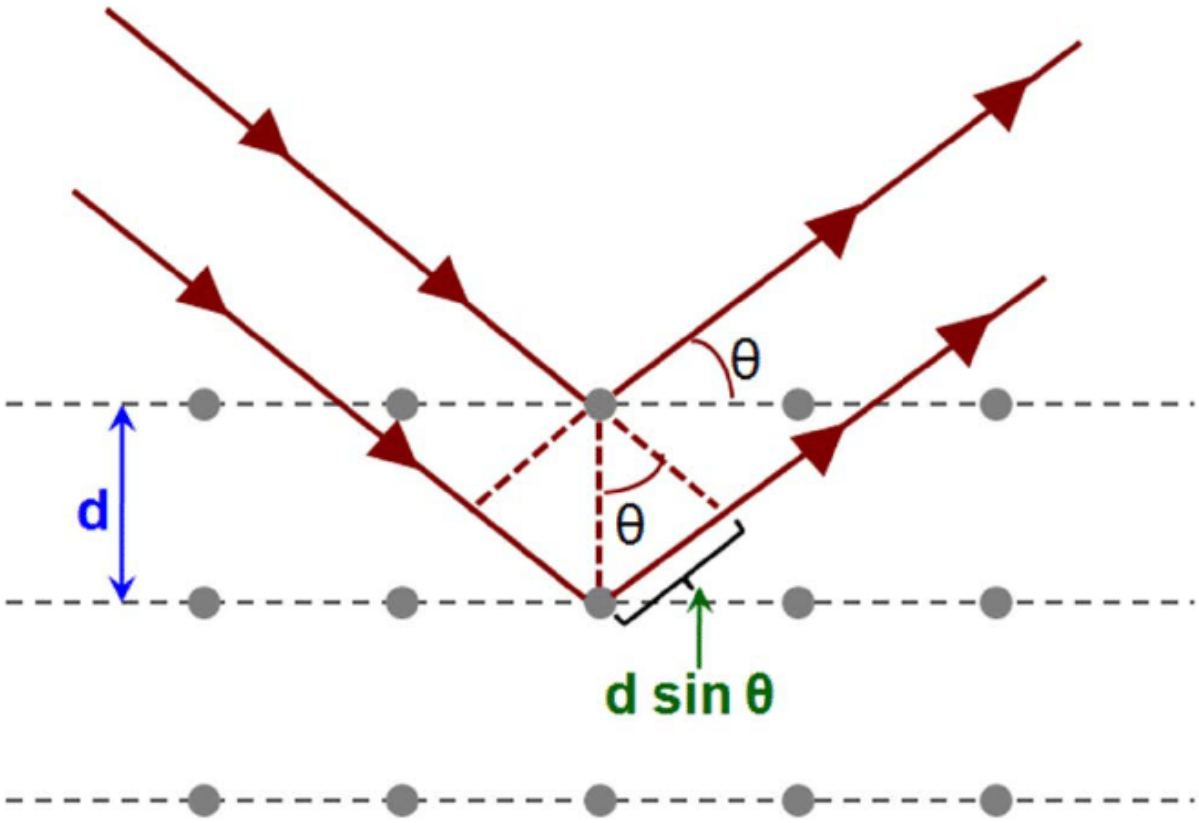

Figure 1-11. Schematic depiction of Bragg's law.[46]

For constructive interference to occur, an X-ray photon interacts with each lattice site separated by distance d and interferes with itself. This produces an increase in measured X-ray intensity and is called a diffraction peak. The Bragg condition is satisfied when the incident angle is equal to the diffracted angle, θ. When the source and detector are both moved together to maintain specular reflection from a sample, the angle that is formed between them is 180°-2θ. When reporting the angle of XRD scans, the angle then is typically reported as 2θ to account for the movement of both the source and detector.

The diffraction data, or diffractograms, shown in this work were collected in a mode especially suited for thin films called grazing incidence XRD (GIXRD).[47] This mode relies on

the incident angle being fixed at a small value, typically 0.3-2°, to allow the x-rays to interact maximally with the thin film on the surface. This small angle should be chosen to be just larger than the critical angle, or the smallest angle at which the incident x-rays will be totally internally reflected. This ensures the x-rays will "see" the maximum amount of the thin film on top to ensure the best signal to noise while still producing reflected diffraction peaks. The convention of reporting the angle as 2θ is followed here. The angle the detector travels from the angle of the source defines the angle 2θ. GIXRD films must be polycrystalline to reliably show diffraction peaks. The array of randomly oriented grains allows for a fixed incident angle to satisfy the Bragg condition for all of the available X-ray reflexes.

Once a diffractogram is generated by XRD it can be compared to literature diffractograms in a relevant database. Diffractograms can be searched by peak position, mineral name, elements present, or composition. Careful selection of an appropriate reference pattern can confirm the crystal structure and nominal composition of the sample being measured. Peak indices can be assigned to the measured diffractogram using the reference diffractogram as well. Peak shifts to the left or right relative to the reference pattern can be explained by increased or decreased lattice constants, respectively. This may be due to a chemical change, such as a substitution of a larger atom for a smaller one, or a mechanical stress from thermal contraction as a thin film cools at a different rate to the substrate.

1.3.5 X-Ray Photoelectron Spectroscopy

X-ray photoelectron spectroscopy (XPS) was used to determine the composition of thin films ex situ. The film composition was determined using an X-ray photoelectron spectrometer (PHI 5600) using a monochromatic Al Kα source with an energy of 1486.6 eV. The XPS data

were collected using Auger Scan (RBD Instruments) software. The XPS data were analyzed in CASA XPS (Casa Software Ltd.) software.

XPS utilizes a soft X-ray source to probe the composition of the surface of thin films.[48] The sampling depth of XPS is larger than that of AES, but it is still surface sensitive with a soft x-ray source as lower energy x-rays have a shallower penetration depth. XPS utilizes the photoelectric effect, wherein a photon of sufficient energy is absorbed by an electron, giving it energy to escape the atomic nucleus. The kinetic energy of the ejected electron relative to the energy of the primary beam is used to determine the element from which it came, as well as the chemical environment the parent atom was in. XPS operates according to the following equation

$$E_{Binding} = E_{Photon} - (E_{Kinetic} + \phi) \quad \text{(Eq. 1.6)}$$

where $E_{Binding}$ is the binding energy of the ejected electron, E_{Photon} is the energy of the X-ray photon, $E_{Kinetic}$ is the kinetic energy with which the electron is ejected, and ϕ is the work function of the sample material plus any calibration terms. A schematic of the XPS apparatus used in this work can be seen in Figure 1-12.[48]

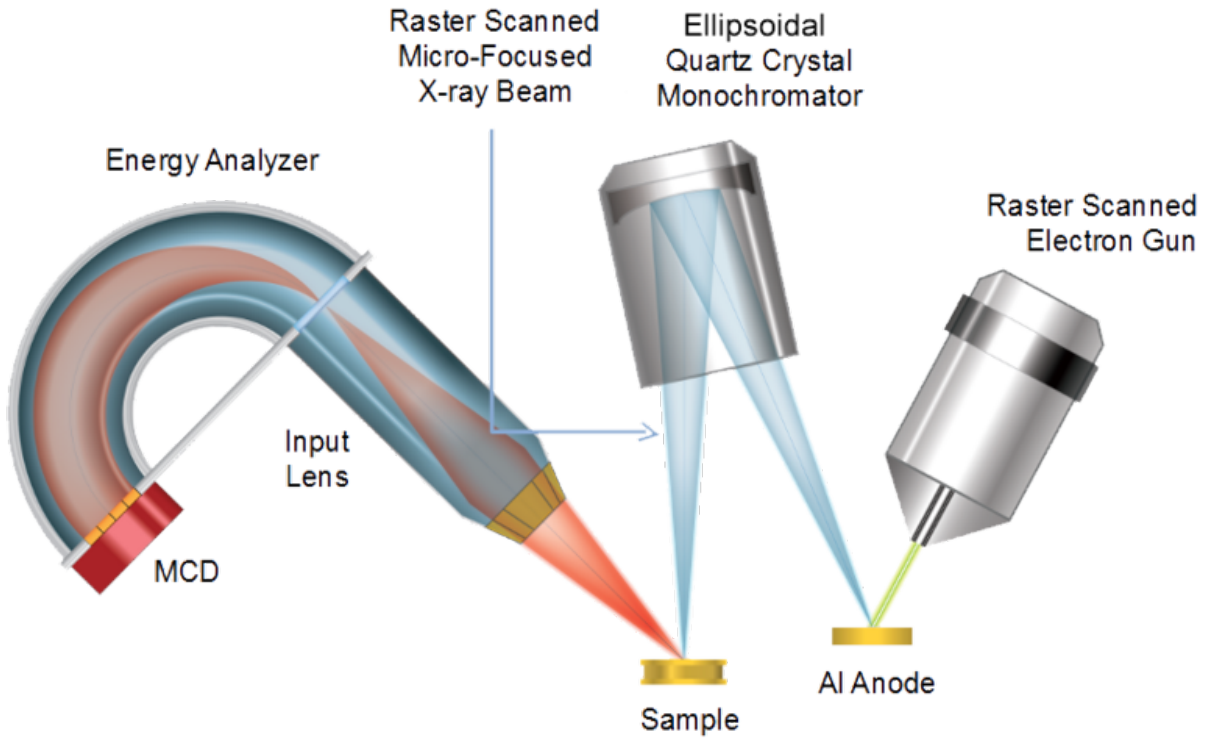

Figure 1-12. Diagram of a PHI XPS. The major components are the electron gun used to generate the X-rays, the monochromator, the sample, and the energy analyzer.[49]

Eq. 1.6 is a conservation of energy equation where the energy is transferred from the incident photon to the ejected electron. Depending on the chemical environment of the atom the binding energy will change. XPS is sensitive to small changes in the binding energy and can determine oxidation states and chemical environments.[50] XPS can be used in combination with ion sputtering to build a compositional depth profile of a film. An XPS scan is taken, then the surface of the sample is sputtered. This is repeated, building a 2D map of composition versus thickness.

AES and XPS are complementary techniques. In this work, AES is used in situ. This is valuable to determine surface composition before atmospheric exposure. AES is also more surface sensitive than XPS due to the short mean free path of Auger electrons relative to the

photoelectrons in XPS. This makes AES useful for determining composition of thin films or the development of film composition during nucleation. The AES used in this work has a relatively poor signal to noise ratio as compared to the XPS used in this work. For more accurate film composition measurements XPS is the preferred tool. As mentioned, the XPS tool used in this work was equipped with a sputter gun, allowing for sputter profiling. As such, XPS is the preferred compositional analysis tool for determining the composition in the bulk of a film.

1.3.6 Atomic Force Microscopy

Atomic Force Microscopy (AFM) measurements were performed with a Park NX10 AFM instrument using non-contact mode. The scan rate used was between 0.2-1.0 Hz with an Olympus micro cantilever probe (OMCL-AC160TS). AFM was used to determine surface roughness and morphology. Ellipsometry and XRR are also able to model surface roughness, however AFM is the preferred technique for determining surface roughness. XRR and ellipsometry must be modeled carefully, and measure roughness indirectly. AFM measures roughness directly without the need for complicated data modeling. AFM uses a microscopic tip rastered over the sample surface to output a 3D surface profile. The tip is controlled with sub nm precision with piezoelectric actuators. The tip hovers just above the sample surface. The tip oscillates at its resonant frequency driven by the piezoelectric actuators. The distance from the tip to the sample changes the nature of the tip-sample interactions. The interaction between the tip and the sample can be described by the Lennard-Jones potential

$$V_{LJ}(r) = 4\varepsilon\left[\left(\frac{\sigma^{12}}{r}\right) - \left(\frac{\sigma^{6}}{r}\right)\right] \quad \text{(Eq. 1.7)}$$

where V_{LJ} is the potential between the tip and the sample, ε is the dispersion energy, and σ is the distance at which the intermolecular potential between the two particles is zero, i.e., the van der Waals radius.[51]

As the tip approaches the sample an attractive force is felt by the tip according to the $-\left(\frac{\sigma^6}{r}\right)$ term in Eq. 1.7. This effectively changes the spring constant of the tip, changing its natural frequency. The electronics in the AFM keep the tip oscillating at the same distance from the sample by tuning the z-actuator to keep the oscillator frequency the same. The oscillation frequency is determined by reflecting a laser off the cantilever arm which holds the tip. The laser reflection is picked up by a CCD sensor which records the oscillation frequency. This allows the instrument to infer the position of the sample surface without touching the sample surface and altering the tip geometry or the sample through tip contact with the sample. This is called non-contact mode (NCM). NCM increases image quality and greatly extends tip life over contact mode. All AFM data in this work was collected using NCM.

In NCM, the tip oscillation frequency is used as feedback to determine sample surface morphology. This contrasts with contact mode, where the repulsive force of the Lennard-Jones potential $\left(\frac{\sigma^{12}}{r}\right)$ Eq. 1.7 pushes the tip and cantilever arm (Figure 1-13).

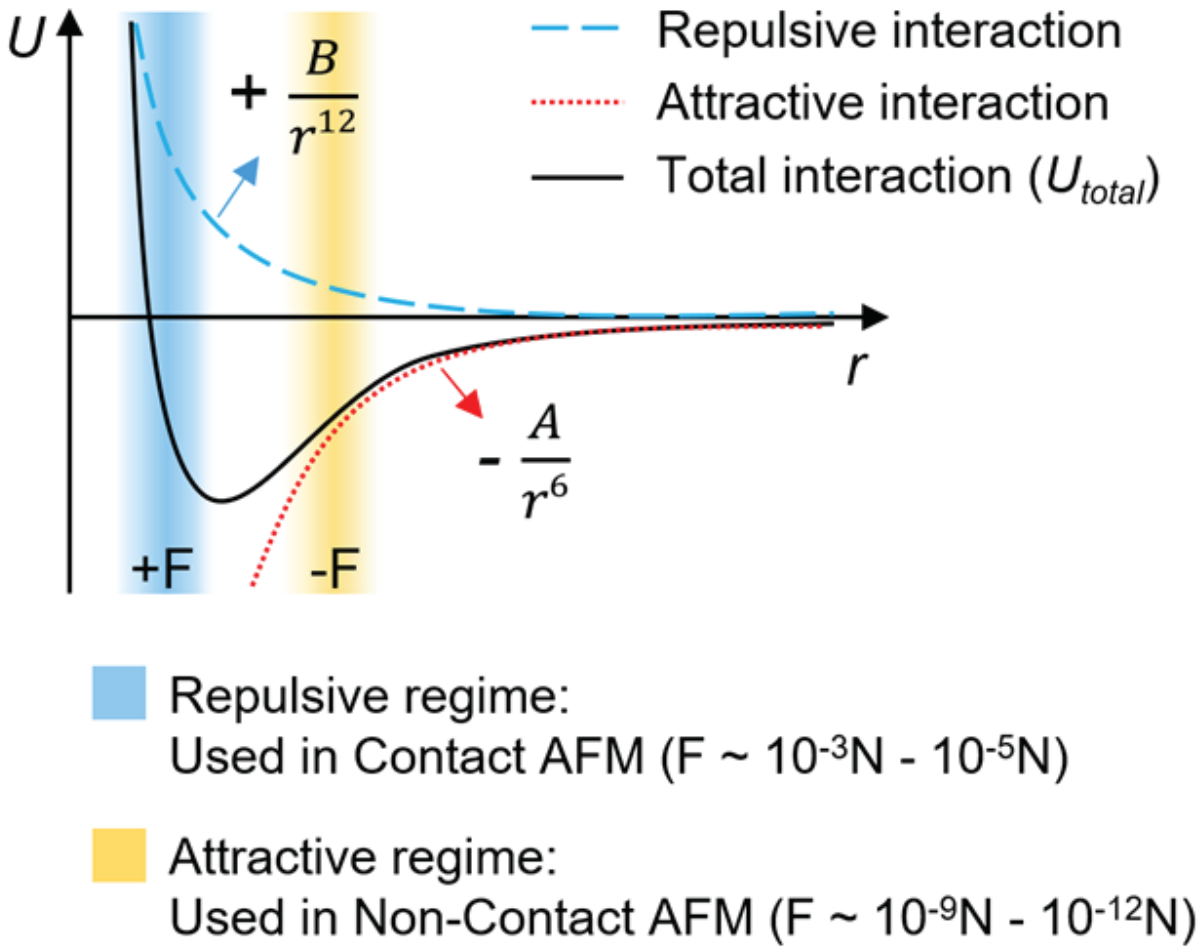

Figure 1-13. Interatomic interaction potential U vs. distance r as approximation for the tip-sample interaction. The blue curve represents a purely repulsive interaction, while the red curve represents a purely attractive interaction. The black curve is a combination of long-range attractive and short-range repulsive interaction called the Lennard-Jones Potential. At larger distances, the net force is attractive (-F), which switches to a net repulsive force (+F) when two atoms are brought closer.[52]

The deflection in the cantilever arm is picked up by the laser position on the same CCD sensor. In contact mode the cantilever deflection is used as feedback to determine surface morphology and the z-actuator adjusts the height of the tip above the sample to maintain a constant force.[53]

1.3.7 Four-Point Probe

A four-point probe (4pp) (Signatone, QP2-MB8) was used for ex situ resistivity measurements. The probes were WC their spacing was 1 mm. 4pp is a preferred method to measure resistivity because it allows the resistivity measurement to be made without the probe contact resistance affecting the measurement. A set current is forced through the outer two probes by applying a sufficient potential to drive the set current. A voltage is measured between the inner two probes to determine the sheet resistance according to the formula

$$\rho_{\square}\left(\frac{\Omega}{\square}\right) = \frac{\pi}{\ln(2)}\frac{\mathrm{I}}{\mathrm{V}} \qquad \text{(Eq. 1.8)}$$

where I is the forced current and V is the measured voltage (Figure 1-14).[54]

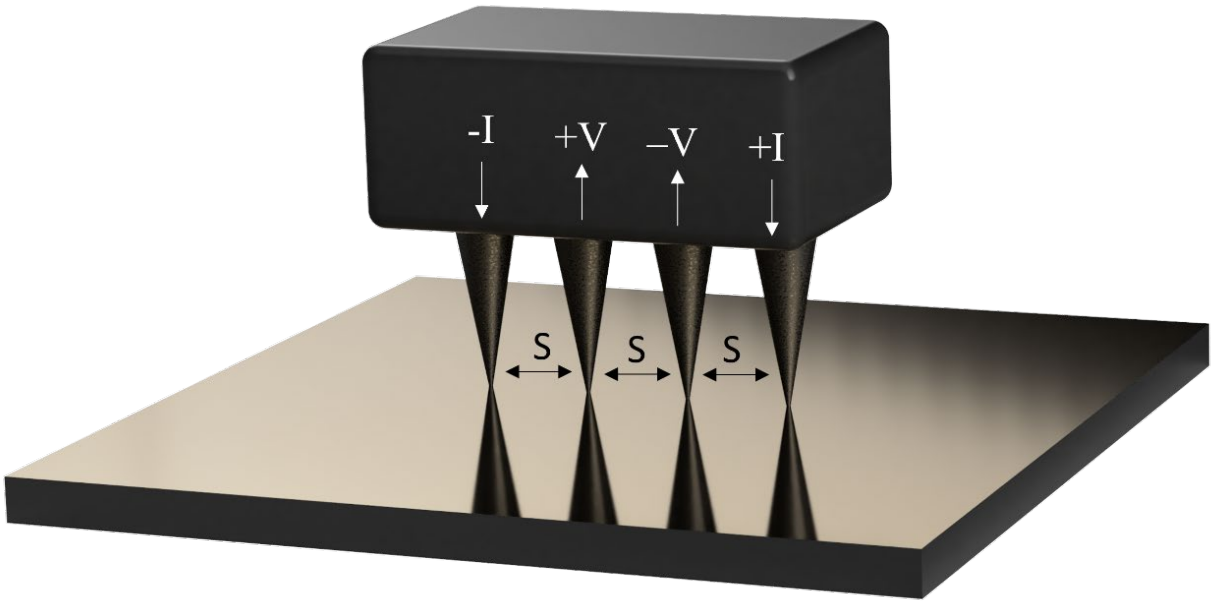

Figure 1-14. Simplified render of a 4-point probe showing forced current into the sample on the outer probes and the measured voltage on the inner probes. S is the probe tip spacing.

This relationship holds true for films with an infinite area. In practice, a geometric correction factor must be applied to account for edge effects. A geometric correction factor was chosen based on the ratio of the probe spacing to the diameter of the largest inset circle possible on the wafer coupon, typically around 2 cm diameter. The geometric correction can be found tabulated according to the ratio described above. A typical geometric correction factor in this work was 0.92. To convert from sheet resistance to resistivity the film thickness must be known. The film thickness is multiplied by the sheet resistance (Eq. 1.8) to find the resistivity.

1.4 Research Topics

After the discussion of the basic chemistry, equipment, and characterization tools used a brief discussion of the research to follow is prudent. The work for this dissertation began with the deposition of EE-ALD cobalt films from $CO(CO)_3NO$ with significant oxygen contamination utilizing a low energy electron flood gun (Section 2). The films were analyzed with in situ ellipsometry to establish the growth characteristics. Ex situ focused probe ellipsometry was used to determine the film profile. From the comparison of the as-deposited film profile to the known Gaussian distribution of the low energy electron beam used for deposition an ESD cross section was calculated. From this cross section different spatial profiles showing various degrees of saturation were generated. Ex situ surface sputtered XPS was used to determine the film composition as predominantly cobalt and oxygen with a small nitrogen impurity, likely from the NO ligand on the $CO(CO)_3NO$ molecule.

The high emissivity coating on the filament of the low energy electron gun was rapidly deteriorated by exposure to the $CO(CO)_3NO$ precursor, so a new electron source was developed (Section 3). A hollow cathode plasma electron source (HC-PES) was chosen for its simplicity, high electron flux capabilities, and its chemical insensitivity. The function of the hollow cathode

was discussed, including the hollow-cathode effect. In-house development of the electron source was successful, and implementation of electron optics greatly improved the purity of the electron beam. A comparison of Co deposition between the electron gun and the HC-PES showed the great improvement the hollow cathode afforded in deposition area and speed.

The superior properties of the HC-PES allowed for the deposition of high quality titanium nitride (Section 4). TiN was deposited with tetrakis(dimethylamido)titanium(IV) (TDMAT) and an NH_3 reactive background gas (RBG). The introduction of NH_3 RBG is possible only with the chemical insensitivity and high operating pressure of the HC-PES. The NH_3 RBG greatly enhanced the purity of the TiN films. The interaction of the NH_3 RBG with the low energy electrons is hypothesized to make ·N radicals which scour C and O from the TiN film. The EE-ALD TiN films were low resistivity, high purity, and crystalline. The EE-ALD TiN films nucleated rapidly and were ultra-smooth as measured by ex situ AFM.

2 Growth of Cobalt Films at Room Temperature Using Sequential Exposures of Cobalt Tricarbonyl Nitrosyl and Low Energy Electrons

Zachary C. Sobell, Andrew S. Cavanagh, and Steven M. George

Department of Chemistry, University of Colorado
Boulder, Colorado 80309-0215

2.1 Abstract

Cobalt thin films were grown at room temperature using sequential exposures of cobalt tricarbonyl nitrosyl (CTN, $Co(CO)_3NO$) and low energy (75-175 eV) electrons. During this cyclic growth process, the CTN molecules were first adsorbed on the substrate. The electrons then induced the desorption of the carbonyl and nitrosyl ligands from the adsorbed CTN. The removal of CO and NO ligands produced new adsorption sites. Subsequent CTN exposures allowed CTN to react with these new adsorption sites on the substrate. In situ ellipsometry was utilized to monitor the film thickness during the electron-enhanced growth. Co growth rates as high as 1.3 Å/cycle were observed by in situ ellipsometry depending on the reaction conditions. The in situ ellipsometry also observed the CTN adsorption and the removal of the carbonyl and nitrosyl ligands. Quadrupole mass spectrometer measurements confirmed the desorption of CO and NO during electron exposures. X-ray photoelectron spectroscopy (XPS) measured N XPS signals from the Co films deposited using electron exposures at 200 eV. The N/Co XPS signal ratio was consistent with the dissociation of 13% of the nitrosyl ligands on the CTN precursors that lead to Co deposition. In contrast, the negligible C XPS signals from the Co films indicated that the CO ligands were desorbed completely from CTN by the electron exposures at 200 eV. Under identical reaction conditions at lower incident electron currents, the maximum growth rate was obtained at an electron energy of 125 eV. Because the Co growth depends on the electron flux, the Co films were deposited only on the surface area irradiated by the electron beam. The

spatial profile of the Co film deposited using long electron exposure times was mapped by ex situ spectroscopic ellipsometry. This spatial profile displayed a pronounced flat top that was consistent with the electron flux desorbing nearly all the CO and NO surface coverage in the central area of the electron beam during each reaction cycle. The spatial profile was used to calculate an electron induced desorption cross section of $\sigma = 2 \times 10^{-17}$ cm^2 at 200 eV. This cross section was in approximate agreement with the cross sections for the electron impact dissociation of CTN in the gas phase.

2.2 Introduction

Electrons are able to enhance surface reactions by a number of pathways including electron stimulated desorption (ESD), dissociative electron attachment (DEA) and electron induced dissociation (EID).[14] These electron-induced processes can dramatically reduce the temperature for thin film growth. These processes can also be employed for nanofabrication using focused electron beam induced deposition (FEBID).[14] There are many unanswered questions on the exact mechanism for electron-enhanced reactions and the dependence of these reactions on electron energy.[15] Although high electron energies >1 keV are typically utilized for FEBID, the secondary electrons with energies <50 eV may be the most effective in inducing the surface reactions.[11, 15, 55]

ESD can enhance thin film growth by removing surface species that limit surface reactions. ESD can occur by a number of pathways including the Menzel-Gomer-Redhead (MGR)[25] and the Knotek-Feibelman (KF)[27] mechanisms. The MGR mechanism is characterized by the promotion of a bonding electron to an antibonding orbital that leads to the scission of the bond. In contrast, the KF mechanism is an Auger process. An incident electron can remove a core electron, then an electron from a higher energy level can drop down to replace the ejected

electron. Energy conservation leads to another electron being ejected from the system together with ligand desorption.

DEA can also enhance surface reactions by promoting the decomposition of the reactant.[11-12] DEA is usually observed with low energy electrons < 10 eV. These low energy electrons can be produced by secondary electrons. The reactant can capture a low energy electron and form a transient negative ion. This transient negative ion can either relax through reemission of the electron or dissociate to produce an anion and a neutral species.

EID can also enhance surface reactions by causing the dissociation of the reactant.[11, 21] The dissociation could occur by dissociative ionization where the electron removes a bound electron from the reactant and forms a cation. The cation can then undergo fragmentation to produce various dissociation products. The dissociation could also occur by neutral dissociation resulting from electronic excitation. The excited neutral may then decompose to neutral fragments if the potential energy surface is repulsive.

Previous studies have shown that thin films can be deposited at room temperature using sequential surface reactions with low energy electrons. For example, GaN films can be grown at room temperature with a sequential surface reaction approach similar to atomic layer deposition (ALD).[30] This GaN film growth was performed using sequential $Ga(CH_3)_3$, NH_3 and electron exposures. Hydrogen radical beam exposures after the $Ga(CH_3)_3$ exposures were able to replace the CH_3 groups with H surface species. The low energy electrons led to hydrogen desorption and produced new adsorption sites. GaN growth rates of 1.3 Å/cycle were measured at electron energies of 50 eV.[56]

Si films have also been deposited at room temperature using sequential Si_2H_6 and low energy electron exposures.[30] The Si electron-enhanced ALD (EE-ALD) growth occurred at

electron energies from 25-200 eV. The low energy electrons were able to desorb hydrogen and produce new adsorption sites. The Si growth was self-limiting and saturated at longer Si_2H_6 and electron exposures. The maximum Si EE-ALD growth rate of 0.3 Å/cycle was observed at 100-150 eV.[30]

BN films have also been deposited at room temperature using sequential borazine ($B_3N_3H_6$) and low energy electron exposures.[57] The BN EE-ALD growth occurred at electron energies from 40-440 eV and saturated at longer borazine and electron exposures. The maximum BN EE-ALD growth rate of 3.2 Å/cycle was observed at 80-160 eV.[57] This growth rate was nearly identical to the distance between neighboring BN basal planes in hexagonal BN. In addition, the BN EE-ALD displayed topographical selectivity and preferentially deposited on horizontal surfaces when the electron beam was normal to the surface.[57] These area-selective EE-ALD results suggested that EE-ALD could be employed for "bottom-up fill" of vias and trenches with vertical sidewalls.

In the current paper, Co thin films were grown using sequential cobalt tricarbonyl nitrosyl (CTN, $Co(CO)_3NO$) and low energy electron exposures. Cobalt is emerging as an important interconnect material to replace copper or tungsten.[58-59] The ability to deposit cobalt in vias and trenches using a "bottom-up fill" mechanism would be desirable to avoid voids and grain boundaries in the conducting lines. CTN is a common cobalt precursor utilized for Co chemical vapor deposition (CVD) at temperatures from 150-480°C.[60-61] The highest purity Co CVD films have been deposited at 350-480°C.[60] CTN is also used to fabricate Co nanostructures using FEBID techniques.[13, 16, 24, 62]

Many investigations have explored the mechanisms involved during Co deposition using CTN with FEBID techniques. The role of low energy electrons and the DEA process during Co

deposition using CTN have been examined by several studies.[11-12, 63] These investigations conclude that the DEA pathway is non-negligible and leads to incomplete CTN decomposition. Other studies have examined the EID and electron induced ionization of CTN in the gas phase.[64-66] These investigations have measured absolute cross sections for the electron induced processes versus electron energy.[66] These gas phase studies versus electron energy are useful to compare with the Co FEBID results versus electron energy to determine the effect of the surface. Additional investigations have examined the individual steps during CTN decomposition by FEBID using surface analytical techniques such as X-ray photoelectron spectroscopy (XPS) and quadrupole mass spectrometry (QMS).[24]

This study investigated Co thin film growth using sequential exposures of CTN and low energy electrons from 75 -175 eV. The growth of the Co films versus number of reaction cycles was examined in an ultrahigh vacuum (UHV) chamber using in situ ellipsometry. The in situ ellipsometry measurements were able to monitor the CTN adsorption and the subsequent desorption of ligands during the electron beam exposure. QMS analysis was also used to determine that CO and NO were desorbed into the gas phase during electron exposure. Additional ex situ spectroscopic ellipsometer experiments were used to map the spatial profile of the Co film formed by the area-selective electron beam. This spatial profile was also utilized to determine the electron induced desorption cross-section at 200 eV.

2.3 Experimental

2.3.1 Vacuum Chamber

Metallic Co films were grown in an UHV chamber described previously.[30, 57] The chamber contains a load lock with a Pirani gauge and hot cathode as pressure sensors. The load lock includes an integrated UV light source to desorb water from the sample, sample holder, and

walls of the load-lock chamber. The load lock is pumped with a turbomolecular pump with a pumping speed of 67 L/s backed by a rotary vane pump. The load lock is separated from the main chamber by an UHV gate valve. The main chamber is pumped by two turbomolecular pumps, one operating at 245 L/s, backed by a smaller turbomolecular pump operating at 67 L/s that is backed by a rotary vane pump. Additionally, the main chamber is pumped by an ion pump operating at 80 L/s with a valve used to close the ion pump off to process gases.

The main chamber has both hot and cold cathode pressure sensors (MKS), as well as an in situ ellipsometer (Filmsense1), mass spectrometer (PrismaPlus QMG 220, Pfeiffer Vacuum), and a pico-ammeter (Keithley) attached to the sample stage to measure the incident electron current. Attached to the main chamber, separated by another UHV gate valve, is an analysis chamber equipped with an ion pump with a pumping speed of 75 L/s and an in situ Auger electron spectroscopy (AES) spectrometer.

2.3.2 Growth Procedure

Si wafers (Silicon Valley Microelectronics, boron doped) were washed in methanol and acetone and blown dry with ultra-high purity nitrogen. There was no attempt to remove the native oxide on the silicon surface. The Si wafer was then loaded into the load lock chamber. The pressure was reduced to ~10^{-6} Torr, and then the UV light was activated for 90 minutes to desorb water. Upon pressure reduction to ~10^{-8} Torr, the load lock was opened to the main chamber, and the sample was transferred to the sample stage that was positioned normal to the electron gun. The sample was further irradiated with UV light for 30 minutes while the main chamber pumped down to at least 1 x 10^{-9} Torr before the first precursor exposure.

The Co growth was conducted using a pulse sequence consisting of: (1) CTN adsorption; (2) purging; (3) electron gun warm up; (4) electron gun exposure; and (5) electron gun cool

down. The timing for this pulsing sequence can be characterized by (t_1, t_2, t_3, t_4, t_5). The CTN precursor was kept at 1.5 Torr behind a micropulse valve. The valve was actuated for t_1 = 0.1 s. The valve opening led to a transient pressure in the main chamber of ~7.5 x 10^{-6} Torr. A purge was then performed for a total of t_2 = 75 s. An additional t_3 = 50 s was required for the filament of the electron flood gun to warm up. A typical electron exposure was then performed at 100 eV for t_4 = 240 s, with an emission current of 100 μA. Another delay time of t_5 = 175 s was introduced to allow the cooling of the electron gun filament. The timing for this pulsing sequence was (0.1, 75, 50, 240, 175). The sum of these steps produced a reaction cycle time of 540 seconds or 9 minutes.

2.3.3 Electron Flood Gun

Co film growth was observed using low energy (75-175 eV) electrons from an electron flood gun. The electron flood gun was a model FRA-2x1-2 from Kimball Physics Inc. The filament was a tantalum disc mounted on a tungsten-rhenium (95%-5%) support. The electron gun was capable of producing electron energies of 5-100 eV and emission currents of 1 nA to 400 μA. The grid voltage was set at 100 V. To preserve the filament and avoid overcurrent conditions, the emission current was maintained at 100 μA.

The total emission current of 100 μA was not incident on the sample. The pico-ammeter measured incident electron currents on the sample that were less than the emission current of 100 μA. Most of the loss of the electron current occurs on the grounded anode of the electron gun. During earlier experiments when larger Co growth rates of 1.0-1.3 Å/cycle were measured at electron energies of 125-150 eV, the incident electron currents were 33-45 μA. During later experiments after many Co deposition experiments when smaller Co growth rates were measured at similar electron energies, the incident electron currents were lower at 24-28 μA. The lower

incident electron currents are attributed to the effect of Co deposition on the grid and anode of the electron gun.

2.3.4 Ellipsometry and XPS Analysis

In situ ellipsometry (Filmsense, FS1) measurements were performed in duplicate after each electron exposure. The in situ ellipsometer uses four wavelengths of light. The measurements were averaged to obtain the growth per cycle. The precision of the in situ ellipsometry measurements of film thickness is within ± 0.03 Å.

Ex situ spectroscopic ellipsometry (Model M-2000, J.A. Woollam Co., Inc.) was performed to obtain the n and k values, measure the film thickness and determine the spatial profile of the deposited film. The data was fit using a B-spline model in CompleteEase (J.A. Woollam Co., Inc.) with n & k values for Co as a starting point. Focusing probes that reduce the spot size to 0.3-0.4 mm were used for all data acquisition.

The film composition was determined using an X-ray photoelectron spectrometer (PHI 5600) using a monochromatic Al Kα source with an energy of 1486.6 eV. The pass energy was 29.35 eV and the step size was 0.25 eV. An electron beam neutralizer was used during the XPS measurements. The XPS data were collected using Auger Scan (RBD Instruments) software. The XPS data were analyzed in CASA XPS (Casa Software Ltd.) software.

2.4 Results and Discussion

2.4.1 Nucleation, Growth and Observation of Precursor Adsorption and Ligand Desorption

The nucleation and growth of a Co film on the native oxide of a silicon wafer at room temperature was measured using in situ ellipsometry as shown in Figure 2-1. The Co film growth was conducted at an electron energy of 150 eV. The timing for the pulsing sequence was

(0.1, 75, 50, 120, 175). The electron current from the filament was 100 μA. The incident electron current on the sample was 33 μA. The in situ ellipsometry measurements were conducted after each reaction cycle. Figure 2-1

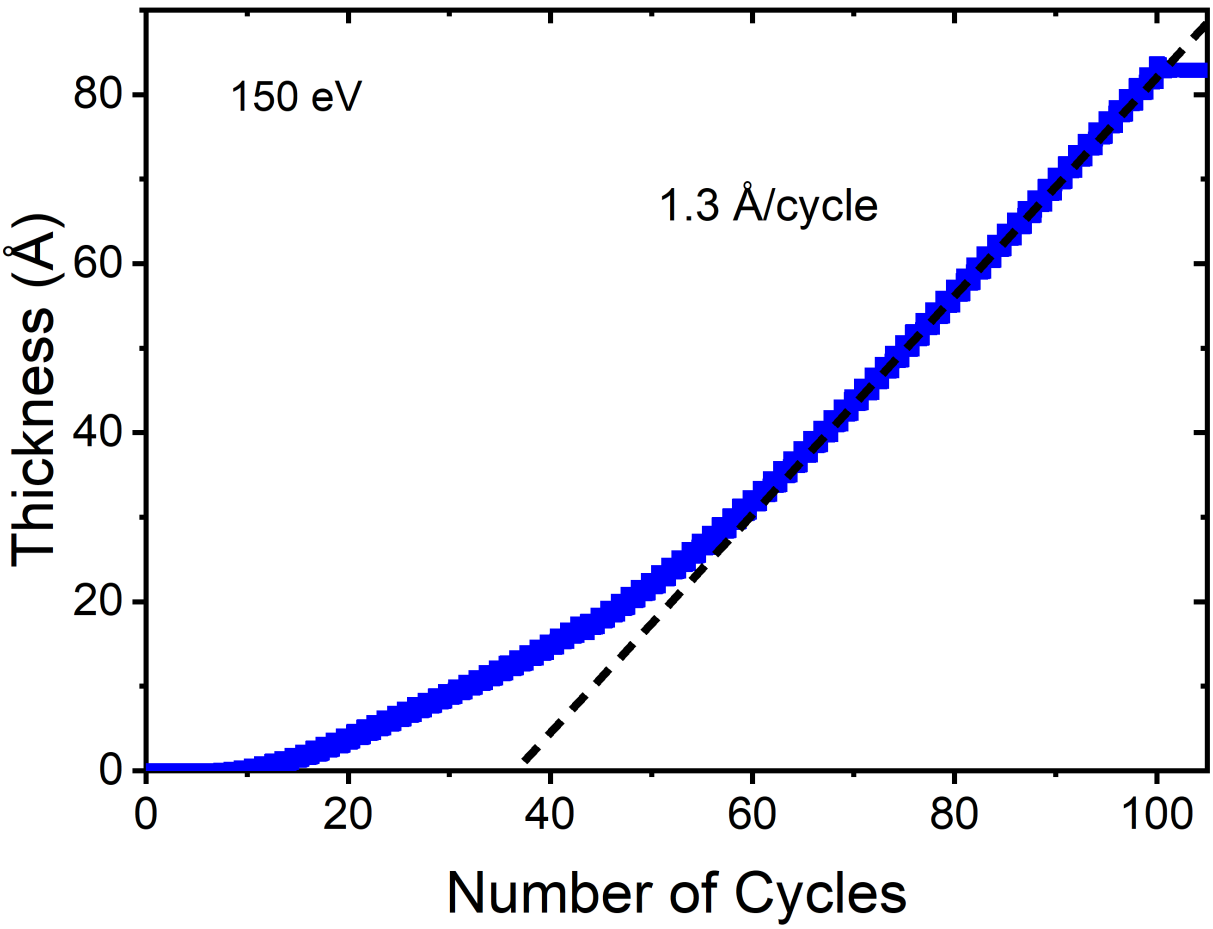

Figure 2-1. Film thickness measured by in situ ellipsometry vs the number of reaction cycles during Co growth on native oxide on an Si wafer.

shows that there is very little Co deposition during the first 10 reaction cycles. The film growth then begins to occur at >10 reaction cycles. After >55 reaction cycles, the Co film is growing linearly at a rate of 1.3 Å/cycle.

The nucleation delay is likely caused by the lack of active sites on the native oxide of the silicon wafer. Repeated cycles of CTN adsorption followed by electron exposures slowly builds up active Co sites on the surface. These Co sites probably first form small islands and then the islands may grow together as described by the Volmer-Weber mechanism.[67] This behavior has been observed by previous nucleation studies of metal ALD on oxide surfaces.[68] After a continuous Co film forms on the surface, there will be a full coverage of active sites on the surface. At this point, the Co deposition reaches the steady state, linear growth regime. To achieve a more rapid nucleation, experiments could also be performed on H-passivated Si surfaces. Earlier Si EE-ALD experiments have demonstrated that hydrogen can be desorbed from Si surfaces by low energy electron exposures.[30] The active sites produced by hydrogen desorption are expected to be very reactive and should facilitate prompt nucleation.

An expansion of the in situ ellipsometry measurements displayed in Figure 2-1 reveals the individual events during the sequential CTN and electron exposures. Figure 2-2 shows the film thickness measured during 6 reaction cycles from Figure 2-1. The individual ellipsometry measurements were performed every 10 s. The rapid increase in the thickness observed in Figure 2-2 occurs when the CTN precursor is dosed into the chamber and adsorbs on the surface. Subsequently, the thickness decreases slowly during the purge following the CTN exposure. The thickness then decreases rapidly at the onset of the electron exposure and resulting electron induced desorption from the surface. The thickness then is constant during the delay time after the electron exposure.

The decrease in the thickness in Figure 2-2

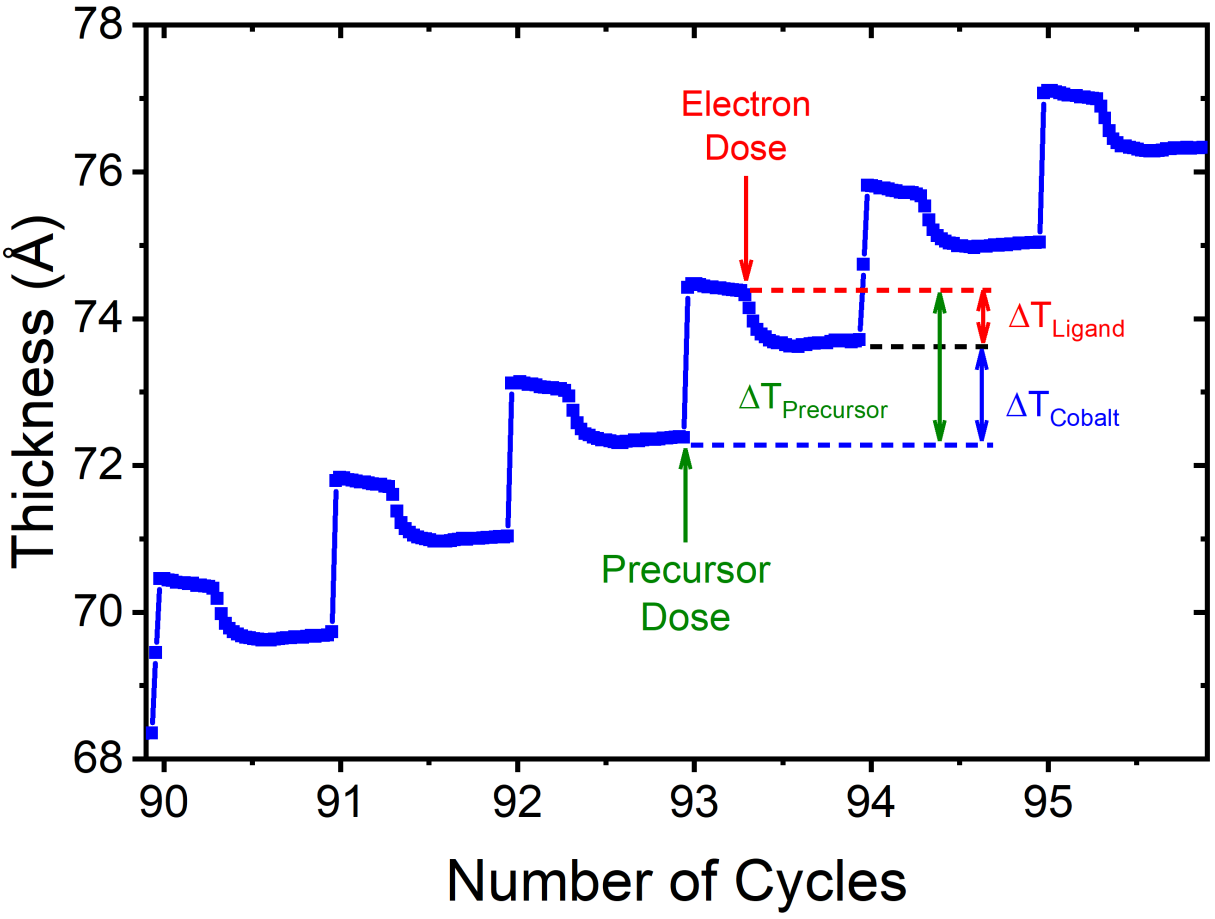

Figure 2-2. Expansion of film thickness measured by in situ ellipsometry for six reaction cycles. Expansion shows a thickness increase during CTN adsorp- tion, a thickness loss during electron beam exposure when CO and NO ligands are removed, and nearly constant thicknesses during purge times after CTN and electron beam exposures.

during the onset of the electron exposure corresponds with the desorption of CO and NO ligands from CTN adsorbed on the surface. To confirm the desorption of CO and NO, QMS was used to monitor the gas phase during the reaction cycle. For these experiments, the electron energy was 100 eV. The electron current from the filament was 100 μA. The incident electron current on the sample was 45 μA. Each reaction cycle had a timing for the pulse sequence of (0.1, 75, 50, 60, 175). Figure 2-3

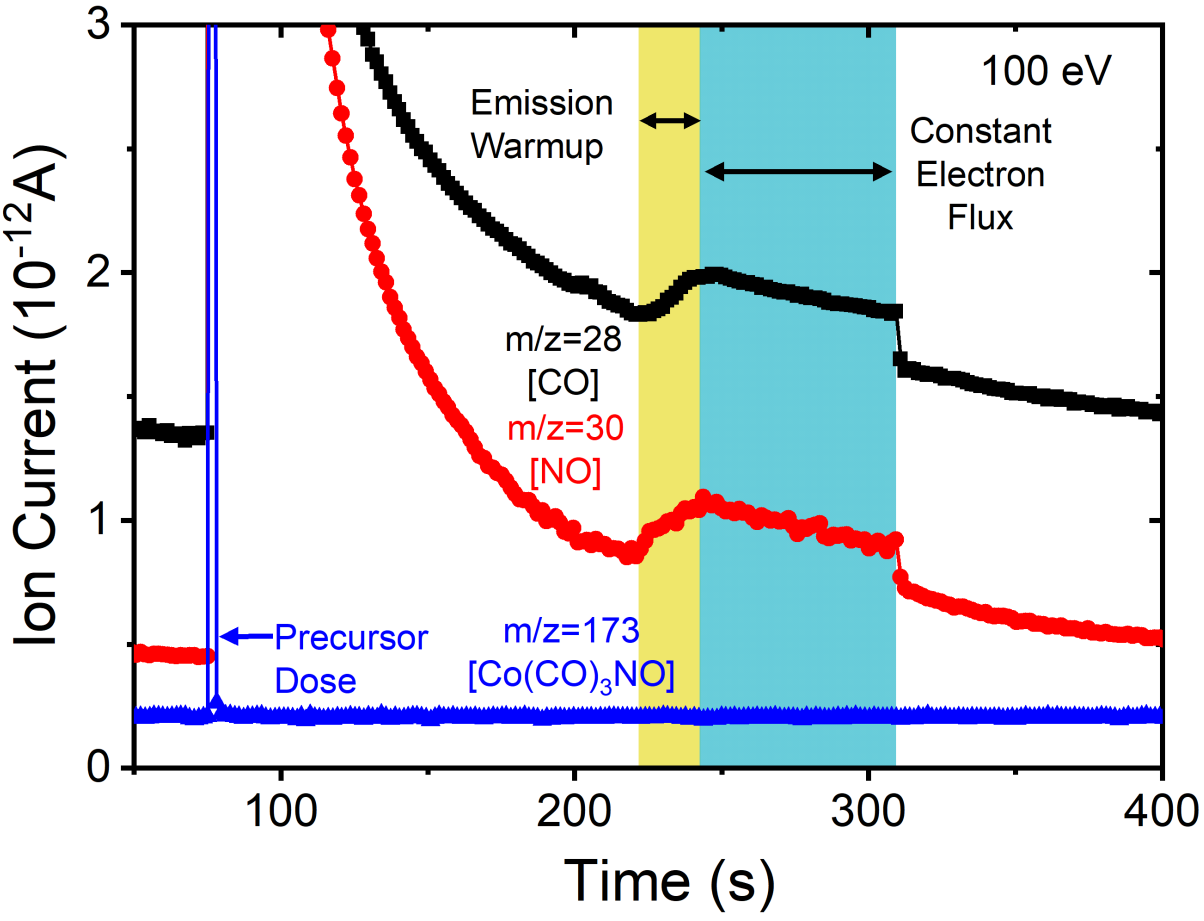

Figure 2-3. Partial pressures of CO, NO, and parent molecule, CTN, as recorded by quadrupole mass spectrometer during sequential CTN exposure, purge time after CTN exposure, electron exposure, and a delay time after electron exposure.

shows the QMS results at m/z = 28, 30 and 173 corresponding with CO, NO and $Co(CO)_3NO$.

Figure 2-3 shows that the ion currents for m/z = 28, 30 and 173 are high during the CTN exposure that occurs at 75 s. These masses are all part of the mass spectrometry fragmentation pattern for CTN.[64-65] The ion current for m/z = 173 is present only during the CTN exposure. The ion currents for m/z = 28 and 30 persist during the pumping period following the CTN exposure. They decrease as expected for the pumping of NO and CO from the chamber.

The electron beam exposure that occurs at 220 s then increases the ion currents only for m/z = 28 and 30 corresponding to CO and NO. There is no ion current for CTN at m/z=173. These ion currents increase slowly during the initial electron emission from the electron filament. These ion currents then slowly decrease again after the electron emission current has reached its final value of 100 μA at 245 s. The ion currents for m/z = 28 and 30 then decrease rapidly when the electron emission current is stopped at 320 s. The ion currents continue to decrease because of pumping during the delay time after the electron exposure.

Additional QMS experiments were performed at higher electron energies of 400 eV. Ion currents were again observed for m/z = 28 and 30 corresponding to CO and NO desorption from the surface. However, no peaks were observed at m/z = 173 from CTN or at m/z = 59 from possible Co etching products. These results are in contrast to earlier results for GaN electron-enhanced growth where Ga-containing etch products were observed to desorb at greater abundance at higher electron energies.[56]

These QMS results can also be compared with earlier QMS investigations of electron irradiation of CTN multilayer films.[24] These CTN multilayer films had a thickness of ~2.5 nm and were adsorbed on gold substrates at -168°C. Upon electron irradiation at an electron energy of 500 eV, CO and negligible NO were observed in the gas phase.[24] In addition, there was no evidence of any Co-containing species in the gas phase. The lack of NO in the gas phase during electron irradiation was consistent with dissociation of the NO ligands in the CTN multilayer films at electron energies of 500 eV.[24] In contrast, NO and CO are both added to the gas phase during electron exposures at 100 eV shown in Figure 2-3. QMS measurements at m/z= 32 also observed no O_2 in the gas phase during electron exposures at 100 eV.

2.4.2 Electron Energy Dependence of Film Growth

The Co film growth was also examined using different electron energies. These experiments were performed after many previous Co deposition experiments. The results for electron energies of 75, 100, 125, 150 and 175 eV are displayed in Figure 2-4.

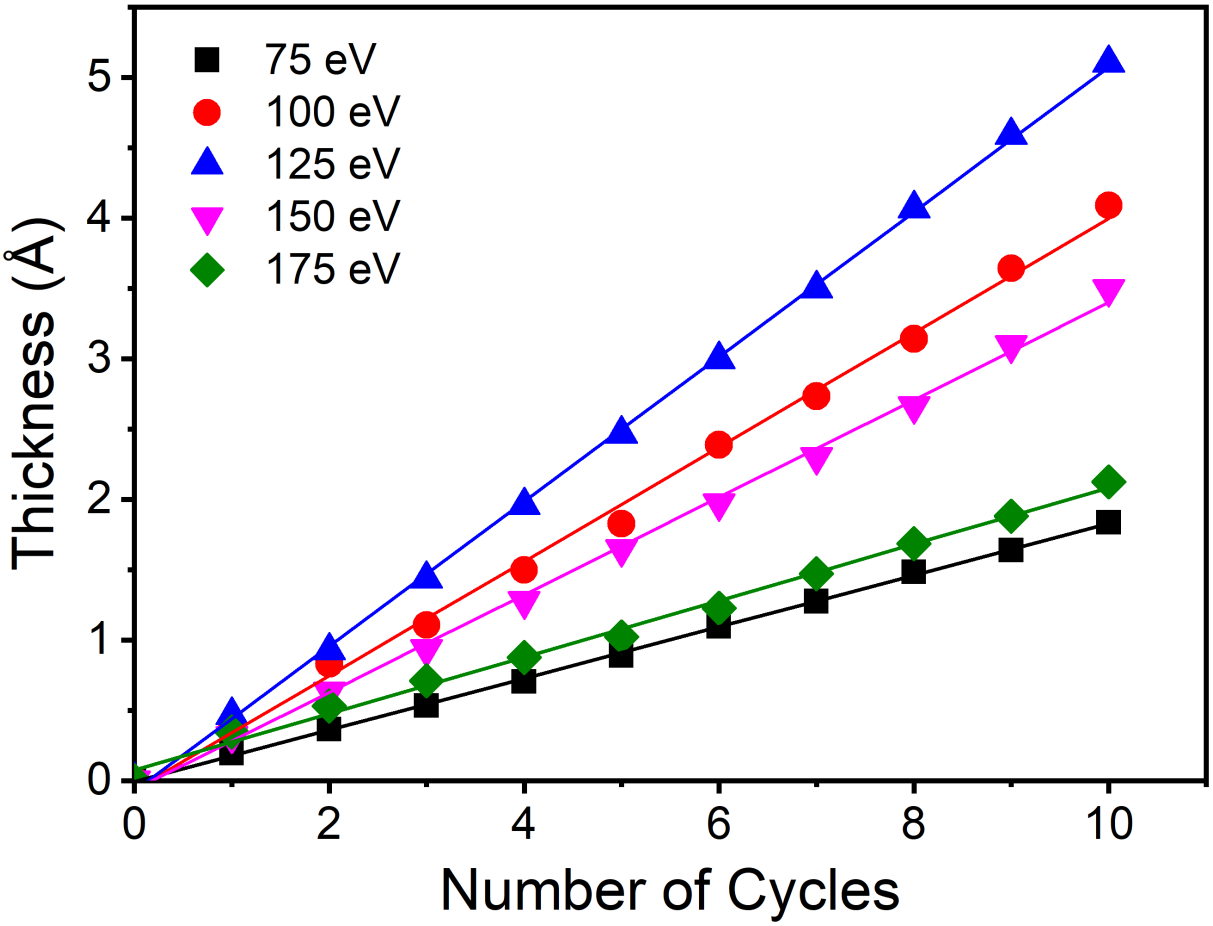

Figure 2-4. Film thickness measured by in situ ellipsometry vs the number of reaction cycles during Co growth at various electron energies.

The timing of the pulsing sequence was (0.1, 75, 50, 240, 175). The electron current from the filament was 100 μA. For these experiments, the electron current incident on the sample was lower at 24-28 μA. The in situ ellipsometry measurements were again conducted after each

reaction cycle. There is no nucleation period because the Co film growth was conducted on a previous Co film for each electron energy.

The Co film growth per cycle (GPC) is dependent on electron energy. The GPC is not in saturation at these lower incident electron currents and relatively short electron exposure times. Under saturating, self-limiting growth conditions, the GPC would have been constant versus electron energy. The GPC is 0.18 Å/cycle at 75 eV. The GPC increases with electron energy and reaches a maximum GPC of 0.50 Å/cycle at 125 eV. The GPC at higher electron energies and is then reduced to a GPC of 0.34 Å/cycle at 150 eV and 0.21 Å/cycle at 175 eV. The GPC values versus electron energy are summarized in Figure 2-5.

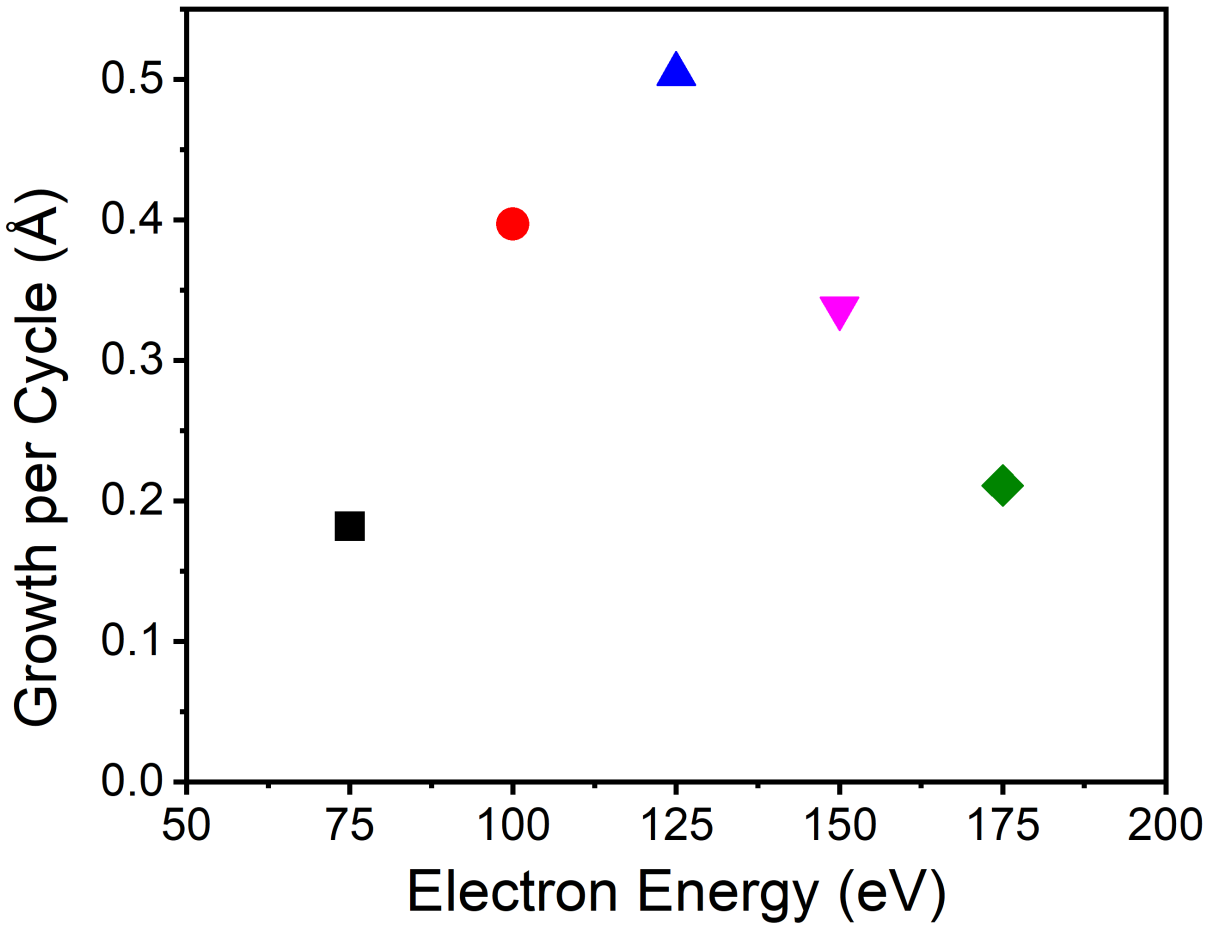

Figure 2-5. Summary of growth per cycle for Co growth vs electron energies. The maximum growth per cycle occurs at 125 eV.

The GPC of 0.34 Å/cycle at 150 eV is lower than the GPC of 1.3 Å/cycle at 150 eV observed in Figure 1-1 and Figure 1-2. Although the electron current from the filament was the same at 100 μA, the incident electron currents at the sample were lower at 24-28 μA. These lower electron currents may have been caused by changes to the electron gun resulting from Co deposition. The CTN can adsorb on the surfaces of the electron gun at room temperature. Over multiple Co deposition experiments, Co will deposit on the grid and anode of the electron gun. This Co deposition may alter the electron current from the electron gun. The lower growth rate of 0.34 Å/cycle at 150 eV is attributed to the lower incident electron currents.

2.4.3 Spatial Distribution of Film Deposition

The Co film was also readily observed on the Si wafer. A picture of the Co film on the Si wafer is shown in Figure 2-6.

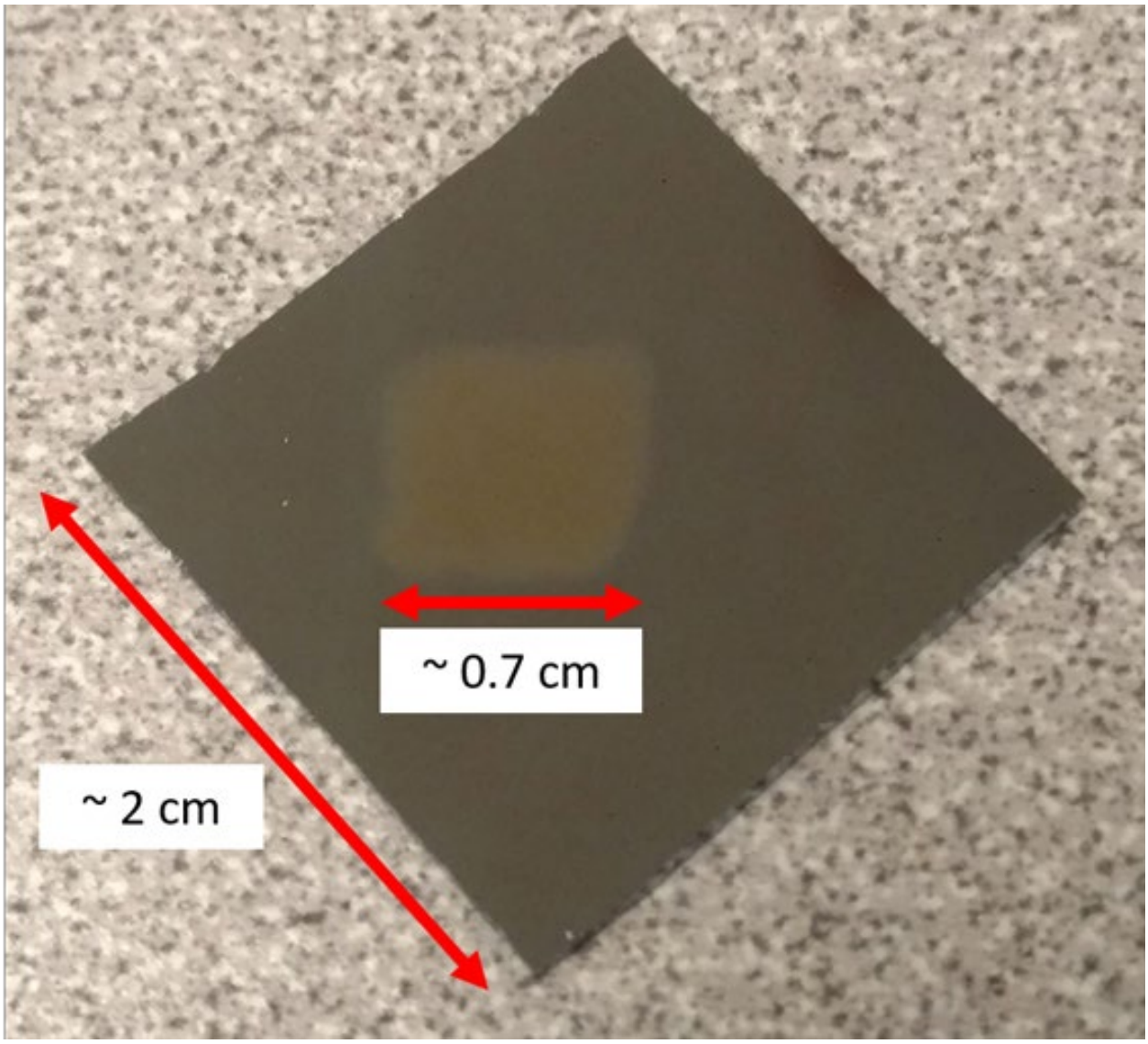

Figure 2-6. Picture of the Co film on a silicon wafer after 223 reaction cycles with an electron energy of 100 eV. Area-selective deposition limits the Co film to a diameter of ~7 mm.

This Co film was deposited using 223 reactions cycles at room temperature. The electron energy was 100 eV. Each reaction cycle had a timing for the pulse sequence of (0.1, 75, 50, 60,

175). The electron current from the filament was 100 μA. The incident electron current on the sample was 45 μA. The Co film is selectively deposited where the electron current was incident on the Si wafer. The Co film has a shiny silver-tan color. The thickness of this Co film measured using ex situ ellipsometry was 110 Å. Assuming a nucleation period that may vary from 20-45 cycles, this film thickness is consistent with a growth rate ranging from 0.54-0.62 Å/cycle at 100 eV. The diameter of the Co film is approximately 7 mm.

The film thickness could also be profiled using ex situ spectroscopic ellipsometry. The results for one of these spatial profiles are displayed in Figure 2-7.

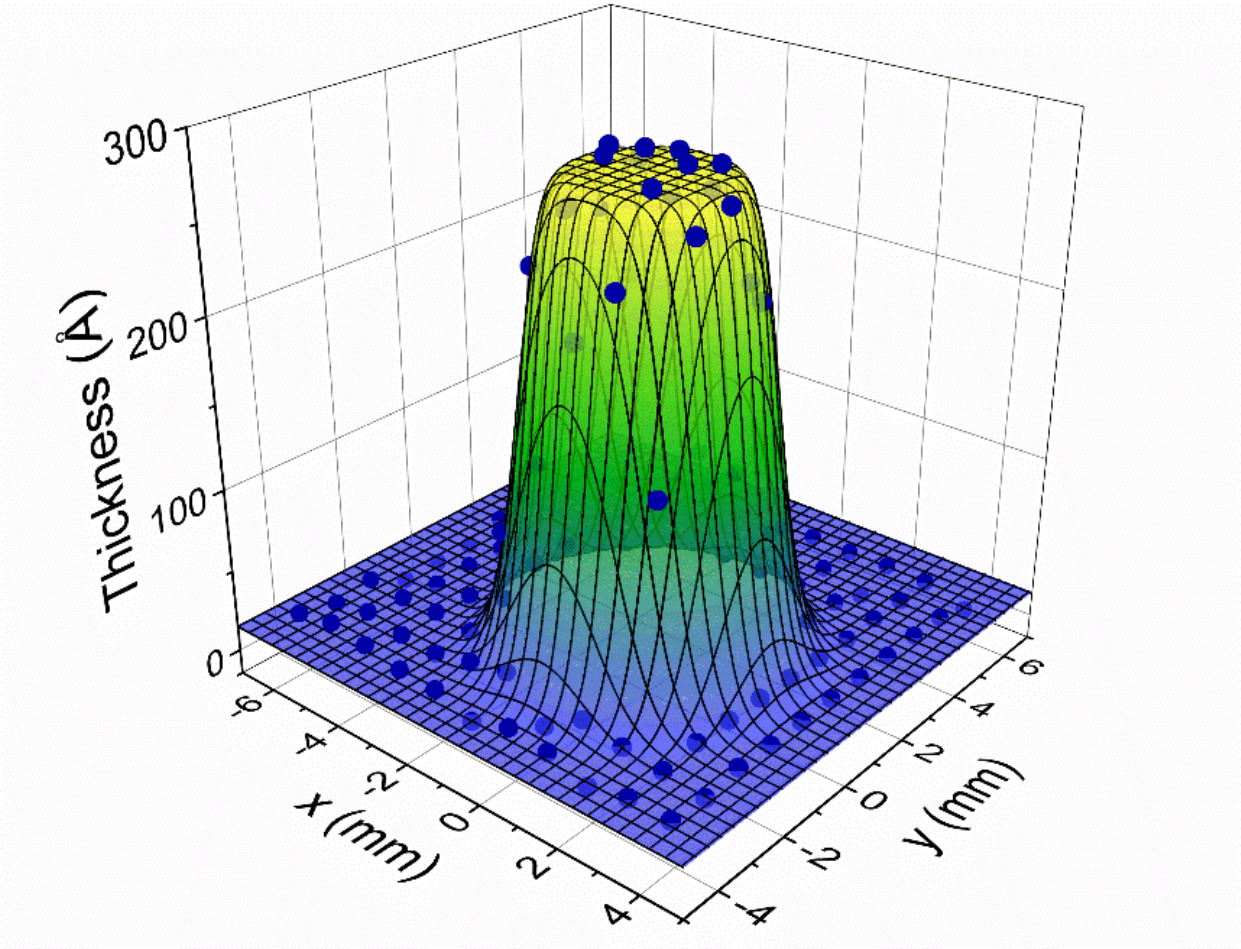

Figure 2-7. Spatial map of the Co film on a silicon wafer as measured by ex situ spectroscopic ellipsometry. A distinctive flat top is observed on the Co film deposition. Co film thickness of ~289 Å is measured after 198 reaction cycles with an electron energy of 200 eV.

This Co film was deposited using 198 reaction cycles at room temperature. The electron energy was 200 eV. Each reaction cycle had a timing for the pulse sequence of (0.1, 75, 50, 960, 175). The electron current from the filament was 100 μA. The incident electron current on the sample was 21 μA. The diameter of the Co film deposition is ~7 mm in agreement with the picture of the Co film in Figure 2-6. In addition, the top of the spatial profile in Figure 2-7 has a flat top. This flat top indicates that the electron induced desorption has reached saturation and removed nearly all of the CO and NO ligands over the central portion of the electron beam. Similar flat top spatial profiles were observed in previous studies of Si EE-ALD and BN EE-ALD.[30, 57] Based on an average of 9 points at the flat top of the spatial profile in Figure 2-7, the thickness at the flat top was 289 Å with a standard deviation of ±10 Å.

This film thickness of 289 Å can be used to estimate a Co growth rate. The nucleation period may be shorter at the long electron exposure times of 960 s per reaction cycle utilized for the film growth shown in Figure 2-7. Assuming a nucleation period of ~20 cycles, this film thickness of 289 Å is consistent with a growth rate of 1.6 Å/cycle at 200 eV. Assuming no nucleation period yields a growth rate of 1.5 Å/cycle. This high growth rate at 200 eV may be attributed to the long electron exposures of 960 s. These long electron exposures may be needed to reach saturation and desorb the CO and NO ligands over a significant fraction of the electron beam distribution on the surface.

The saturation behavior and corresponding high growth rates revealed from the results in Figure 2-7 indicate that EE-ALD could be very useful. However, the long electron exposures of 960 s per reaction cycle required to obtain saturation behavior and high growth rates at incident electron currents of 21 μA from the electron flood gun do not facilitate rapid Co growth. Much higher incident electron currents are needed to produce Co film growth in more reasonable times.

A higher electron current source, such as a hollow cathode plasma electron source, could be employed to address this issue.[69]

2.4.4 Film Composition

The composition of the Co films was examined using ex situ XPS. These XPS measurements utilized the same Co film that was used for the spatial profile shown in Figure 2-7. The ex situ XPS analysis was performed after the Co film had been exposed to atmosphere. The XPS depth-profile analysis of the Co film is shown in Figure 2-8.

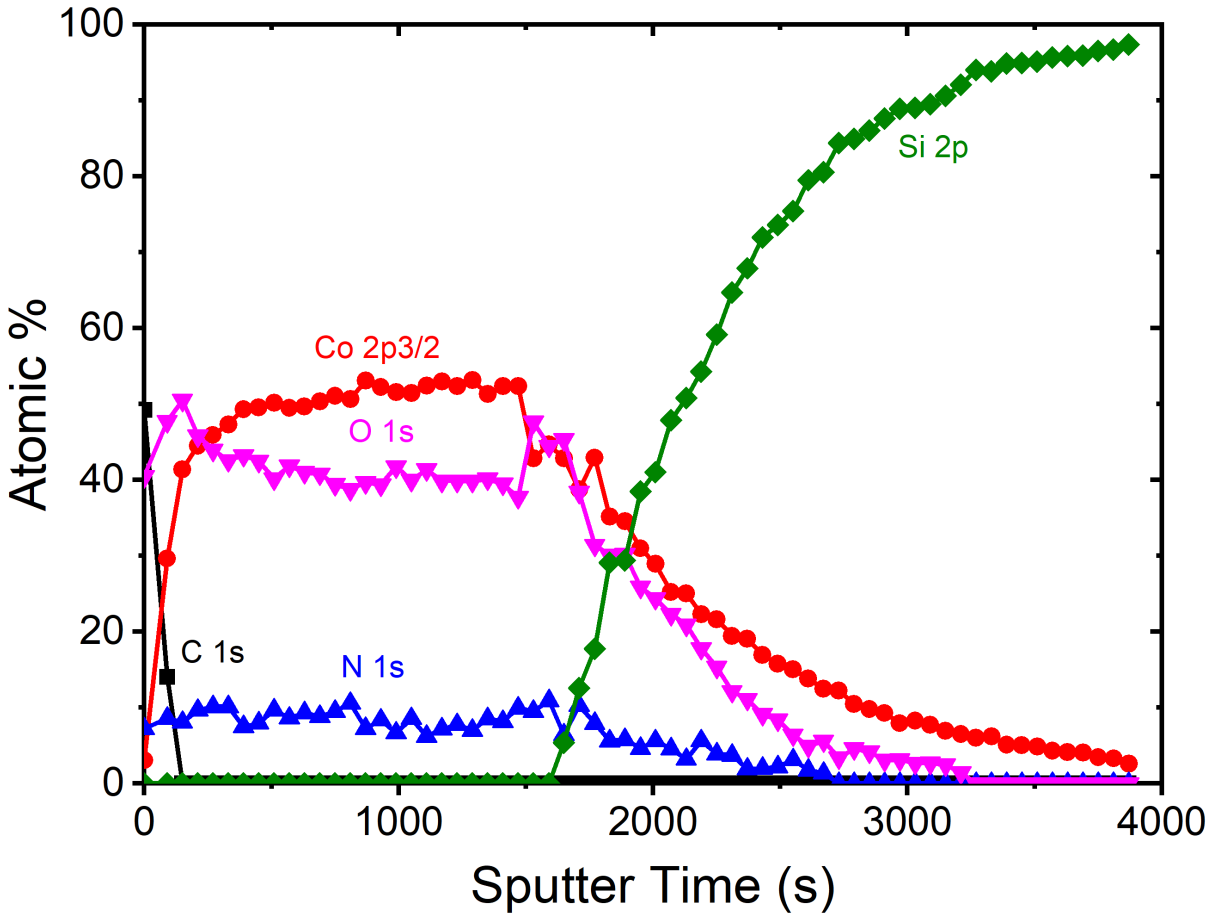

Figure 2-8. Atomic percentage vs sputter time during XPS depth profile analysis of the Co film shown in Figure 2-7.

After a sputter time of 990 s, the XPS measurements revealed that the composition of the films was 51.6 at% Co, 41.7 at% O, and 6.7 at% N. The samples contained a large amount of oxygen impurities because the Co films are easily oxidized in air.

The C XPS signal was below the XPS threshold intensity after sputtering into the Co film. The N/Co XPS signal ratio of 6.7 at%/51.6 at% = 0.13 indicates that approximately 13% of the nitrosyl ligands on the CTN precursors that lead to Co deposition are dissociated during the electron exposures at 200 eV. In contrast, the lack of C XPS signals argues that the carbonyl ligands on CTN are desorbed cleanly during the electron exposures at 200 eV.

These XPS results for the Co film composition are fairly similar to earlier studies of Co FEBID using CTN and much higher electron energies of 5-20 keV. There was nitrogen in these Co depositions at 12-20 at% and smaller levels of carbon at ≤ 10 at%.[13, 70] Additional studies have also explored electron beam induced reactions in CTN multilayers at -168°C using lower electron energies of 500 eV.[24] These investigations are consistent with NO dissociation and CO desorption during electron irradiation.[24] After longer electron exposures at 500 eV, the partially decarbonylated CO species undergo electron stimulated CO decomposition.[24] The remaining CO species and most of the dissociated carbon atoms then leave the surface after annealing to room temperature.[24]

For the current studies, there is less NO dissociation and no observed CO decomposition after electron exposures at 200 eV for CTN adsorbed on the Co films at room temperature. These differences may result from the lower electron energy of 200 eV. The different behavior may also be attributed to the lower coverages of adsorbed CTN on the Co films at room temperature. Additional experiments at various temperatures, surface coverages and electron

energies are required to understand the film composition resulting from electron induced processes.

The high-resolution Co 2p XPS signal obtained after 990 s of sputtering into the Co film is displayed in Figure 2-9.

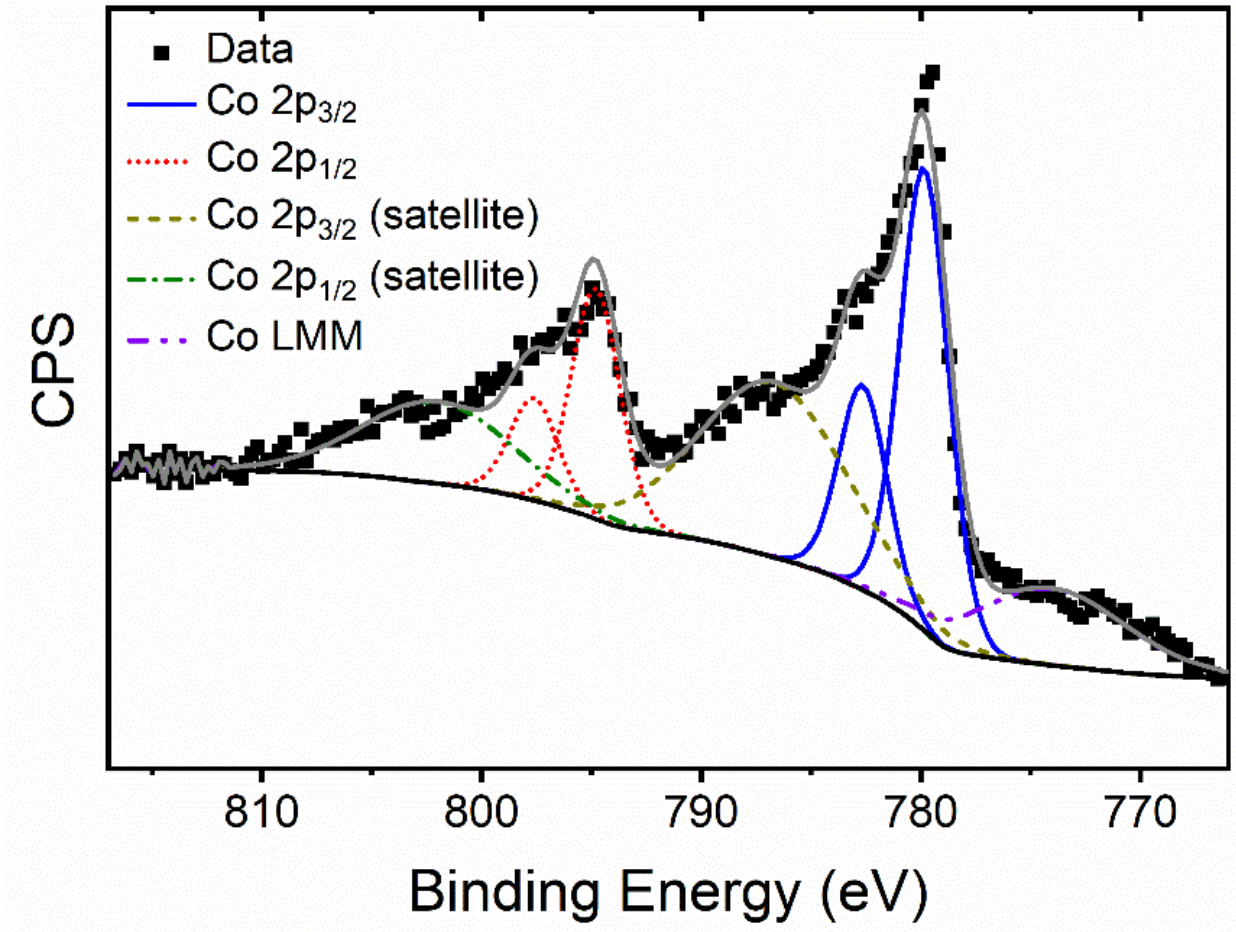

Figure 2-9. Counts per second vs binding energy for the Co 2p XPS signal obtained after 990 s of sputtering into the Co film shown in Figure 2-8. Peaks were fit using Co 2p3/2,Co2p1/2, shake-up satellites and Co LMM Auger features.

This XPS spectrum is consistent with cobalt in the 2+ oxidation state.[50] The peaks were fit with features for Co $2p_{3/2}$, Co $2p_{1/2}$, shake-up satellites and Co LMM Auger signals. Each of the Co 2p peaks was fit with two peaks to account for multiplet splitting.[50, 71] The strong intensity of the

Co shake-up satellites relative to their Co 2p transitions is indicative of Co(II) oxide.[50, 71] The binding energies of the two Co $2p_{3/2}$ peaks are 781.8 and 779.8. These peak positions are in agreement with CoO.[50]

There may also be contribution in Figure 2-9 from some Co(III) species. The possible presence of Co(III) oxides, such as Co_2O_3 and Co_3O_4, is complicated by the susceptibility of these oxides to ion induced reduction during sputtering.[72] More accurate compositional analysis of the Co films prior to atmospheric exposure must be performed using in situ techniques such as in situ Auger electron spectroscopy. The Auger spectrometer in the analysis chamber was not operational during the course of these experiments.

2.4.5 Electron Induced Desorption Cross Section from Film Spatial Profile

The spatial profile in Figure 2-7 was used to calculate the electron induced desorption cross section. The time dependent surface coverage for a monolayer during electron induced desorption with a uniform electron flux can been modeled as:[30, 57, 73]

$$\Theta(t) = \Theta_0 \, e^{[-(J \sigma / q A)t]} \qquad \text{(Eq. 2.1)}$$

In this expression, J is the electron current, A is the area of the irradiated surface, q is the charge of an electron, and σ is the total cross section for electron induced desorption. Θ_0 corresponds to the initial surface coverage of CO and NO species from the adsorbed CTN. The Co atom coverage, X(t), deposited during one reaction cycle is proportional to the number of open sites on the surface resulting from the time-dependent electron induced desorption of CO and NO species. The Co atom coverage can be expressed as:[30, 57]

$$X(t) \sim \big(1 - \Theta(t)\big) \qquad \text{(Eq. 2.2)}$$

The thickness of the Co film, T(t), can then be described as:[30, 57]

$$T(t) = \alpha \, (1 - \Theta(t)) \qquad \text{(Eq. 2.3)}$$

In this expression, α is a constant that includes the number of reaction cycles and the conversion between Co atom coverage deposited per reaction cycle and the Co film thickness deposited per reaction cycle. This conversion could also account for the expansion of the Co film upon atmospheric oxidation to form CoO.

The electron beam from the electron flood gun has a Gaussian profile. The electron flux from a normalized 2D-Gaussian is:[57]

$$J[x,y] = J_0 \frac{1}{2\,\pi\,w_x\,w_y}\, exp\left[-\frac{(x-x_c)^2}{2\,w_x^2} - \frac{(y-y_c)^2}{2\,w_y^2}\right] \quad \text{(Eq. 2.4)}$$

Inserting this expression for electron flux in Eq. 2.1 yields an expression for the thickness of the oxidized Co film corresponding to different positions on the spatial profile of the electron beam. The resulting expression for the spatial distribution of the film thickness is:[57]

$$T[x,y] = \alpha\left(1 - exp\left[-t\,\frac{\sigma}{q}\,J_0\,\frac{1}{2\,\pi\,w_x\,w_y}\,exp\left[-\frac{(x-x_c)^2}{2\,w_x^2} - \frac{(y-y_c)^2}{2\,w_y^2}\right]\right]\right) + T_0 \quad \text{(Eq. 2.5)}$$

The offset, T_0, accounts for deposition outside of the primary electron beam.

Eq. 2.5 can be fit to the spatial profile of the film shown in Figure 2-7. The fitting parameters were α, σ, the center of the Gaussian profile at x_c and y_c, the width of the Gaussian profile determined by w_x and w_y, and T_0. This fit to the spatial profile yielded the electron induced desorption cross-section. The best fit was consistent with a cross section of $\sigma = 2 \times 10^{-17} \pm 6 \times 10^{-18}$ cm^2. In addition, $\alpha = 269 \pm 12$ Å, $w_x = 0.70 \pm 0.05$ cm, $w_y = 0.70 \pm 0.05$ cm and $T_0 = 15 \pm 4$ Å. The low background thickness of $T_0 = 15$ Å may be film growth resulting from secondary electron scattering.

2.4.6 Measured and Predicted CO Throughput During Electron Irradiation

The ESD cross section can be used to compare the measured and predicted CO throughput during electron irradiation. The mass spectrometer results shown in Figure 2-3 can

be employed to estimate the partial pressures of gaseous species by converting the ion currents to pressures. The mass spectrometer calibration yielded a conversion factor of 5 x 10^{-4} A/Torr for CO. The pressure increase produced by the electron current in Figure 2-3 was then determined by dividing the increase in ion current by the conversion factor. For the ion current increase of 0.17 x 10^{-12} A for the m/z = 28 signal (CO) in Figure 2-3 during electron irradiation, the pressure increase is ΔP = 3.4 x 10^{-10} Torr.

The CO pressure increase can then be employed to calculate the CO throughput, Q. This calculation uses the relationship Q = SΔP where S is the pumping speed. Given S = 250 L/s for CO and ΔP = 3.4 x 10^{-10} Torr, a CO throughput of Q = 3.0 x 10^{12} CO/s is obtained from the ~0.5 cm^2 electron irradiated area. The measured CO throughput can then be compared with the predicted CO throughput defined as the desorption of CO ligands per second from the ~0.5 cm^2 electron irradiated area.

The electron current on the sample in Figure 2-3 is 45 μA over an area of ~0.5 cm^2. The electron flux can be obtained using the relationship $\Phi = I/Aq$ where Φ is the electron flux, I is the electron current, A is the irradiated area, and q is the electron charge. Based on this relationship, the electron flux is Φ = 5.6 x 10^{14} electrons/(cm^2 s). The ESD cross section of 2.0 x 10^{-17} cm^2 can then be used to predict the CO throughput.

The normalized CO coverage, Θ/Θ_0, will be reduced by CO ESD according to $\Theta/\Theta_0 = \exp[-\sigma D]$.[10, 11, 30] In this expression similar to Eq. 2.1, D is the electron dose defined as the product of the electron flux, Φ, and time. For an exposure of 1 s, the electron dose is D=5.6 x 10^{14} electrons/(cm^2 s) x 1 s = 5.6 x 10^{14} electrons/cm^2. This electron dose for 1 s yields a normalized CO coverage of Θ/Θ_0 = 0.989. Likewise, 1.1% of the CO ligands are desorbed in 1 s.

The absolute CO coverage can then be estimated from the growth rate and the composition of the resulting cobalt film. A growth rate of 1.5 Å/cycle was obtained from the ex situ spectroscopic ellipsometry results in Figure 2-7 assuming no nucleation period. The composition of these cobalt films was CoO after oxidation resulting from atmospheric exposure. Using a CoO density of 6.44 g/cm^3, the growth rate of 1.5 Å/cycle is equivalent to 7.76 x 10^{14} CoO units/(cm^2 cycle).

Given 3 CO ligands per $Co(CO)_3NO$ precursor, there are 2.3 x 10^{15} CO ligands/cm^2 on the surface after $Co(CO)_3NO$ exposures that yield a growth rate of 1.5 Å/cycle. This estimate assumes that the Co film deposited in vacuum was converted to a CoO film after oxidation by atmospheric exposure. If the electron exposures over 0.5 cm^2 for 1 s desorb 1.1% of this CO coverage, the CO throughput is 1.3 x 10^{13} CO/s. This predicted CO throughput of 1.3 x 10^{13} CO/s can be compared with the measured CO throughput of 3.0 x 10^{12} CO/s. The prediction of the CO throughput from the ESD cross section and the estimated CO absolute surface coverage is within a factor of 4 of the measured CO throughput. This agreement is good given all the assumptions and estimates used to obtain this comparison between the measured and predicted CO throughput during electron irradiation.

2.4.7 Comparison Between Spatial Profiles for Electron Current and Co Deposition

Figure 2-10

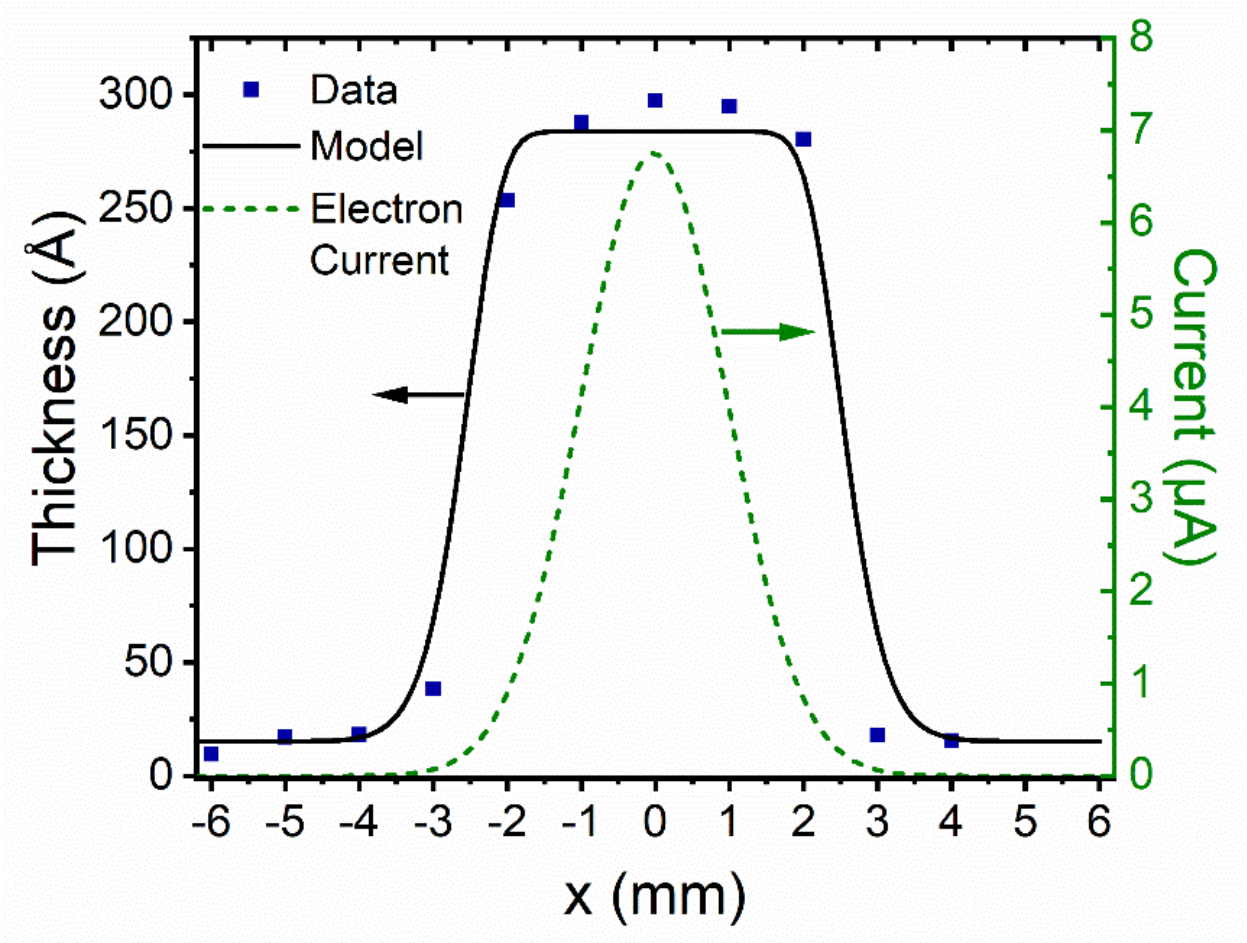

Figure 2-10. Spatial profiles of the Gaussian electron beam and Co deposition for results in Figure 2-7. Flat top on Co deposition extends over the central area of the electron beam.

displays a cross section of the spatial profile of the film thickness from Eq. 2.5 that fits the individual film thicknesses displayed in Figure 2-7. Figure 2-10 also shows the spatial profile of the Gaussian electron beam that fits the deposition results in Figure 2-7. Individual film thicknesses measured through a cross section of the deposited film are also displayed in Figure 2-10. The width of the Gaussian profile of the electron beam is smaller than the diameter of the film visible on the silicon wafer. A comparison between the spatial profiles of the electron beam and deposition reveals that the flat top of the film is obtained over a significant fraction of the electron beam.

The distinctive flat top on the Co deposition indicates that saturation was achieved over the central area of the electron beam for the long electron exposure times of 960 s used to obtain the spatial profiles shown in Figure 2-7 and Figure 2-10. Calculations can be performed to predict the spatial profile of the deposition for different electron exposure times assuming the reactions conditions in Figure 2-7 with a cross section of $\sigma = 2 \times 10^{-17}$ cm^2. These predictions for electron exposure times from 15 to 3840 s are shown in Figure 2-11.

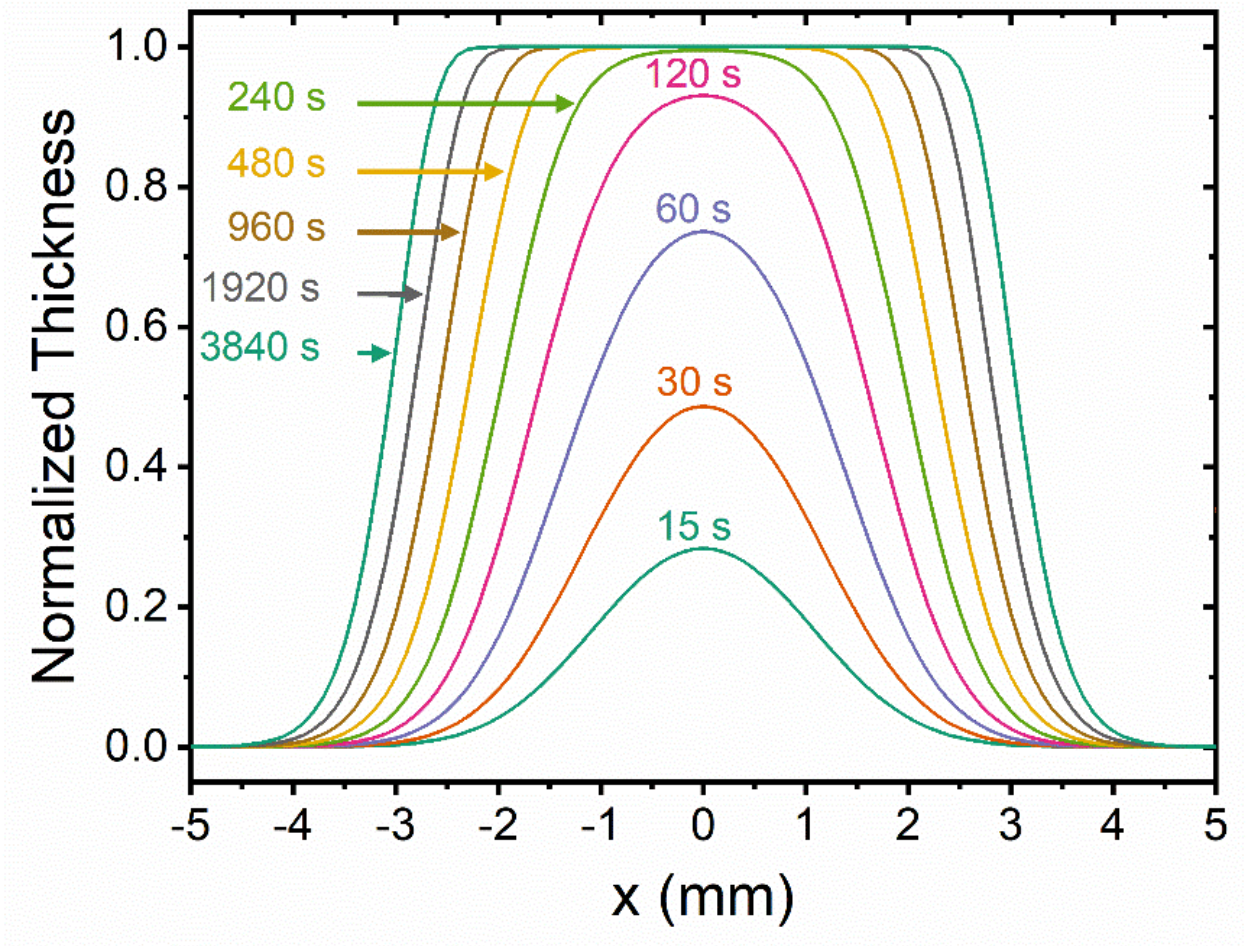

Figure 2-11. Predicted spatial profile of Co deposition vs electron exposure time using an electron induced cross section obtained from results in Fig. 7. Saturation behavior is observed for electron exposure times ≥240 s.

The thicknesses are normalized to the thickness obtained at saturation when electron induced desorption removes nearly all of the CO and NO surface species during the electron exposures.

Figure 2-11 shows that electron exposures <240 s do not display saturation behavior or obtain the maximum film thickness per reaction cycle. Longer electron exposures >240 s progressively reach larger amounts of saturation. These longer electron exposures produce the maximum film thickness per reaction cycle over a greater fraction of the spatial profile of the electron beam. Consequently, the size of the flat top area is larger with increasing electron exposure times.

2.4.8 Electron Induced Desorption Cross Section

The electron induced desorption cross section of $\sigma = 2 \times 10^{-17}$ cm^2 for Co growth is in good agreement with measured electron induced desorption cross sections derived from other recent film growth studies. An electron induced desorption cross section of $\sigma = 5.8 \times 10^{-17}$ cm^2 was measured for hydrogen desorption from Si during Si EE-ALD at 100 eV.[30] An electron induced desorption cross section of $\sigma = 4.2 \times 10^{-17}$ cm^2 was measured for hydrogen desorption from borazine during BN EE-ALD at 100 eV.[57] These cross sections are all higher than typical ESD cross sections of $\sigma = 10^{-23}$–10^{-20} cm^2 that have been measured for the desorption of ionic species and $\sigma = 10^{-20}$ – 10^{-18} cm^2 that have been reported for the desorption of neutral species.[14, 74] These cross sections from recent film growth studies are also slightly smaller than typical cross sections of ~10^{-16} cm^2 that have been reported for EID at 100 eV.[14]

This electron induced desorption cross-section of 2×10^{-17} cm^2 can also be compared with the cross sections for EID for gas phase CTN that have been performed in the electron energy range from 0 to 140 eV.[66] These measurements observe the dissociation ionization of CTN with a threshold at an electron energy of ~20 eV. The highest cross section of 4.5×10^{-16} cm^2 is

observed for Co^+ production at electron energies from 50-100 eV.[66] The next highest cross section of 2.5 x 10^{-16} cm^2 is measured for $[CoCO]^+$ production. A cross section of 1.0 x 10^{-16} cm^2 is determined for $[Co(CO)_2NO]^+$ production.[66]

The fairly close agreement between the electron induced desorption cross section from this study and the absolute cross sections for the EID of gas phase CTN suggests that CTN adsorbs as a physisorbed molecule on the Co surface. The adsorbed CTN precursor may not be significantly perturbed by the Co surface. The adsorbed CTN then undergoes ligand loss by mechanisms similar to the dissociative ionization of gas phase CTN.

The dependence of the absolute cross sections on electron energy for the dissociative ionization of gas phase CTN is also fairly similar to the dependence of the electron induced desorption cross section on electron energy that is shown in Figure 2-5. The electron induced desorption cross section increases with electron energy and peaks at 125 eV as displayed in Figure 2-5. The cross section then decreases at higher electron energies. In comparison, the absolute cross sections for the dissociative ionization of gas phase CTN have a threshold at ~20 eV, display their maximum values at electron energies of 50-100 eV, and then decrease for electron energies >100 eV.[66]

Although the Co growth rate versus electron energy in Figure 2-5 is comparable to the dissociative ionization cross section for gas phase CTN versus electron energy, there is still a possibility that the desorption of CO and NO ligands during Co growth could be dependent on low energy secondary electrons that are produced by the primary electrons. The electron beam induced deposition of Pt from methylcyclopentadienyl-platinum-trimethyl ($MeCpPtMe_3$) has been studied at electron energies from 40-1000 eV.[20] The results for Pt deposition yield versus electron energy displayed a maximum at 140 eV. The increasing Pt yield versus electron

energies up to 140 eV and then decreasing yield at electron energies >140 eV is similar to the results observed for Co deposition in Figure 2-5.[20]

The Pt deposition results from $MeCpPtMe_3$ have be explained in terms of the primary electrons inducing secondary electrons at < 20 eV.[20, 75] These secondary electrons can then decompose the $MeCpPtMe_3$ via the DEA mechanism. However, there is ambiguity because the EID cross sections and the secondary electron emission yields both have their maximum values at electron energies of 80-150 eV.[15, 76] Identifying whether the electron-enhanced Pt deposition from $MeCpPtMe_3$ occurs through the EID or DEA mechanism is not straightforward. Similar uncertainty exists for the electron-enhanced growth of cobalt in this study.

2.5 Conclusions

Cobalt thin films were deposited at room temperature using sequential cobalt tricarbonyl nitrosyl (CTN, $Co(CO)_3NO$) and low energy (75-175 eV) electrons exposures from an electron flood gun. During this electron-enhanced growth process, the CTN molecules were first adsorbed on the substrate. The carbonyl and nitrosyl ligands from the adsorbed CTN were then removed by electron induced desorption. New adsorption sites were produced by the removal of the CO and NO ligands. These new adsorption sites on the substrate allowed additional CTN to adsorb during subsequent CTN exposures.

The film thickness during the electron-enhanced growth was monitored using in situ ellipsometry. Depending on the reaction conditions, the Co growth rates were as large as 1.3 Å/cycle. Using equivalent reaction conditions at lower incident electron currents, the maximum growth rate was measured at an electron energy of 125 eV. The CTN adsorption and the removal of the carbonyl and nitrosyl ligands could also be observed using in situ ellipsometry.

The desorption of CO and NO during electron exposures was also confirmed using quadrupole mass spectrometer measurements.

XPS measurements revealed that the Co films were easily oxidized after atmospheric exposure. XPS analysis also detected some N in the Co film produced during electron exposures at 200 eV. The N/Co XPS signal ratio was consistent with the dissociation of 13% of the NO ligands on the CTN precursors that produce the Co film. The absence of C XPS signals from the Co films indicated that the CO ligands on CTN were completely desorbed by the electron exposures at 200 eV.

The Co films were deposited only on the surface area illuminated by the electron beam. The spatial profile of the Co film was mapped by ex situ spectroscopic ellipsometry. A distinctive flat top was observed for the spatial profile that was consistent with the electron induced desorption of nearly all the CO and NO surface coverage from the central area of the electron beam. Fitting the spatial profile of the Co film yielded an electron induced desorption cross section of $\sigma = 2 \times 10^{-17}$ cm^2 at 200 eV. This cross section is only slightly less than the cross sections for the EID of CTN in the gas phase. The dependence of the electron induced desorption cross section on electron energy was also similar to the electron energy dependence of the EID cross section for CTN in the gas phase. This agreement suggests that CTN is adsorbed on the Co surface as a nearly unperturbed, physisorbed molecule.

There is some ambiguity about the electron induced mechanism for Co growth. The electron energy dependence of secondary electron yield is similar to the electron energy dependence of EID of CTN. The primary electrons could be directly causing EID or ESD via a Menzel-Gomer-Redhead or Knotek-Feibelman mechanism. Alternatively, the primary electrons

could be generating secondary electrons that then lead to dissociation of CTN via a DEA mechanism.

3 Hollow Cathode Plasma Electron Source for Low Temperature Deposition of Cobalt Films by Electron-Enhanced Atomic Layer Deposition

Zachary C. Sobell,[1] Andrew S. Cavanagh,[1] David R. Boris,[2] Scott G. Walton,[2] and Steven M. George[1]

[1]Department of Chemistry, University of Colorado, Boulder, Colorado 80309-0215
[2]Naval Research Laboratory 4555 Overlook Ave SW, Washington, DC 20375

3.1 Abstract

The development of a hollow cathode plasma electron source (HC-PES) facilitated the rapid nucleation and low temperature deposition of thin cobalt films using electron-enhanced atomic layer deposition (EE-ALD). The Co EE-ALD was performed near room temperature (30-60 °C) using sequential exposures of cobalt tricarbonyl nitrosyl ($Co(CO)_3NO$, CTN) and low energy (100-200 eV) electrons. Electron-stimulated desorption (ESD) of CO and NO surface species create open sites for precursor adsorption to facilitate low temperature film growth. The HC-PES displayed high electron currents, rapid ALD cycling and low susceptibility to chemical interference. Electron steering optics were also used to mitigate the effects of sputtering in the HC-PES. The high electron currents from the HC-PES yielded rapid nucleation of cobalt films in as few as 4 EE-ALD cycles with Co growth rates over 2 Å/cycle on areas >4 cm^2. In high aspect ratio structures, transmission electron microscopy (TEM) and energy dispersive spectroscopy (EDS) analysis revealed a 4:1 topographical selectivity in favor of horizontal compared with vertical surfaces. This selectivity was attributed to the directional electron flux from the HC-PES. This topographical area selective deposition suggests that Co EE-ALD may be successful in achieving bottom-up fill of trenches and vias.

3.2 Introduction

The use of low energy electrons can facilitate the growth of thin films of metals, dielectrics, and semiconductors through electron-enhanced atomic layer deposition (EE-ALD).[30, 36, 56-57] EE-ALD uses sequential exposure of precursors and low energy electrons to deposit thin films. The precursor molecule first adsorbs on the substrate. Subsequently, the low energy electrons desorb the ligands from the precursor via electron stimulated desorption (ESD).[26-27] The process of ligand desorption leaves behind open sites for further precursor adsorption. Repeating the precursor and low energy electron sequential exposures produces the EE-ALD film growth.

Similar to the behavior during thermal ALD,[1] both the electron exposure and precursor dose should display self-limiting behavior during EE-ALD. For the precursor dose, saturation is defined as the formation of one complete layer of precursor on the substrate. For the electron exposure, saturation is defined as the removal of all ligands from the saturated surface. Repetition of the sequential precursor and electron exposures should lead to thin film growth with Ångstrom-level precision.

Electron-enhanced thin-film growth has been demonstrated previously for the deposition of elemental silicon.[30] Silicon was deposited using sequential surface reactions with disilane (Si_2H_6) and low energy electrons as the reactants. The proposed mechanism was dissociative adsorption of disilane on the surface and then the removal of hydrogen by ESD using low energy electrons. The removal of hydrogen from the surface leaves behind dangling bonds on the silicon, which are then available for subsequent disilane adsorption. Silicon growth rates were determined to be 0.3 Å/cycle at room temperature and an electron energy of 100 eV.[30]

EE-ALD has also been demonstrated for the growth of hexagonal boron nitride (BN).[57] The h-BN was grown using borazine ($B_3N_3H_6$) and low energy electrons. Borazine is an ideal molecule for EE-ALD BN for several reasons. Borazine has a high vapor pressure and the 1:1 B:N stoichiometry needed for BN growth. Borazine also contains hydrogen which has been shown to be labile from surfaces under electron radiation.[30, 77-78] The BN EE-ALD was shown to be crystalline and turbostratic by XRD and TEM, respectively.[57] The proposed growth mechanism was the adsorption of the borazine rings parallel to the surface. The low energy electrons then desorb hydrogen, which allows the borazine rings to bond together. This hypothesis was supported by the distinct layered appearance of the BN films by TEM.[57]

The EE-ALD investigations discussed above utilized low energy electrons generated from an electron gun source based on thermionic emission.[30, 36, 56-57] Such electron gun sources are typically limited to fairly low electron currents because of space charge limits defined by the Child-Langmuir law.[79-80] In addition, the hot filament electron emitter is susceptible to chemical attack and deposition from the chemical precursors and reactive carrier gases. The time required for film growth is long because of the low electron flux. The processing times are further lengthened due to the pump and purge times needed to ensure minimal precursor reaction with the hot electron filament. A more chemically insensitive electron source would allow shorter pump and purge times, significantly decreasing the processing time.

Compared with electron guns based on hot filaments, hollow cathode plasma electron sources (HC-PES) are much more robust and produce higher currents.[81-82] These sources take advantage of the "hollow cathode effect", where electron confinement within a hollow cavity cathode leads to high plasma densities.[83] The plasma electrons can then be extracted from the hollow cathode plasma to yield high current electron beams. Numerous designs for the HC-PES

have evolved over the last thirty years.[69, 84-85] Many of these HC-PES designs conveniently operate at pressures of 10-500 mTorr.[86-90] These conditions are compatible with many material processing procedures.

Because of their high electron density and chemical insensitivity, hollow cathodes can be employed for many applications.[85, 91] The sputtered ions and plasma species from hollow cathodes have been used previously for thin film deposition.[92] The extracted electrons from hollow cathode plasmas can also be utilized to generate low electron temperature plasmas capable of delivering very low energy ions to adjacent surfaces in a wide variety of gases.[93-94] Electron beam injection from hollow cathodes has also been utilized for electron-enhanced surface etching.[95] This paper will utilize the HC-PES as a source of low energy electrons for Co EE-ALD.

This paper begins with a description of the basic operating principles of the HC-PES. The design and operation of the HC-PES is then discussed including the auxiliary electron steering optics needed to bend the electron beam to eliminate any downstream contamination from the hollow cathode. The paper then explores the results for Co EE-ALD obtained using the HC-PES. A direct comparison between the HC-PES and the previously employed thermionic emission electron gun is also given for Co EE-ALD. Finally, an examination of Co EE-ALD in high aspect ratio structures is presented using transmission electron microscopy (TEM) analysis.

3.3 Hollow Cathode Plasma Electron Source (HC-PES)

3.3.1 Hollow Cathode Plasma Operation

An illustration of the operation of a hollow cathode plasma is shown by the following steps in Figure 3-1.[96]

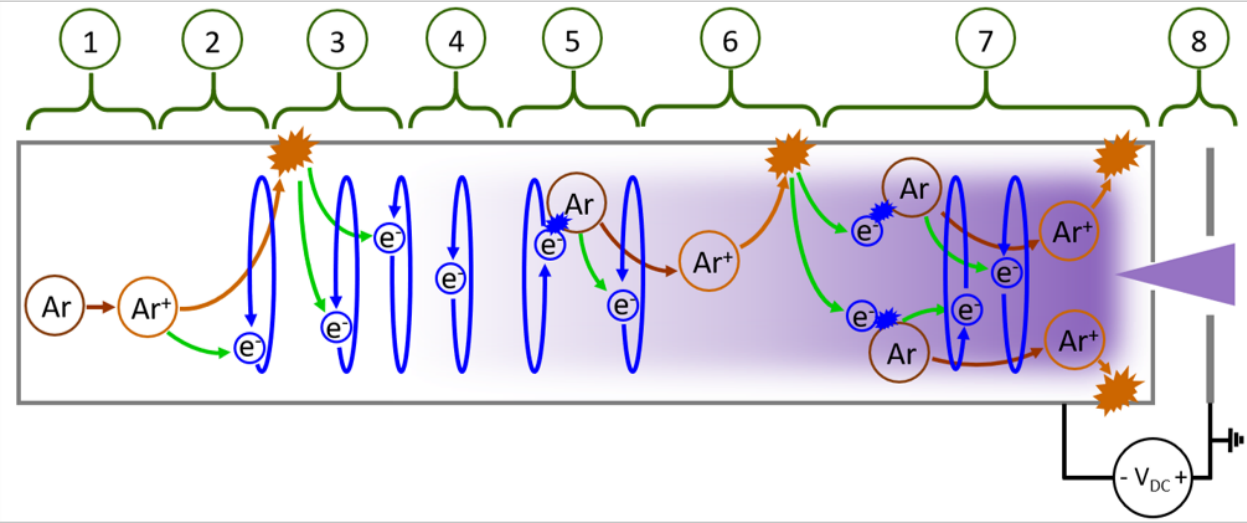

Figure 3-1. Operation of hollow cathode plasma can be described as: (1) an initial ionization event; (2) ion accelerated to cathode wall; (3) ion impacts on cathode wall produce secondary electrons; (4) secondary electrons are repelled from cathode walls and become trapped in the bulk plasma; (5) electrons oscillating about the axis of hollow cathode ionize more argon; (6) ionized argon is again accelerated to cathode wall and produces more secondary electrons; (7) positive feedback loop continues building up electron reservoir in hollow cathode; and (8) electron beam is extracted from the hollow cathode.

(1) The hollow cathode plasma starts with an initial ionization event inside the hollow cathode body. This ionization event creates an ion-electron pair. (2) The positive ion is accelerated toward the negatively biased walls of the hollow cathode and strikes the wall with a kinetic energy commensurate with the applied cathode voltage, i.e. several hundred eV in this work. (3) The resulting collision is energetic enough to liberate secondary electrons. (4) The electrons are repelled from the negatively biased walls, enter the bulk plasma, and become trapped between the walls.

The events in the hollow cathode continue as follows: (5) As the electrons oscillate within the hollow cathode cavity, they can ionize and excite additional argon atoms before losing most of their kinetic energy. (6) The newly created ions are again accelerated toward the walls, liberating more secondary electrons during their collision with the walls. (7) The secondary

electrons, as well as electrons from argon ionization, join the existing electrons in the hollow cathode body, further ionizing more neutral species. This process of ionization, acceleration, secondary electron liberation, electron oscillation and further ionization continues until reaching steady state. (8) When the potential of the hollow cathode plasma is sufficiently negative relative to the anode bias, an electron current can be extracted from the hollow cathode plasma.

3.3.2 Hollow Cathode Plasma Electron Source (HC-PES)

Figure 3-2a

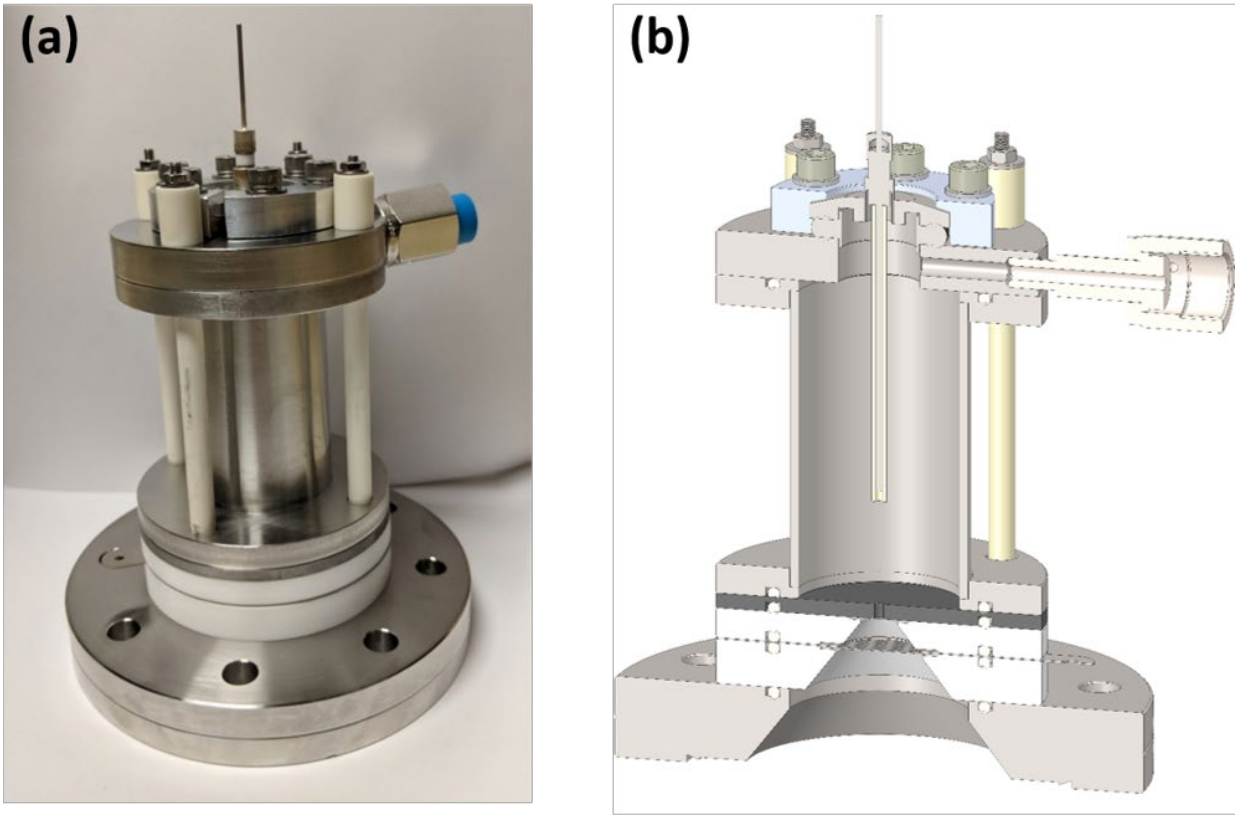

Figure 3-2. (a) Picture of assembled HC-PES before installation on the chamber. (b) Cross section of HC-PES.

shows a picture and Figure 3-2b displays a cross-sectional view of the HC-PES used in this study. This HC-PES was based on an earlier HC-PES design developed at the Naval Research Laboratory.[82, 97] The hollow cavity has an inner diameter of 3.5 cm and a length of 6.8 cm. Argon gas flows in at the top of the hollow cavity. The argon gas flows out an aperture at the bottom of the hollow cavity. The aperture also allows electrons to escape from the HC plasma source towards the bias grid. The diameter of the aperture is 1.5 mm.

The geometry is an important aspect of the HC-PES design.[85] In particular, when the aperture area is very small compared with the interior surface area of the hollow cathode, most of the discharge voltage appears across an ion sheath at the cathode wall. The corresponding electron flux required for quasi-neutrality appears at the anode grid which is positive with respect to the plasma potential. When the ratio of the effective anode surface area (A_a) to cathode surface area (A_c) satisfies $(A_a/A_c) < (m_e/m_i)^{1/2}$, where m_e and m_i are the electron and ion masses, respectively, the electrons leave the plasma source through an electron sheath at the anode, and the electron beam current can ideally be as large as the discharge current.[85, 98]

Figure 3-3

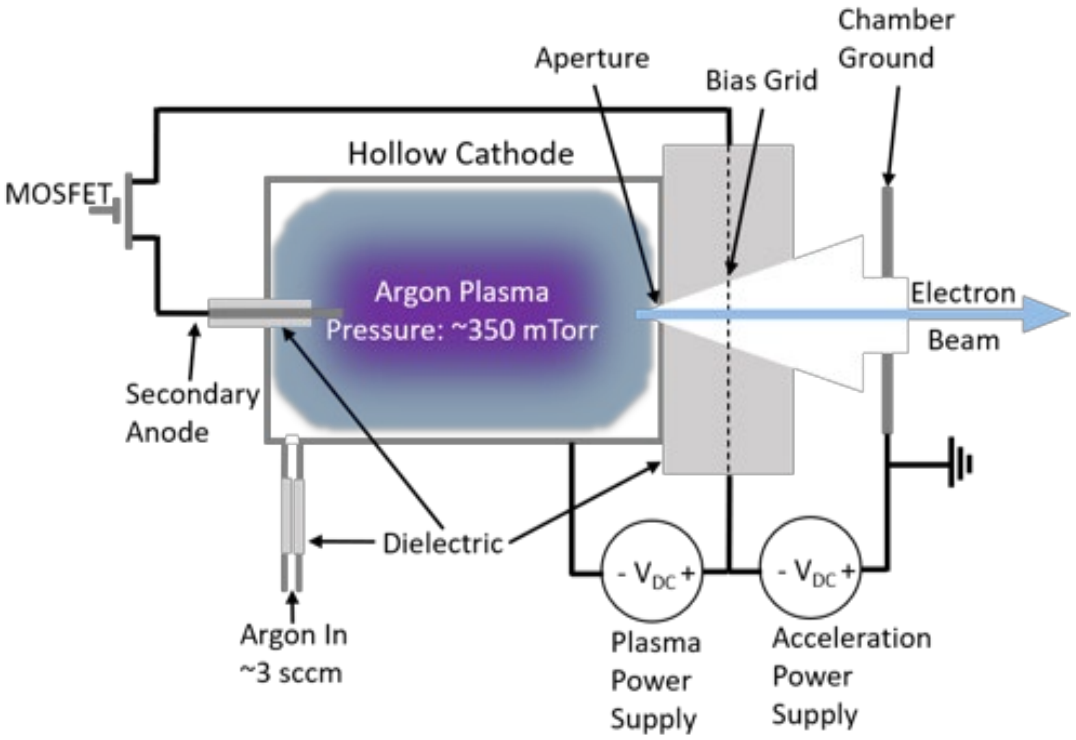

Figure 3-3. Schematic of the HC-PES showing the electrical diagram, gas flow and approximate pressures, plasma in the hollow cathode cavity, and emitted electron beam.

displays a schematic of the HC-PES. The HC-PES operates at an argon gas pressure of approximately 350 mTorr. This Ar pressure is determined using the Ar gas throughput and the estimated gas conductances. The wall of the hollow cavity is the cathode. The cathode is biased at -250 to -350 V relative to the bias grid voltage. The power supply for the HC plasma is referenced to the bias grid, which is biased with respect to ground.

Electrons extracted from the hollow cathode plasma are then accelerated by the grid bias. The nonambipolar flow conditions established by the geometry produces an electron sheath at the acceleration grid, with a potential that scales with electron temperature.[97] The electron beam energy will be the sum of the electron sheath potential and bias applied to the grid. The electron

sheath potential is not known in this work. Consequently, the beam energy will be reported as the grid bias. The electron sheath potential will typically add an additional 20-40 eV to the grid bias to define the electron energy.[97] A coaxial secondary anode inside the HC is incorporated to switch the electron beam on and off.[82, 97] This coaxial secondary anode is located on top of the HC-PES as shown in Figure 3-2. The anode is a thin tungsten filament that is electrically connected to the bias grid through a MOSFET. When the MOSFET is on, this connection effectively shunts the electrons in the plasma to the secondary anode. When the MOSFET is off, the secondary anode floats to the plasma potential within the cathode and electrons will again flow through the aperture to reach the bias grid.

The plasma power supply is current-limited to restrict heating of the hollow cathode. For the majority of the experiments, the current was limited at 200 mA. The electrons in the emitted beam must be replenished by the power supply. Consequently, the current limit on the plasma power supply also regulated the electron beam current to the sample. Much more current could be extracted if the hollow cathode was allowed to run at higher temperatures. However, the hollow cathode plasma would be harder to control at these higher temperatures.

The sample is connected to the chamber ground. The grounding of the sample prevents the sample from building up a potential that would then deflect incident electrons. The sample current can be quantified by installing an ammeter between the sample and ground. This sample current is a direct measure of the electron current to the sample from the HC-PES. The sample current determines the time required to desorb ligands from the surface during EE-ALD.

3.3.3 Electron Steering Optics

Figure 3-1 shows that ions are accelerated toward the wall of the hollow cathode. These ions collide with the wall at a kinetic energy of hundreds of electron volts. These collisions

produce secondary electrons that sustain the plasma. In addition, these collisions also sputter the walls of the hollow cathode, with a yield that depends on ion energy. While this sputtered material can be used for thin film deposition if the sputtered species have line-of-sight to the substrate,[92] the sputtered material will adversely affect purity of the films grown by EE-ALD in this study.

In the hollow cathode displayed in Figure 3-2, the enclosed nature of the hollow cathode cavity confines most of the sputtered material inside the hollow cathode. However, some of the sputtered material can leave the hollow cathode cavity through the aperture where the electron beam exits. In addition, the aperture can be sputtered by ions in the hollow cathode cavity, where ions hitting the edge of the aperture can lead to forward scattering of sputtered species. Sputtering of the edges of the aperture can enlarge the aperture. This enlargement will eventually affect the pressure differential across the aperture that is necessary to sustain the plasma. The pressure differential is important to maintain a lower pressure in the chamber to provide a long mean free path for the electrons to reach the sample. To minimize this sputter yield, a sputter resistant material can be chosen for the aperture. Molybdenum, tungsten and tantalum have fairly low sputtering yields.[99] For the hollow cathode in this study, molybdenum was used as the aperture material since molybdenum is relatively easy to machine.

To address the sputter deposition on the sample, electron optics were developed to steer the electron beam through a bend. The sputtered neutrals are not affected by the electron steering optics and do not pass through the bend, thereby eliminating line-of-sight from the cathode to the sample. Illustrations of the bending of electrons by magnetic fields defined by electromagnetic coils are shown in Figure 3-4.

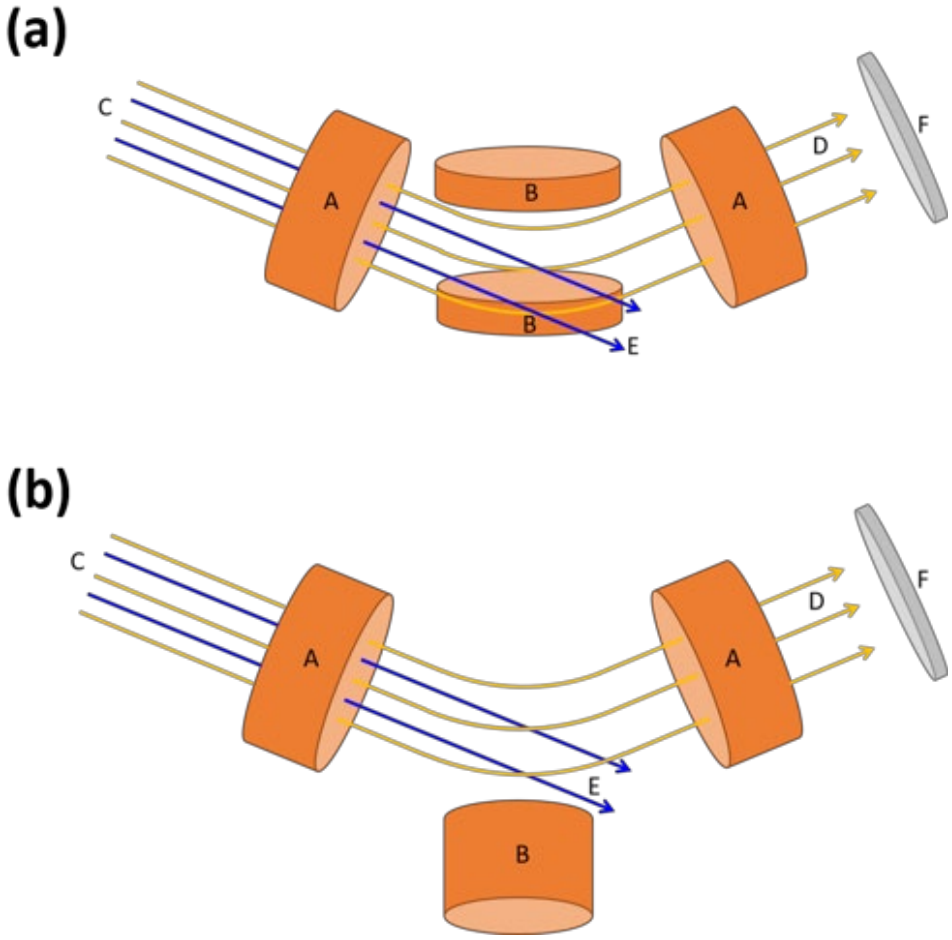

Figure 3-4. Schematic of installed electron optics with (a) two steering coils above and below bend and (b) one steering coil outside bend. Schematic designates: (A) collimating coils; (B) steering coil; (C) electron beam with sputtered material from HC-PES; (D) clean electron beam; (E) sputtered material separated from electron beam; and (F) sample.

Any sputtered ions should be attracted to the negative potential on the cathode wall or bias grid before they enter the electron steering optics. The magnetic fields used in this work were not sufficient to steer any possible ion transmission. The electron steering optics in Figure 3-4a were composed of a pair of on-axis collimating electromagnetic coils and a pair of off-axis steering electromagnetic coils above and below the bend. A photograph of these collimating and steering electromagnetic coils is given in Figure 3-5a.

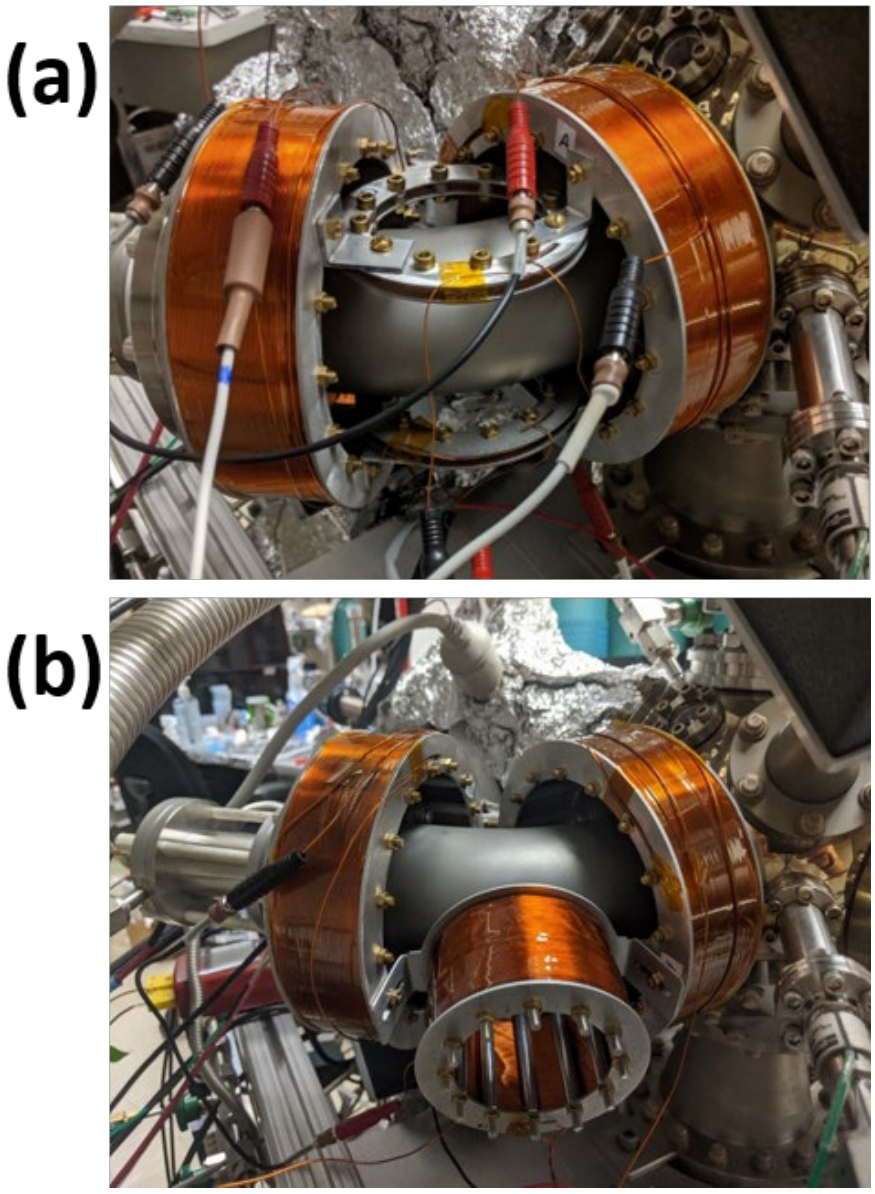

Figure 3-5. Picture of installed electron optics with (a) two steering coils above and below the bend and (b) one steering coil outside the bend. HC-PES is to the left of the leftmost collimating electromagnetic coil. The main chamber and the sample are to the right of the rightmost collimating electromagnetic coil.

The electron beam diverges because electrons repel each other as they travel due to space-charge effects. The on-axis coils collimate and center the electron beam. The magnetic field from the

collimating coils provides a track for the electrons. The electrons spiral along the field lines, packing more closely as the magnetic field strength increases in the region of the coil.

The off-axis steering coils alone should be able to bend the electron beam and sweep the beam alignment in the plane of the bend. This sweep of the beam alignment provides precise positioning of the electron beam in the horizontal plane on the sample stage. However, when combined with the large magnetic fields from the on-axis electromagnetic coils, the off-axis coils in Figure 3-4a were not able to move the electron beam enough to position the electron beam on the exact center of the sample stage.

Determining the electron beam center on the sample stage is difficult when the electron flux is sufficient to remove all ligands from the saturated surface after precursor adsorption. In this electron flux limit, the spatial distribution of the deposited film is uniform. To identify the electron beam center, electron-enhanced BN chemical vapor deposition (CVD) was employed using borazine as the sole-source precursor.[57] BN EE-CVD does not exhibit the self-limiting behavior associated with saturation. Consequently, the spatial deposition of the BN EE-CVD can reveal the electron beam center.

The updated configuration, shown in Figure 3-4b, was implemented for more precise alignment of the electron beam. This configuration has a single off-axis electromagnetic coil positioned outside the bend. This coil effectively pushes the beam around the bend and steers the electron beam. A photograph of the collimating and steering electromagnetic coils corresponding to Figure 3-4b is given in Figure 3-5b. This configuration results in more accurate positioning of the electron beam at the center of the sample stage than the configuration shown in Figure 3-4a and Figure 3-5a.

Several configurations of electromagnetic coils were used for the different experiments as described in the text. Both configurations shown in Figure 3-4 were effective at bending the electron beam and separating the electron beam from the sputter yield. Prior to installing the electron steering optics, in situ Auger Electron Spectroscopy (AES) of samples subjected to electron beam exposures showed a Mo AES signal. In contrast, no Mo AES signals were observed after the installation of the electron steering optics.

3.4 Experimental for Co EE-ALD

Co EE-ALD films were grown in a vacuum apparatus chamber that has been described previously.[30, 36, 57] The main UHV chamber with a base pressure of 2×10^{-9} Torr is equipped with a load lock that allows samples to be introduced without breaking vacuum. The main chamber also contains an in situ ellipsometer (Filmsense1) and mass spectrometer (PrismaPlus QMG 220, Pfeiffer Vacuum). In addition, a pico-ammeter (Keithley) is attached to the sample stage to measure the incident electron current. An analysis chamber containing an in situ Auger electron spectroscopy (AES) spectrometer (RBD, microCMA) is also attached to the main chamber.

The Co EE-ALD films were grown on Si wafer coupons (Silicon Valley Microelectronics, boron doped). The Si coupons contained the native oxide on the silicon surface. Prior to insertion into the vacuum apparatus, the Si coupons were washed in methanol and acetone and blown dry with ultra-high purity nitrogen. The Si coupons were then loaded into the load lock chamber following procedures that have been detailed earlier.[36]

The Co EE-ALD growth was conducted using a pulse sequence consisting of: (1) cobalt tricarbonyl nitrosyl (CTN) adsorption; (2) pump time; (3) electron beam exposure; and (4) pump

time before the next adsorption. The timing for this pulsing sequence can be characterized by (t_1, t_2, t_3, t_4). The following is representative of the parameters in a typical experiment. The CTN precursor was kept at 3 Torr behind a micropulse valve. The valve was actuated for t_1 = 0.5 s. The valve opening led to a transient pressure in the main chamber of ~5 x 10^{-3} Torr. Pumping was then performed for a total of t_2 = 20 s. The electron exposure was then performed with a grid bias of 140 V for t_3 = 2 s, with an electron current of >50 mA. The next CTN adsorption was then conducted after a pump time of t_4 = 20 s. The timing for this pulsing sequence was (0.5, 20, 2, 20). The sum of these steps produced a reaction cycle time of ≈43 seconds.

In situ ellipsometry (Filmsense, FS1) measurements were collected every second throughout the deposition. The in situ ellipsometer uses four wavelengths of light. The precision of the in situ ellipsometry measurements of film thickness is within ± 0.03 Å. Ex situ spectroscopic ellipsometry (Model M-2000, J.A. Woollam Co., Inc.) was also performed to measure the film thickness and determine the spatial profile of the deposited film. The data was fit using a B-spline model in CompleteEase (J.A. Woollam Co., Inc.) with n & k values for Co as a starting point. Focusing probes that reduce the spot size to 0.3-0.4 mm were used for data acquisition.

The technique of in situ lift-out in an FEI Nova 600 Dual Beam SEM/FIB was used for preparing cross-sectional TEM specimens. The surfaces of the specimens were polished with low energy (2 keV) Ga ion beam to minimize the damaged layer caused by focused ion beam (FIB) milling. All HAADF-STEM images and EDS maps were acquired at 300 kV on a spherical aberration corrected FEI Titan Themis equipped with a Bruker Super-X quad EDS detector.

3.5 Results and Discussion

3.5.1 HC-PES Characterization

The HC-PES can produce an electron beam with high currents. **Error! Reference source not found.**

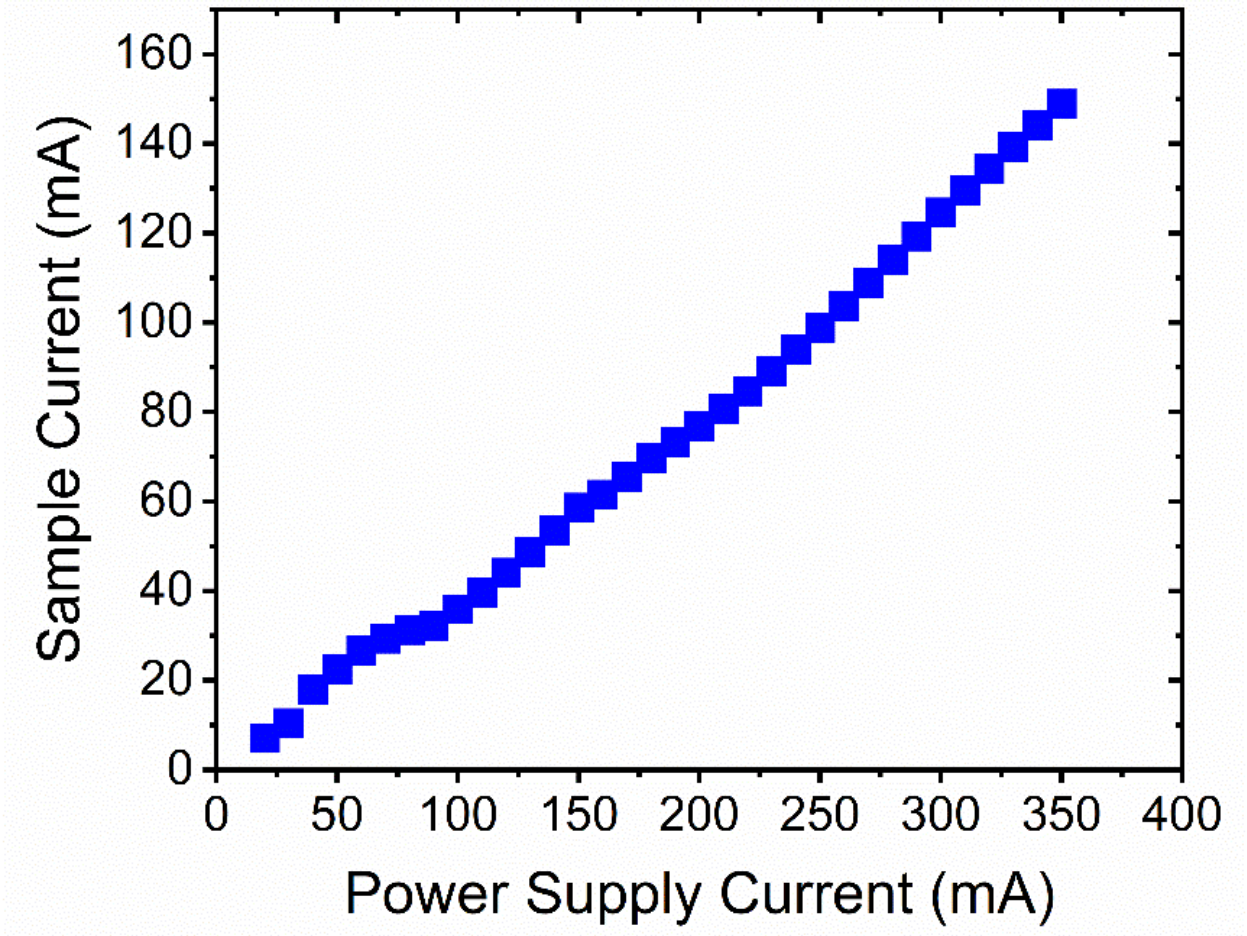

Figure 3-6. Sample current as a function of the power supply current.

shows the measured sample current versus the HC-PES power supply current. The power supply current can be turned up even higher to produce a proportionally larger sample current. However, these larger power supply currents lead to heating of the hollow cathode. This heating

must be contained because of the thermal limits of the Viton O-Rings that are used to seal the various components that define the HC-PES. Constructing a HC-PES without using temperature sensitive materials is possible. The present setup with Viton O-Rings allows easy access to the hollow cathode cavity and replacement of the aperture. Importantly, the electron currents obtained with the present HC-PES are sufficient for EE-ALD experiments to be conducted in a timely manner.

Another advantage of the HC-PES is the rapid on/off switching of the electron beam. Figure 3-7

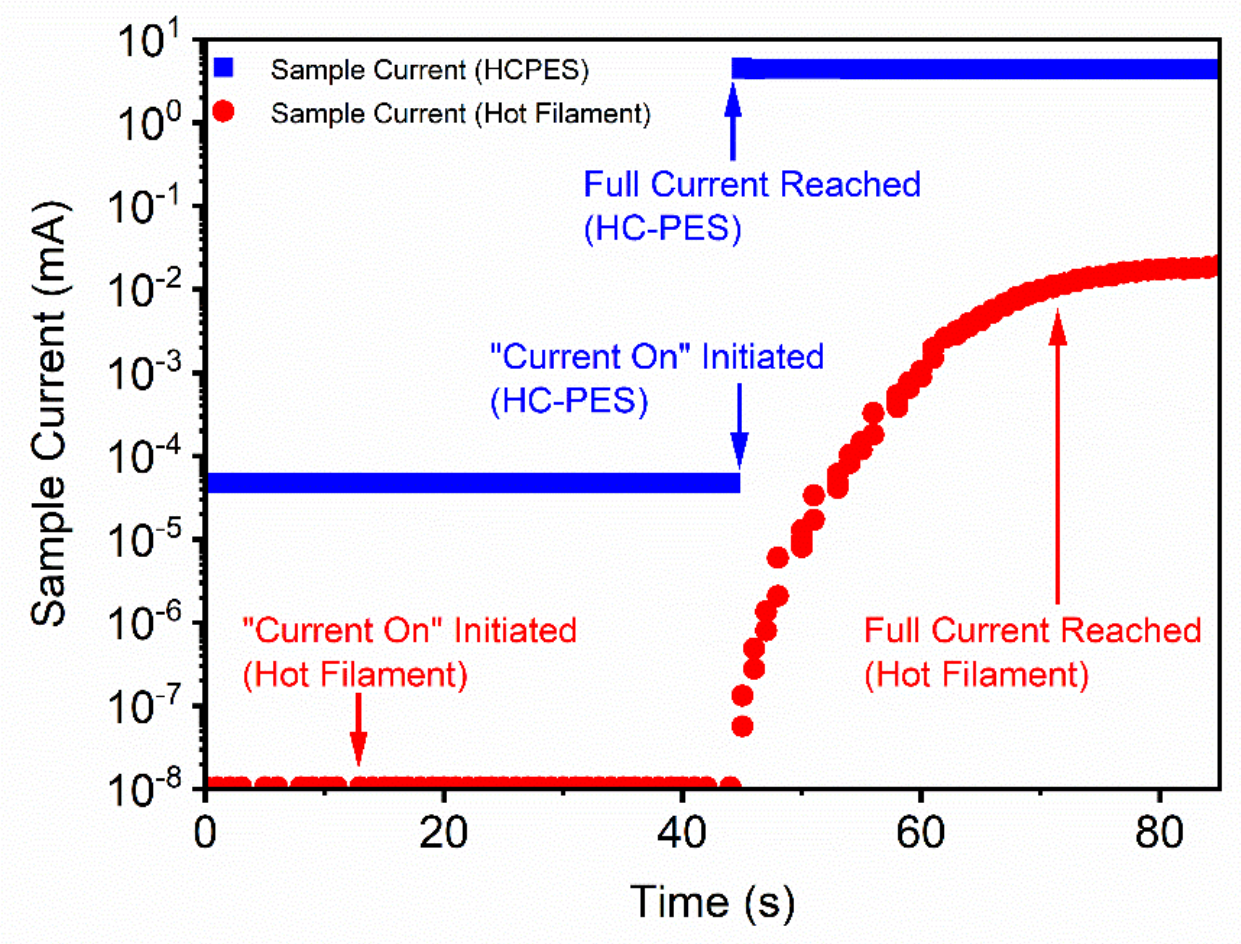

Figure 3-7. Comparison of the start-up time of the electron gun and HC-PES. Electron gun reached full current in >1 min. HS-PES reached full current in <10 ms.

shows a comparison between the HC-PES and an electron flood gun (FRA-2x1-2, Kimball-Physics Inc.) for obtaining full current to the sample. For the HC-PES, the electron beam can be effectively turned on/off by switching with a MOSFET that provides access to a secondary anode. When the MOSFET is switched on, most of the electrons flow through the secondary anode. Figure 3-7 indicates that only a small number of electrons can travel through the aperture and reach the sample when the MOSFET is turned on. This "leakage" current from the HC-PES is almost three orders of magnitude less than the full electron current from the electron gun. These low electron currents have a negligible effect on Co EE-ALD.

Upon turning off the MOSFET, the electron beam can exit the aperture at the front of the HC-PES and reach the sample. Figure 3-7 reveals that the electron beam is reestablished in less than the 10 ms time resolution of the ammeter used to make the measurement.[100] In contrast, Figure 3-7 shows that the electron gun used in previous work requires several minutes to obtain an electron beam from the hot filament.

Figure 3-7 also illustrates the dramatic difference in electron current from the HC-PES and the electron flood gun. Electron currents from the HC-PES described in this publication easily reach 100 mA over a 10 cm^2 area in steady state operation. This is a factor of 3000x more current over an area 10x larger than for the previous electron flood gun. The factor of 3000x more current over an area 10x larger is an increase of 300x in electron flux. The essentially immediate on/off switching and the 300x increase in electron flux lead to a dramatic reduction in cycle time for EE-ALD.

The chemical insensitivity of the HC-PES is also important in reducing the EE-ALD cycle time. The hot filament in the electron flood gun must not be hot when precursor is present in the reactor to avoid precursor decomposition on the filament that leads to chemical vapor

deposition (CVD). This CVD can lead to corrosion of the filament or change its work function. These changes can decrease both filament lifetime and the electron emission from the hot filament. To avoid this CVD, the precursor must be completely removed from the chamber prior to and after heating the filament.

Previous EE-ALD experiments using electron flood guns have reported that the time required for filament warm up, cool down, pumping, and electron exposure with low electron flux can be as long as 15 minutes for just the electron exposure step.[30, 101-103] In contrast, an EE-ALD cycle using the HC-PES is essentially as long as the electron exposure. Electron exposures are usually on the order of 10 s. Large pump or purge times are not necessary because the HC-PES is chemically insensitive.

3.5.2 Co EE-ALD Growth Characteristics

Co EE-ALD can be performed using sequential exposures of cobalt tricarbonyl nitrosyl (CTN) and electrons.[101] The surface reactions during one cycle of Co EE-ALD using CTN and electron exposure are given below:

(A) $Co^* + Co(CO)_3NO(g) \rightarrow Co\text{-}Co(CO)_3NO^*$ (Eq. 3.1)

(B) $Co\text{-}Co(CO)_3NO^* + e^- \rightarrow Co\text{-}Co^* + 3CO(g) + NO(g)$ (Eq. 3.2)

The asterisks indicate the surface species. Co EE-ALD films are grown by repeating the Co EE-ALD cycles. The desorption of CO and NO during electron exposures has been confirmed earlier using quadrupole mass spectrometry investigations.[101] The cobalt thickness versus spatial position after a number of Co EE-ALD cycles reveals the electron beam on the sample.

A comparison of spatial profiles for Co EE-ALD are shown in Figure 3-8.

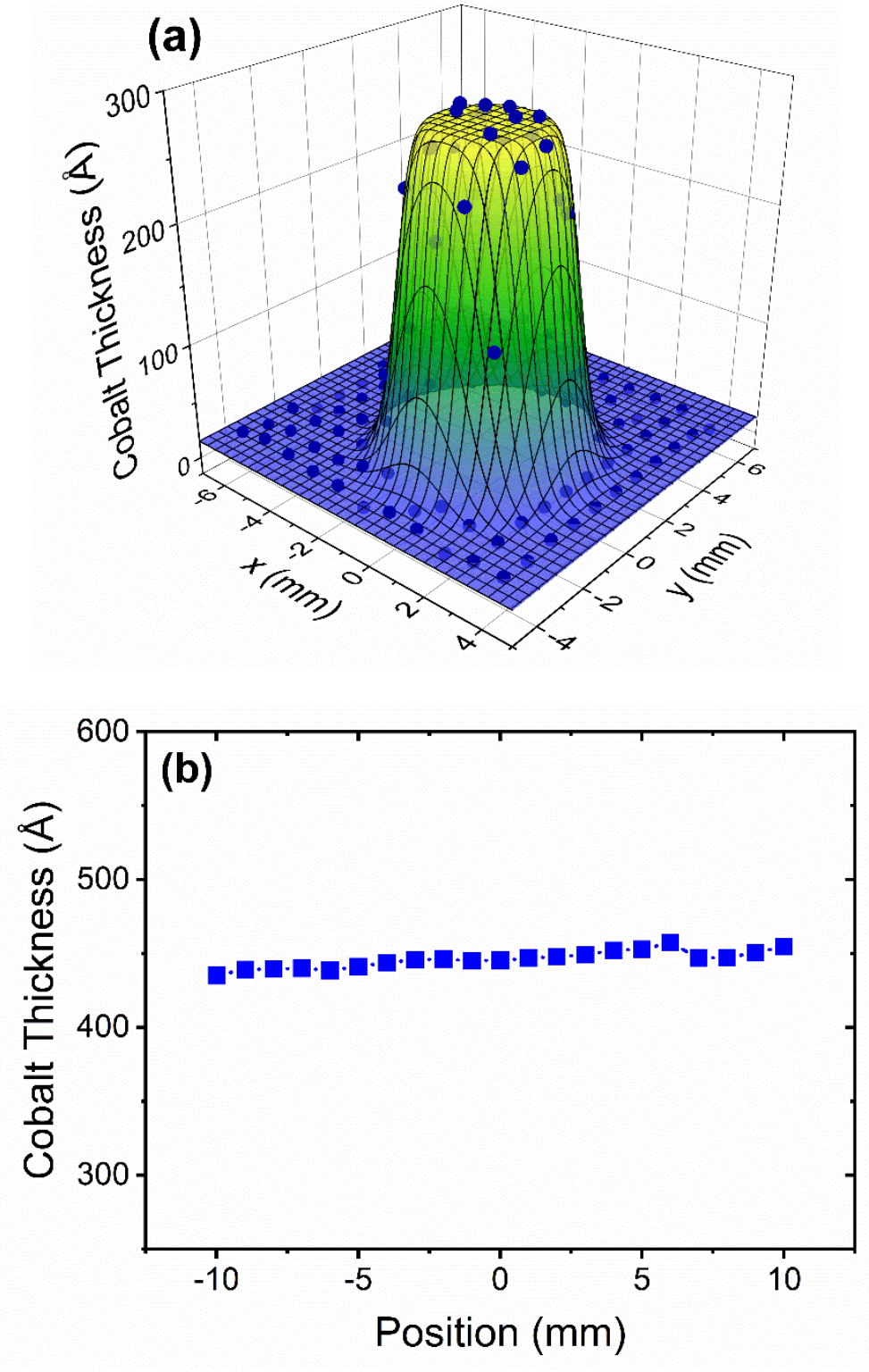

Figure 3-8. Comparison of (a) three-dimensional spatial profile of the Co EE-ALD film grown using the electron flood gun and (b) two-dimensional spatial profile of the Co EE-ALD film grown using the HC-PES.

Figure 3-8a displays the spatial profile of the focused electron beam from the hot filament electron gun.[1] The electron gun has a small spot size of approximately 1 cm^2. The electron flux achieves saturation of the electron stimulated desorption reaction as revealed by the "flat top" profile over a small, ≈0.25 cm^2 area of the substrate. Additional calculations confirmed that the "flat top" profile was a signature of saturation behavior.[101]

The electron exposure time required to achieve saturation at the center of the electron beam spatial profile for the cobalt deposition shown in Figure 3-8a during Co EE-ALD was 16 minutes with the electron gun.[101] A Co film thickness of ≈289 Å was measured after 198 EE-ALD cycles with an electron energy of 200 eV.[101] The dependence of the Co EE-ALD growth rate on electron energy was examined using electrons from the electron gun.[101] The growth rate was highest at a lower electron energy of 125 eV. For the results in Figure 3-8a, the incident electron current on the sample was 21 μA. The time for one EE-ALD cycle was 21 min. The total processing time was 69.3 hours.

In contrast, Figure 3-8b shows the spatial profile for cobalt deposition after Co EE-ALD using the HC-PES. The constant Co thickness of ≈435 Å indicates that the electron exposures can provide saturation exposures over these surface areas of at least 4 cm^2. There is no "flat top" profile because the film thickness is uniform over the entire substrate. The HC-PES can deposit a more uniform Co film thickness over a larger surface area in much less time than the electron gun. These results were obtained after 156 Co EE-ALD cycles using a grid bias of 140 V at an electron current of 10 mA. Given the time for one EE-ALD cycle of 110 s, the total processing time was 4.8 hours. Compared with the electron gun, this performance with the HC-PES represents an order of magnitude increase in area in an order of magnitude less time to produce Co films of comparable thickness.

The spatial profile after cobalt deposition shown in Figure 3-8b was performed prior to installing the electron steering optics displayed in Figure 3-5. For this cobalt deposition, the HC-PES had line-of sight to the sample, with the electron flux directed along the surface normal. A single electromagnetic coil was also used to collimate the electron beam. The time for one EE-ALD cycle was 110 s. During this EE-ALD cycle, 80 seconds were dedicated to the electron exposure. The single collimating coil focused fewer electrons onto the sample. This necessitated the longer electron exposure time of 80 seconds. In situ AES measurements determined that the Mo composition in the Co EE-ALD film was 11 at%. After the installation of the electron optics Mo contamination was eliminated. Other impurities which remained in the Co EE-ALD film were C, O and N at 6.0, 22.6 and 6.2 at%, respectively.

Figure 3-9

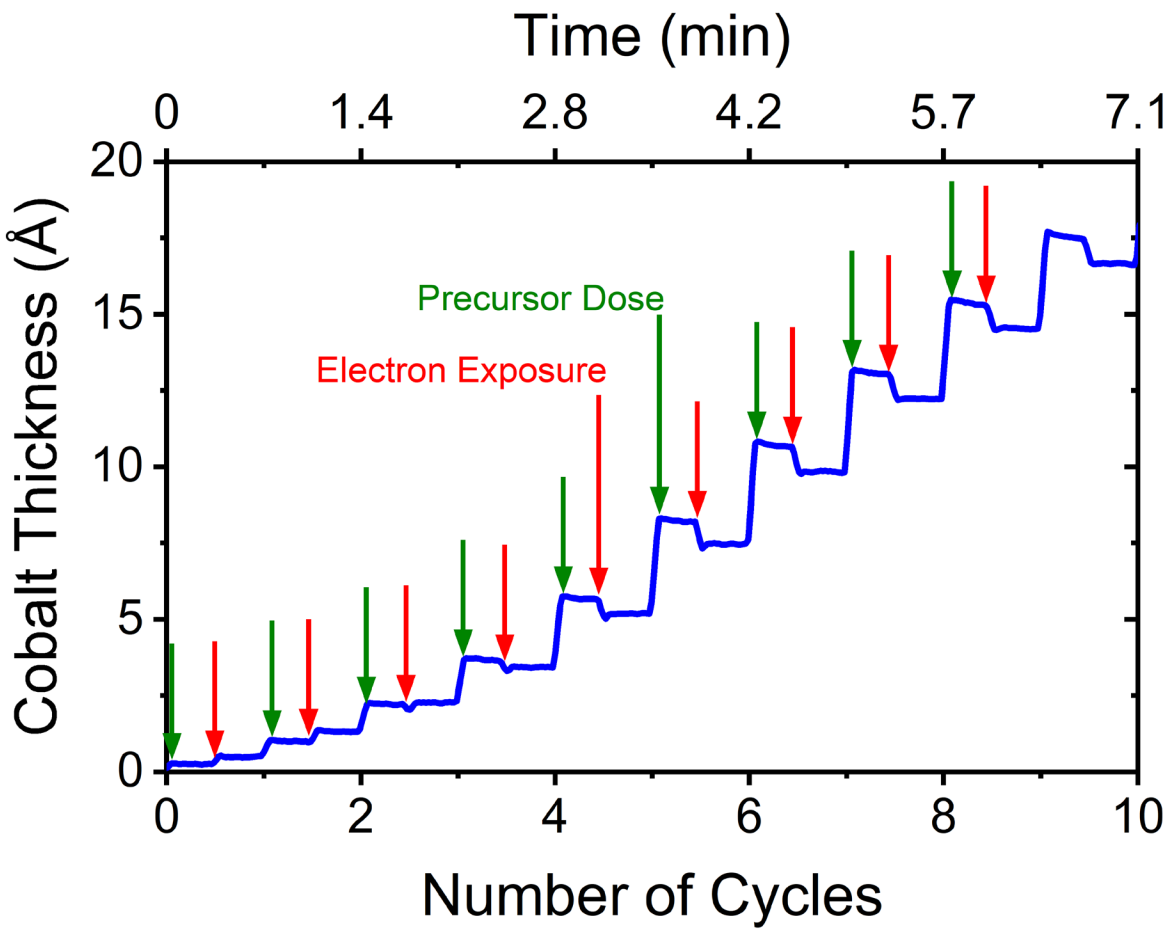

Figure 3-9. In situ real time ellipsometry of Co EE-ALD nucleation on native oxide on Si coupon. The growth rate at a steady state was 2.4 Å/cycle

shows the initial nucleation of Co EE-ALD on the native oxide of the Si coupon using the steering optics shown in Figure 3-5a. The electron current was 72 mA for 1.5 seconds with a grid bias of 140 V. The pumping time was 20 seconds before and after each electron exposure. The total cycle time was 43 s. The in situ ellipsometry measurements observe deposition from the first electron exposure. The thickness increases with each precursor dose. The measured thickness is then constant until the electron exposure. The electron exposure leads to a reduction

of the measured thickness. The Co EE-ALD film nucleates in 4 EE-ALD cycles. The cobalt film growth is then very constant at 2.4 Å/cycle for subsequent EE-ALD cycles.

To appreciate the significance of these results, Figure 3-10

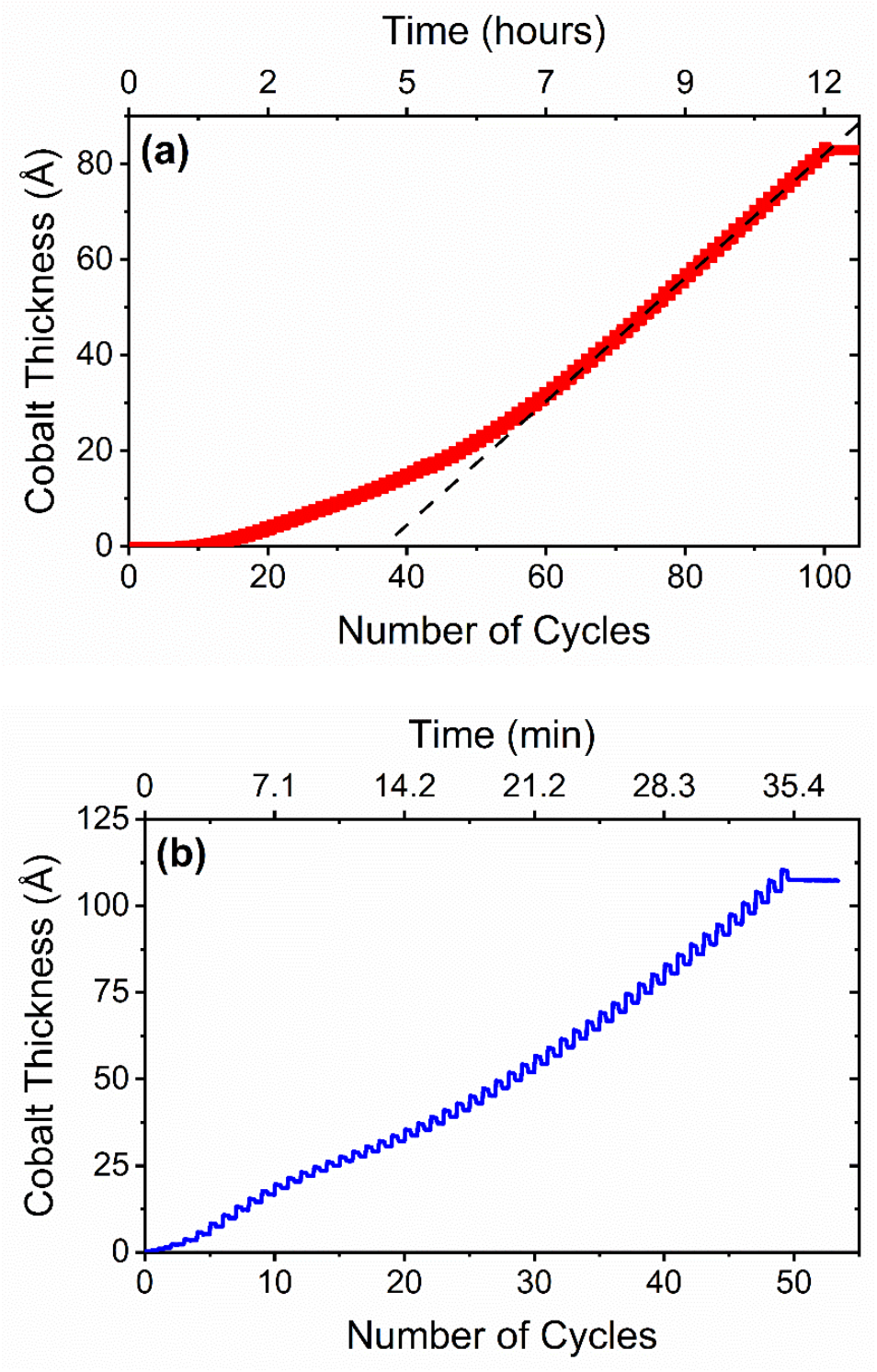

Figure 3-10. Nucleation of Co EE-ALD using (a) electron flood gun and (b) HC-PES. Co EE-ALD with the electron flood gun had an EE-ALD cycle time of 7 min and a steady- state growth rate of 1.3 Å per cycle after nucleation. Co EE-ALD with HC-PES had an EE-ALD cycle time of 43 s and a steady-state growth rate of 2.4 Å per cycle after nucleation.

compares the nucleation of Co EE-ALD using the electron gun and the HC-PES. The HC-PES obtains much more rapid nucleation of Co EE-ALD than the electron flood gun. In Figure 3-10a, there is a delay of approximately 10 cycles before observing any deposition.[1] Between 10-50 cycles, the deposition occurs and increases progressively with the number of cycles. The EE-ALD reaches steady state growth after approximately 50 cycles.

These results were obtained with an electron energy of 100 eV and an electron current of 21 μA with the electrons focused to a Gaussian spatial profile with a waist of ≈2.5 mm.[101] The EE-ALD cycle time was 7 min.

Extended nucleation times similar to the long nucleation period observed in Figure 3-10a are typical for metal ALD on metal oxides.[104-106] For EE-ALD, one possible explanation for the long nucleation period is that the low electron fluxes from the electron gun were not adequate to create sufficient active sites on the substrate. Consequently, many EE-ALD cycles were required for enough nucleation sites to build up on the surface and eventually lead to linear growth.

In contrast, nucleation is much more rapid during Co EE-ALD using the HC-PES. Figure 3-10b shows the rapid nucleation of Co EE-ALD. These results are an extension of the results described above and depicted in Figure 3-9. Cobalt deposition is observed during the first EE-ALD cycle. The Co deposition increases progressively between the 2nd and 6th EE-ALD cycles. Subsequently, the Co EE-ALD film proceeds to grow linearly with a growth rate of 2.4 Å/cycle. These results were obtained with a grid bias of 140 V and an electron current of 72 mA for an electron exposure time of 1.5 s with the electrons illuminating an area of at least 2 x 2 cm^2. The EE-ALD cycle time was 43 s.

Co EE-ALD film growth with the HC-PES was observed to be linear over a wide range of electron exposures. The large electron flux of the HC-PES allows electron exposures to be short and still achieve growth rates > 1 Å per EE-ALD cycle. Figure 3-11

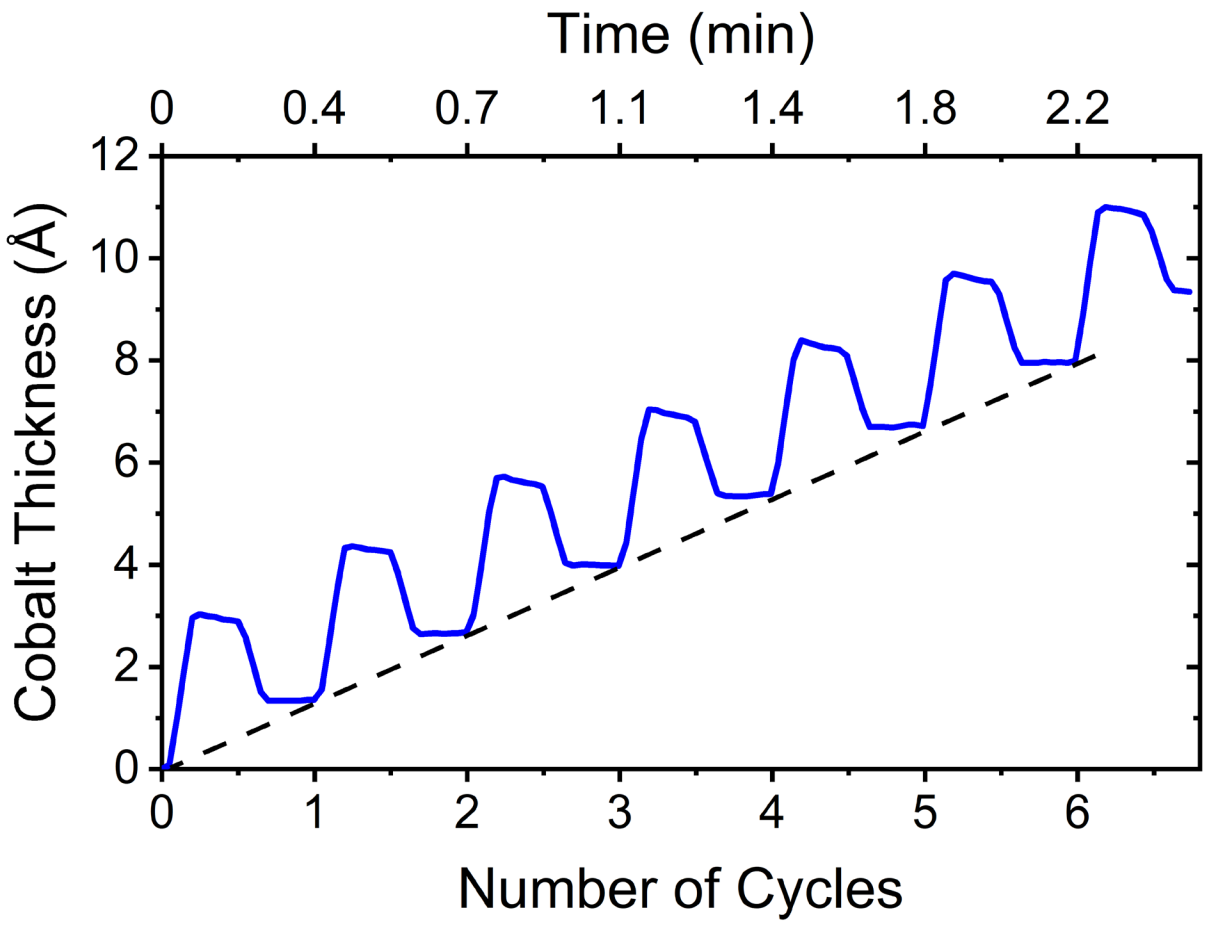

Figure 3-11. In situ real time ellipsometry of Co EE-ALD on a previously deposited Co film. The Co film growth shows linearity with EE-ALD cycle time of 22 s using short electron exposures of 1.0 s. The growth rate is 1.3 Å/cycle.

shows results for the cobalt thickness versus number of cycles for shorter electron exposure times of 1 s. The growth rate is 1.3 Å per EE-ALD cycle with the electron exposure time of 1 s. These results were obtained with a grid bias of 140 V and an electron current of 65 mA with the

electrons illuminating an area of at least 4 cm^2 using the electron steering optics shown in Figure 3-5a. The EE-ALD cycle time was 22 s with pumping times of 10 s before and after each electron exposure.

The interpretation of these results in Figure 3-11 is that the shorter electron exposure times of 1 s at 65 mA from the HC-PES desorb fewer ligands from the surface than the longer electron exposure times of 1.5 s at 72 mA. The ligands left behind after the smaller electron exposure lead to lower precursor adsorption during the next EE-ALD cycle. The lower precursor adsorption leads to the lower observed growth rates. The linearity of the EE-ALD growth can be attributed to the consistency of the electron exposure during each EE-ALD cycle. As long as the electron desorption is repeatable, linear EE-ALD growth is possible with smaller electron exposures.

One advantage of EE-ALD is the ability to deliver a directed flux of electrons to the surface. To explore the effect of this directed flux, the HC-PES was used for Co EE-ALD on patterned substrates. The pattern consisted of vias with vertical walls, oriented parallel to the surface normal. The vias were approximately 200 nm wide and approximately 1000 nm deep. The Co EE-ALD was performed prior to installing the electron steering optics. The HC-PES was line-of-sight to the sample with the electron flux along the surface normal. A single electromagnetic coil was used to collimate the electron beam.

The Co EE-ALD on patterned substrates was performed with an expected growth rate of 2.4 Å/cycle. The Co EE-ALD was conducted with a grid bias of 140 V and an electron exposure of 10 mA for 80 s. Based on various in situ AES studies, the Mo composition in the Co EE-ALD film could have been as much as 15 at%. This Mo inclusion coupled with ex situ air oxidation may account for the large deposition thickness as measured by TEM.

Figure 3-12

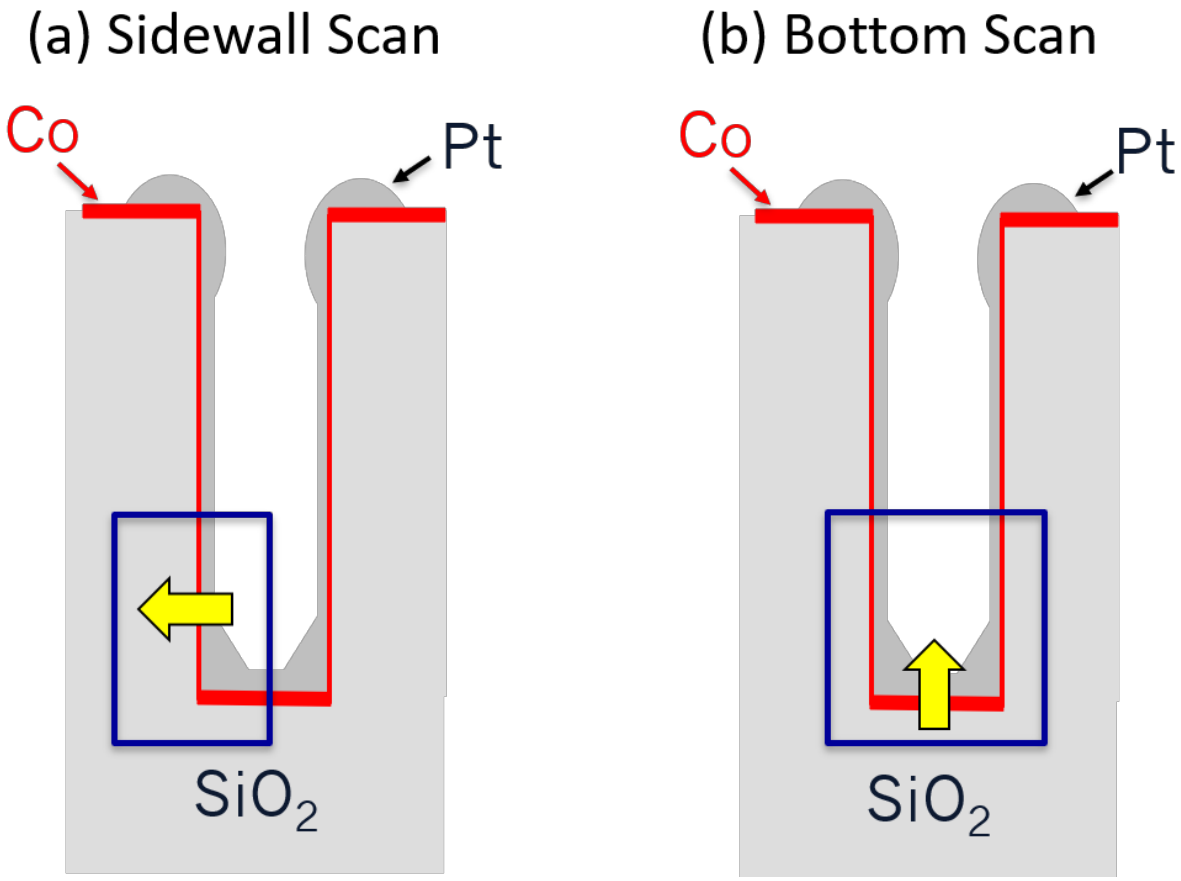

Figure 3-12. Schematic showing via locations for (a) sidewall scan and (b) bottom scan.

shows a representation of the transmission electron microscopy (TEM) and energy dispersion (EDS) scans on the sidewall and bottom of the via after Co EE-ALD on the patterned substrates. The actual TEM and EDS line scans for the sidewall and bottom of the via are displayed in Figure 3-13

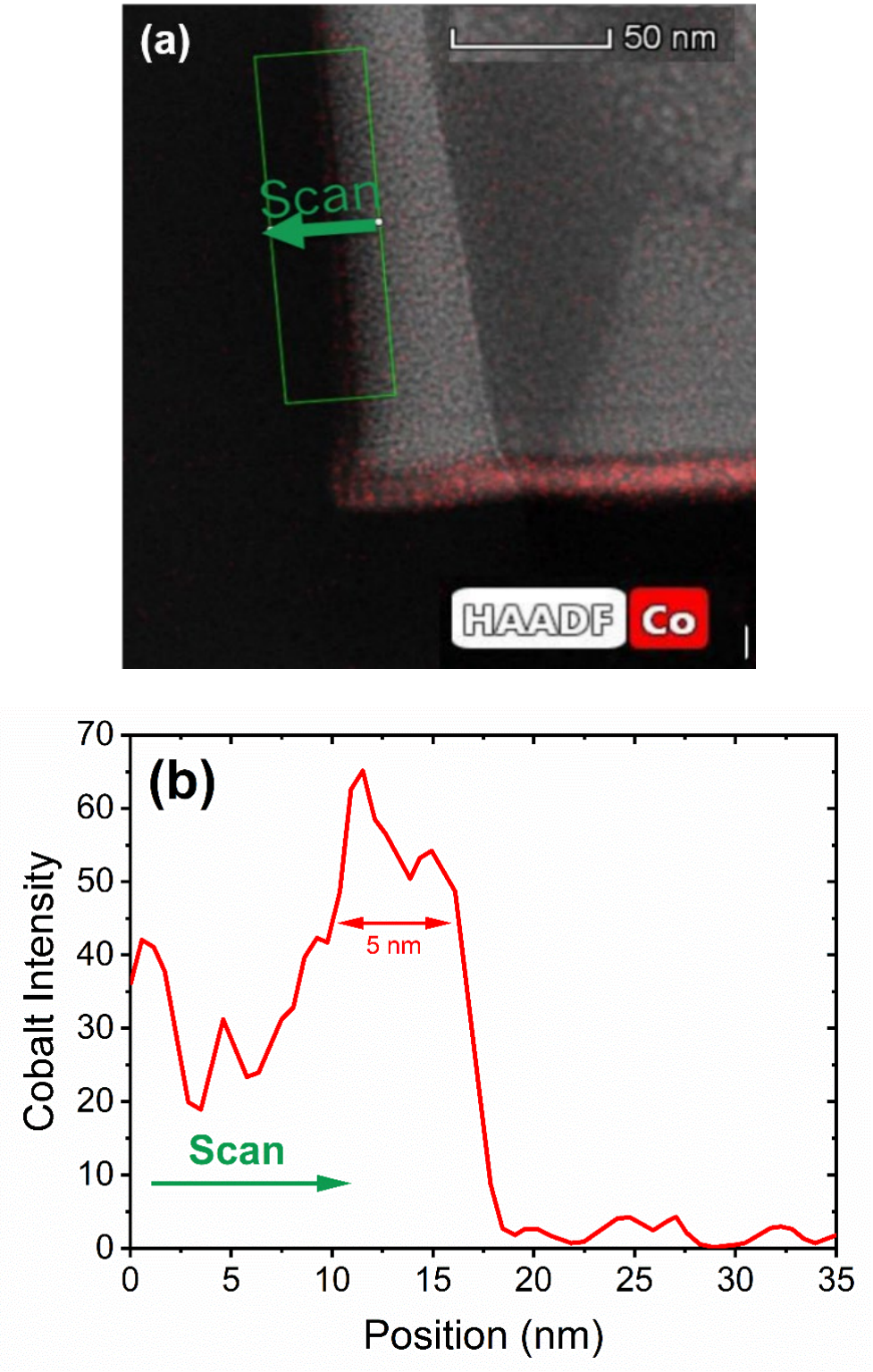

Figure 3-13. (a) TEM image of via showing the location of the sidewall scan and (b) the EDS line scan for Co on the vertical sidewall yielding a Co film thickness of ≈5 nm.

and Figure 3-14,

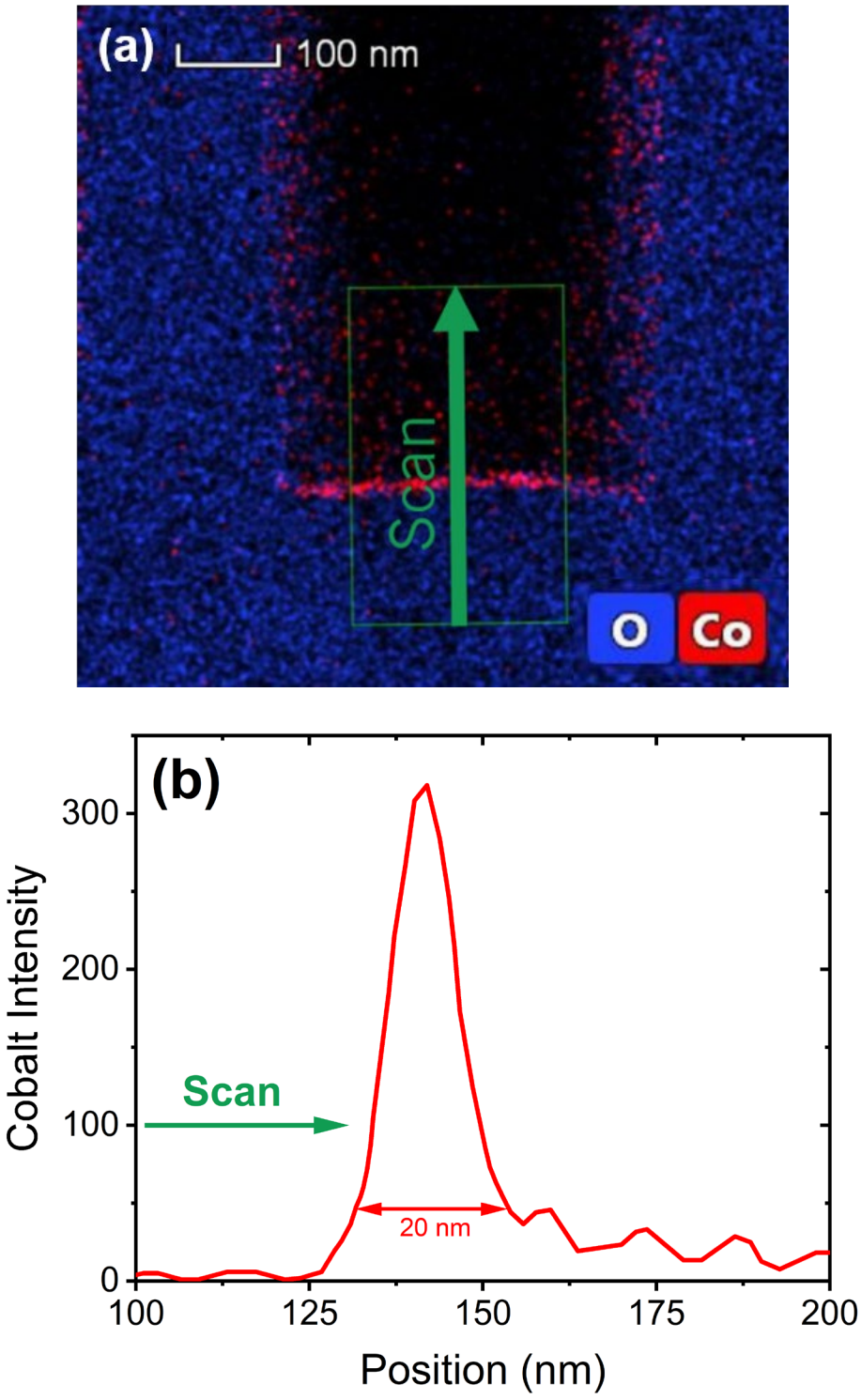

Figure 3-14. (a) TEM image of via showing the location of the bottom scan and (b) the EDS line scan for Co on the horizontal bottom yielding a Co film thickness of ≈20 nm.

respectively. The boxes in Figure 3-12 identify the areas of the via that are scanned in Figure 3-13 and Figure 3-14.

The topographical area selectivity of the Co EE-ALD is apparent from an examination of the Co line scans in Figure 3-13 and Figure 3-14. The EDS line scan on the sidewall of the via in Figure 3-13b reveals that the Co EE-ALD has a thickness of approximately 5 nm. This thickness is probably larger than the actual thickness because the vias have a curved surface. Scans across this curved surface detect signal from surface area that is not in the same plane as the focused ion beam cut required for imaging.

In comparison, the EDS line scan on the bottom of the via in Figure 3-14b reveals that the Co EE-ALD has a thickness of approximately 20 nm. In this case, the width of the Co thickness is more precise because there is no Co EE-ALD beyond the bottom of the via. A comparison of the ≈5 nm thickness on the sidewall of the via and the ≈20 nm thickness on the bottom of the via yields a topographical selectivity of 4:1.

This topographical area selectivity of 4:1 in favor of horizontal surfaces is expected given the direction of the electron flux. More of the electron flux oriented along the surface normal is incident on horizontal surfaces. The vertical sidewalls are parallel to the electron flux. Electron stimulated desorption from the vertical sidewalls will occur resulting from electron beam misalignment, electron deflection due to charging, or electron scattering in the vias. This topographical area selectivity may allow Co EE-ALD to achieve bottom-up fill of trenches and vias.

3.6 Conclusions

A hollow cathode plasma electron source (HC-PES) was built and utilized for electron-enhanced atomic layer deposition (EE-ALD). The HC-PES produced high electron currents

>200 mA that could be turned on/off in < 10 ms. These higher electron fluxes and much smaller purge times were facilitated by the chemical robustness of the HC-PES and led to short EE-ALE cycle times. This performance was greatly improved compared with the electron currents and cycle times from a previous electron flood gun source. The total process times using the HC-PES decreased by as much as an order of magnitude or more compared with the electron gun source. The sputter yield from the HC-PES was eliminated using electron steering optics defined by electromagnetic coils.

The higher electron flux from the HC-PES led to very uniform Co thin films using sequential exposures of cobalt tricarbonyl nitrosyl ($Co(CO)_3NO$) and low energy (100-200 eV) electrons. The Co films were uniform over the entire surface area of ≈4 cm^2 suggesting that the electron exposures were sufficient for the electron stimulated desorption of surface species to reach saturation. The high electron fluxes also led to the rapid nucleation of Co EE-ALD films on the native oxide on Si coupons. The Co EE-ALD films nucleated in as few as 4 EE-ALD cycles. Steady-state Co growth rates of > 2 Å/cycle were observed over the entire surface area. Shorter electron exposures also led to linear film growth at slightly lower growth rates.

Transmission electron microscopy (TEM) and energy dispersive spectroscopy (EDS) was used to analyze Co EE-ALD on high aspect ratio features. Co EE-ALD on vertical vias with a width of ≈200 nm and a depth of ≈1000 nm displayed a topographical area selectivity. There was a 4:1 topographical selectivity in favor of horizontal surfaces. This topographical selectivity was explained by the directional electron flux incident on the surface normal and parallel to the vertical sidewalls of the vias. This topographical area selective deposition may be useful for the bottom-up fill of trenches and vias.

4 Electron-Enhanced Atomic Layer Deposition of Titanium Nitride Films Using an Ammonia Reactive Background Gas

Zachary C. Sobell and Steven M. George

Department of Chemistry, University of Colorado, Boulder, Colorado 80309-0215

4.1 Abstract

Electron-enhanced atomic layer deposition (EE-ALD) of titanium nitride (TiN) films was achieved using sequential exposures of tetrakis(dimethylamido)titanium (TDMAT) and low energy electrons in the presence of a continuous NH_3 reactive background gas (RBG). This is a new ALD technique. The TiN EE-ALD was performed utilizing a hollow cathode plasma electron source (HC-PES). The HC-PES can deliver a high electron flux into background gases at pressures up to several mTorr. The TiN EE-ALD was conducted at temperatures of 30-70 °C using an electron acceleration voltage of 100 V and a NH_3 pressure of ~1 mTorr. The incident electron flux promotes electron stimulated desorption (ESD) and facilitates rapid nucleation and low temperature film growth. This TiN film growth was achieved on a variety of substrates including a native oxide on silicon, an SiO_2 thermal oxide and in situ silicon nitride films grown using electron-enhanced chemical vapor deposition (EE-CVD). Growth rates of 0.75 to 1.8 Å per cycle were measured using in situ 4-wavelength ellipsometry for different TDMAT precursor exposures. Ex situ x-ray photoelectron spectroscopy (XPS) studies indicated that the TiN films were high purity and slightly nitrogen-rich. The in situ ellipsometry also measured low resistivities of ~120 μΩ-cm for the TiN films with thicknesses of ≥ 60 Å. These low resistivities were confirmed by ex situ four-point probe measurements and ex situ spectroscopic ellipsometry. X-ray diffraction investigations determined that the TiN films were crystalline. X-ray reflectivity studies also indicated that the thin TiN films had densities similar to bulk films.

The high quality of the TiN EE-ALD films is attributed to the NH_3 RBG. Interaction between the low energy electrons and the NH_3 RBG is believed to form $\bullet NH_2$ and •H radical species that react with the surface during EE-ALD and improve film purity. The reactive $\bullet NH_2$ and •H species likely lead to nitridation and carbon removal from the films. RBGs greatly expand the possibilities for tuning film composition and properties during EE-ALD. In addition, TiN EE-ALD was accomplished on insulating substrates such as an SiO_2 thermal oxide. The TiN EE-ALD is believed to be possible on insulating substrates because the secondary electron yield for electron energies of ~100 eV is greater than unity.

4.2 Introduction

Low energy electrons can deposit films of semiconductors, metals, and dielectrics by electron-enhanced atomic layer deposition (EE-ALD). EE-ALD has been previously used to deposit GaN, Si, BN and Co films in a high vacuum environment.[35, 56, 107-109] EE-ALD employs sequential exposures of precursors and low energy electrons at ≤ 100-150 eV to deposit these thin films. During EE-ALD, the precursor molecule adsorbs on the substrate. Subsequent electron exposure leads to a loss of ligands from the adsorbed precursor through electron stimulated desorption (ESD). The desorbed ligands leave behind open sites that are then available for further precursor adsorption. Repeating the sequential precursor doses and electron exposures yields EE-ALD growth.

The deposition of Si from disilane (Si_2H_6) can be considered a model system for EE-ALD.[56] Silicon was deposited using sequential surface reactions with Si_2H_6 and low energy electrons as the reactants.[56] The proposed mechanism was dissociative adsorption of Si_2H_6 on the surface and then the removal of hydrogen by ESD using low energy electrons. The removal of hydrogen from the surface leaves behind dangling bonds on the silicon. These dangling bonds

are then available for subsequent Si_2H_6 adsorption. Silicon growth rates were determined to be 0.3 Å/cycle at room temperature and an electron energy of 100 eV. Calculations showed that this growth rate agrees well with the predicted growth rate based on dissociatively adsorbed Si_2H_6 on the dangling bonds of a Si surface.[56]

EE-ALD is a non-thermal process and can deposit materials at low temperatures <100 °C. The directional electron flux also leads to topographically selective deposition.[35] Surfaces that are normal to the electron flux receive a larger electron exposure than surfaces parallel to the electron flux. This difference yields deposition primarily on surfaces normal to the direction of electron travel. In addition, large electron exposures lead to saturation of the ESD process by desorbing all the surface species. This desorption in the saturation limit produces a very conformal coverage of the deposited film. EE-ALD also has been shown to nucleate rapidly on a variety of surfaces.[35, 56, 107-109] Rapid nucleation should produce continuous films that may be important for ultrathin diffusion barriers and liners.

Titanium nitride (TiN) films have many applications. For example, TiN acts as a barrier to Cu diffusion.[110-112] Without a diffusion barrier, Cu readily diffuses into Si and SiO_2.[113-114] Ultrathin TiN diffusion barriers in small vias and trenches are important to maximize the amount of space that can be occupied by the Cu conducting line.[115-116] Rapid nucleation of TiN is critical to produce ultrathin continuous TiN films. In contrast, long nucleation times lead to thicker and rougher films prior to obtaining continuous films. TiN films also act as effective barriers to protect Ti and Si from chemical attack by WF_6 during W plug formation.[117] In addition, thin TiN films are used in the metal gate stack for CMOS.[118]

Previous TiN ALD films have required high deposition temperatures or have suffered from high porosity, low purity, and high resistivity.[110, 119-125] Plasma enhanced TiN deposition

processes can result in more desirable film properties, but risk substrate damage from the high energy ions.[126-127] TiN deposition processes with $TiCl_4$ and NH_3 have additional drawbacks including the generation of corrosive HCl. Thermal ALD with tetrakis(dimethylamido)titanium (TDMAT) and NH_3 has been shown to have high porosity and large C impurities.[120] The high porosity allows for facile oxidation.

In this investigation, TiN EE-ALD was performed using sequential exposures of TDMAT and low energy electrons in the presence of a continuous NH_3 reactive background gas (RBG) at a pressure of ~1 mTorr. An illustration of this processing sequence is shown in Figure 4-1.

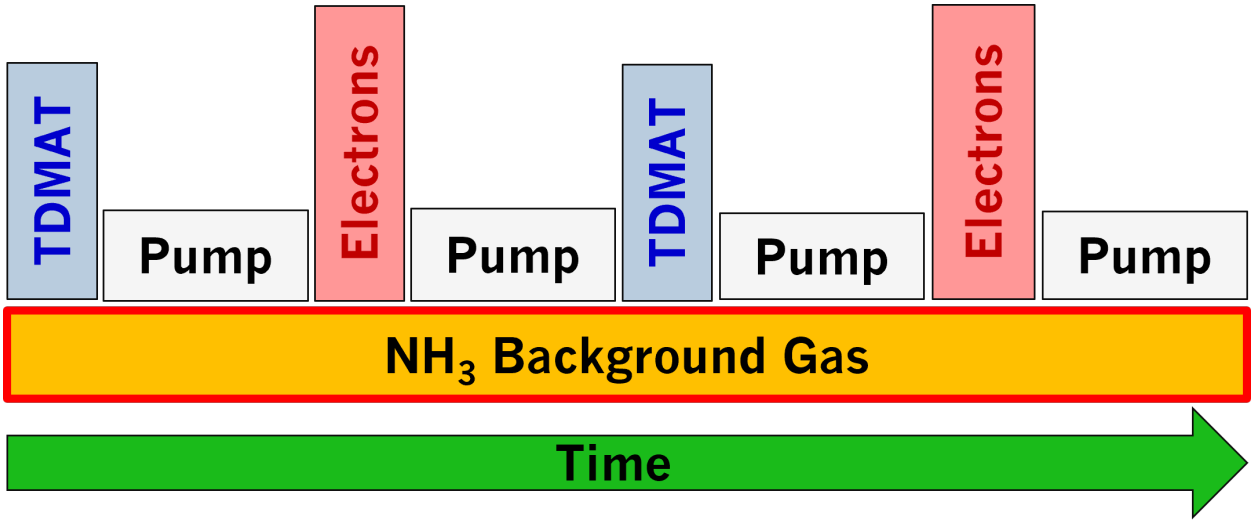

Figure 4-1. TiN EE-ALD process using sequential TDMAT and electron exposures with continuous NH_3 reactive background gas.

The electrons can induce ESD of surface species to create reactive surface sites. The electrons can also dissociate NH_3 in the gas phase. The dissociation products of NH_3 help nitridate and purify the TiN film. A similar strategy has been employed in the field of focused electron beam induced deposition (FEBID). High electron energies of ~1 keV during FEBID lead to nearly

complete dissociation of the gas precursors and high impurity levels in the FEBID films. Some FEBID studies have reported using a background gas during FEBID to attempt to reduce the impurity concentrations.[19, 31-33] The use of an RBG in this study illustrates how an RBG also improves film purity during EE-ALD.

4.3 Experimental

The TiN EE-ALD films were grown in a vacuum chamber that has been described previously.[35, 56, 107-109] The main UHV chamber had a base pressure of 2 x 10^{-9} Torr. This chamber was equipped with a load lock that allowed samples to be introduced without breaking vacuum. The main chamber also contained an in situ ellipsometer (Filmsense1) and mass spectrometer (PrismaPlus QMG 220, Pfeiffer Vacuum). The chamber was also equipped with a cold cathode gauge (MKS) to measure pressure. In addition, a pico-ammeter (Keithley) was attached to the sample stage to measure the incident electron current from the electron source.

The electron source was a hollow cathode plasma electron source (HC-PES) that has been described in detail earlier.[35] An argon (Airgas, 99.999%) plasma was sparked in the hollow cathode body. Low energy electrons were extracted with a biased grid. The electrons exited the HC through an aperture. Argon gas also leaked through this aperture and produced a pressure of ~1 mTorr in the reactor. All the work in this study used an applied voltage of 100 V to the biased grid. This applied voltage accelerated the electrons leaving the aperture. The electrons were separated from any sputtered material from the hollow cathode plasma using electron optics.[35] An analysis chamber containing an in vacuo Auger electron spectroscopy (AES) spectrometer (RBD, microCMA) was also attached to the main chamber.

NH_3 (Matheson, 99.9992%) flowed into the chamber though a leak valve and was present continuously during the TiN EE-ALD. The NH_3 RBG pressure was ~1 mTorr as measured by the cold cathode pressure gauge (MKS). The recommended total cross section for electron scattering in NH_3 is $\sigma = 8.57 \times 10^{-16}$ cm^2 for electron energies of 100 eV.[128] In addition, the background Ar pressure in the chamber resulting from leakage through the aperture on the hollow cathode was ~1 mTorr. The total cross section is $\sigma \sim 8 \times 10^{-16}$ cm^2 for electron scattering in Ar for electron energies of 100 eV.[129]

The mean free path for electrons traveling through gas is $\lambda_e = 1/\rho\sigma$ where ρ is the gas number density and σ is the cross section for electron scattering by the gas. The gas number density is $\sigma = 3.2 \times 10^{13}$ molecules/cm^3 at room temperature at a pressure of 1 mTorr. Therefore, the electron mean free path is $\lambda_e = 18$ cm using $\sigma \sim 8 \times 10^{-16}$ cm^2 for the Ar and NH_3 total cross sections. Electron scattering by the Ar and NH_3 RBG does not seriously affect the electron transport over the 25 cm distance between the HC-PES and the sample.

The TiN EE-ALD was explored on several substrates including Si wafer coupons, SiO_2 thermal oxide wafer coupons, and in situ deposited silicon nitride on Si wafer coupons. The Si wafer coupons (Silicon Valley Microelectronics, boron-doped) contained a native oxide on the silicon surface. The SiO_2 thermal oxide wafer coupons had a thickness of 400 nm on a Si wafer. Prior to insertion into the vacuum apparatus, the coupons were washed sequentially in methanol, acetone, and DI water, then blown dry with ultra-high purity nitrogen. The coupons were then loaded into the load lock chamber following procedures that have been detailed earlier.[35]

The in situ deposited Si_3N_4 films were grown using pulsed electron-enhanced chemical vapor deposition (EE-CVD). For this Si_3N_4 pulsed EE-CVD, an NH_3 RBG was flowed through

the chamber during electron beam irradiation of the sample. Throughout this continuous electron beam and NH_3 exposure, Si_2H_6 was pulsed into the chamber every 5 seconds. In situ ellipsometry measurements observed that the Si_3N_4 films nucleated on the first Si_2H_6 pulse and grew linearly versus number of Si_2H_6 exposures. The Si_3N_4 pulsed EE-CVD films were grown to a thickness of ~10 nm. The Si_3N_4 pulsed EE-CVD films had high purity as measured by in vacuo AES. The films displayed a nearly stoichiometric 3:4 Si:N ratio with C and O impurities <2 at%. In addition, the Si_3N_4 pulsed EE-CVD films were smooth as measured by ex situ AFM with an RMS roughness of <2 Å.

The TiN EE-ALD growth was conducted using a pulse sequence consisting of: (1) TDMAT dose; (2) pump time; (3) electron beam exposure; and (4) pump time before the next TDMAT dose. The timing for this pulsing sequence can be characterized by (t_1, t_2, t_3, t_4). For deposition on the silicon native oxide and the SiO_2 thermal oxide, the TDMAT precursor was maintained at P=0.3 Torr behind a micropulse valve. The valve was actuated for t_1 = 1 s. The valve opening led to a transient pressure in the main chamber of 4 x 10^{-7} Torr as measured by the cold cathode gauge. The pressure at the sample was higher because the micropulse valve was connected to a ¼" diameter tube that led to the sample and ended ~ 5 cm from the sample. For deposition on the in situ deposited Si_3N_4, the valve was actuated for 2 s. The TDMAT pressure was 0.2 Torr behind the micropulse valve. These conditions yielded a transient pressure of 6 x 10^{-7} Torr.

Pumping was then performed for a total of t_2 = 2 s. Subsequently, the electron exposure was performed with a grid bias of 100 V for t_3 = 20 s, with an electron current measured at the sample stage of ~25 mA. The next TDMAT adsorption was then conducted after a pump time of

t_4 = 1 s. The timing for this pulsing sequence was (1, 2, 20, 1). The sum of these steps produced a reaction cycle time of ~24 s.

In situ ellipsometry measurements were collected every second throughout the deposition. The in situ ellipsometer used four wavelengths of light. The precision of the in situ ellipsometry measurements of film thickness was within ± 0.03 Å. The in situ ellipsometer used a Drude-Lorentz model to model the TiN films. The software (Filmsense) was able to extrapolate resistivity from the model. Ex situ spectroscopic ellipsometry (Model M-2000, J.A. Woollam Co., Inc.) was also performed to measure the film thickness of some samples after taking them from the reactor. The data was fit using a Drude-Lorentz model with a Drude oscillator[130] (119 μΩ·cm resistivity, 0.952 fs scattering time) and one Lorentzian oscillator (center energy: 5.385 eV, amplitude: 6.519, broadening: 3.980 eV).

A four-point probe (Signatone, QP2-MB8) was used for ex situ resistivity measurements. The probe spacing was 1 mm. The geometric correction factor was chosen based on the ratio of the probe spacing to the diameter of the largest inset circle possible on the wafer coupon. A typical geometric correction factor was 0.92. AFM measurements were used to monitor ex situ film roughness. The AFM measurements were performed with an AFM instrument (Park NX10) using non-contact mode. The scan rate was 0.3-0.8 Hz for a 1x1 μm area using a micro cantilever probe (Olympus, OMCL-AC160TS).

X-ray Reflectivity (XRR) was used to determine film thickness and density. Grazing incidence x-ray diffraction (GI-XRD) determined crystallinity of the films. Both GI-XRD and XRR scans were performed using a XRD instrument (Bede D1, Jordan Valley Semiconductors) with radiation from Cu Kα (λ=1.540 Å). The X-ray tube filament voltage was 40 kV and the current was 35 mA. The incident angle used for GI-XRD was 0.3°. The XRR scan range was

300 to 6000 arcsec with a 5 arcsec step size. The XRR scans were analyzed using modeling software (REFS, Jordan Valley Semiconductors).

The film composition was determined using an X-ray photoelectron spectrometer (PHI 5600) using a monochromatic Al Kα source with an energy of 1486.6 eV. The pass energy was 58.7 eV, the step size was 0.25 eV, and the dwell time was 50 ms per step. An electron beam neutralizer was used during the XPS measurements. The Ar ion beam energy during depth profiling was 3 keV. The XPS data were collected using Auger Scan (RBD Instruments) software. The XPS data were analyzed in CASA XPS (Casa Software Ltd.) software.

4.4 Results and Discussion

4.4.1 Nucleation Regime for TiN EE-ALD

The TiN EE-ALD films grown in the presence of the NH_3 RBG nucleated rapidly on the Si native oxide, thermal SiO_2 and the in situ deposited Si_3N_4 EE-CVD films. Figure 4-2

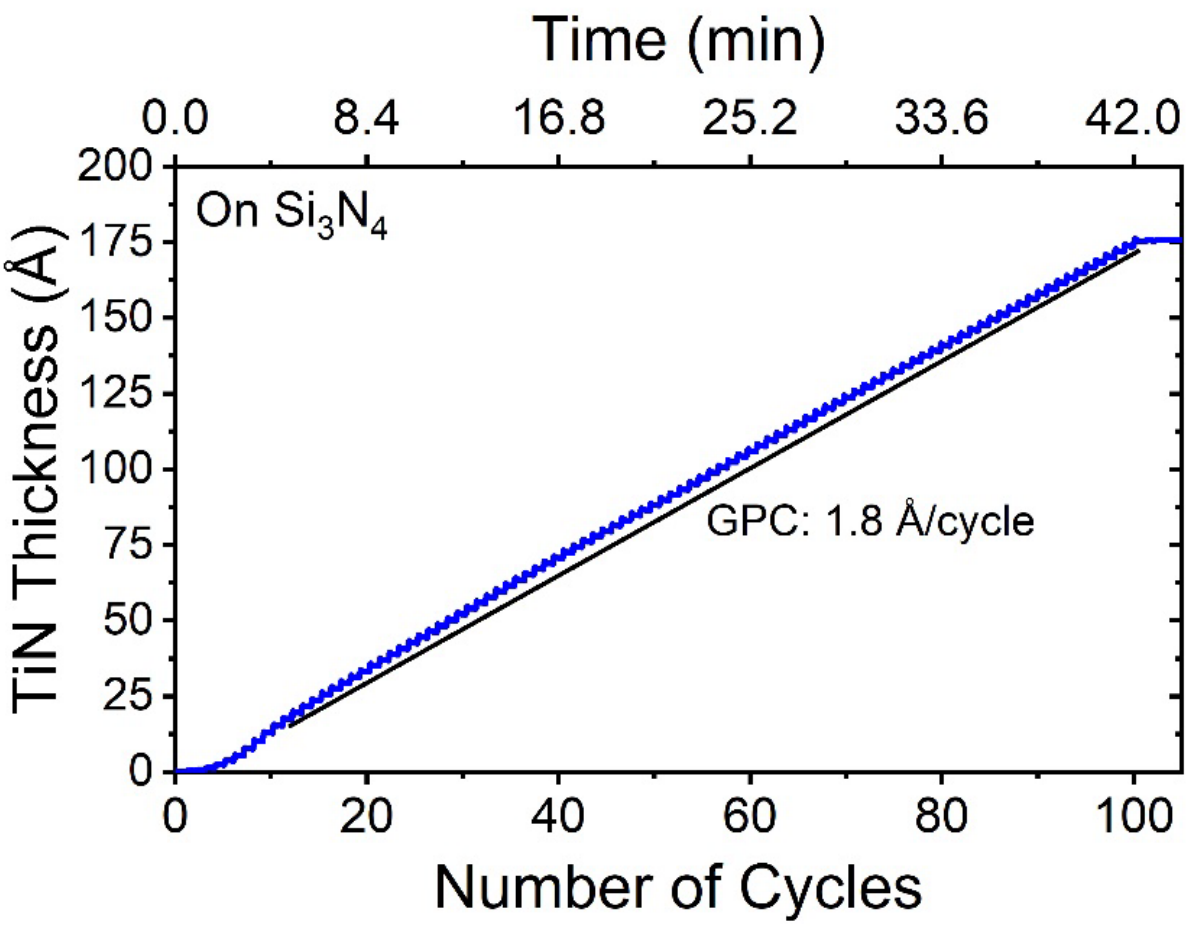

Figure 4-2. Nucleation and growth of TiN EE-ALD film thickness on Si_3N_4 versus number of EE-ALD cycles measured using in situ ellipsometry. Pulsing sequence in seconds was (2, 2, 20, 1) with NH_3 background pressure of ~1 mTorr. Growth per cycle was 1.8 Å/cycle.

displays the growth of a TiN EE-ALD film on an in situ deposited Si_3N_4 EE-CVD film. These in situ ellipsometry measurements were performed in real time during TiN EE-ALD. The timing sequence in seconds was (2, 2, 20, 1) with a NH_3 RBG at ~1 mTorr and a TDMAT pressure of 0.2 Torr behind the micropulse valve. The TDMAT exposures produced a pressure transient of 6 x 10^{-7} Torr in an empty reactor.

Figure 4-2 shows that the TiN EE-ALD film nucleates quickly and then grows with a growth per cycle (GPC) of 1.8 Å/cycle. An expansion of the first 10 EE-ALD cycles from the ellipsometric results in Figure 4-2 is given in Figure 4-3.

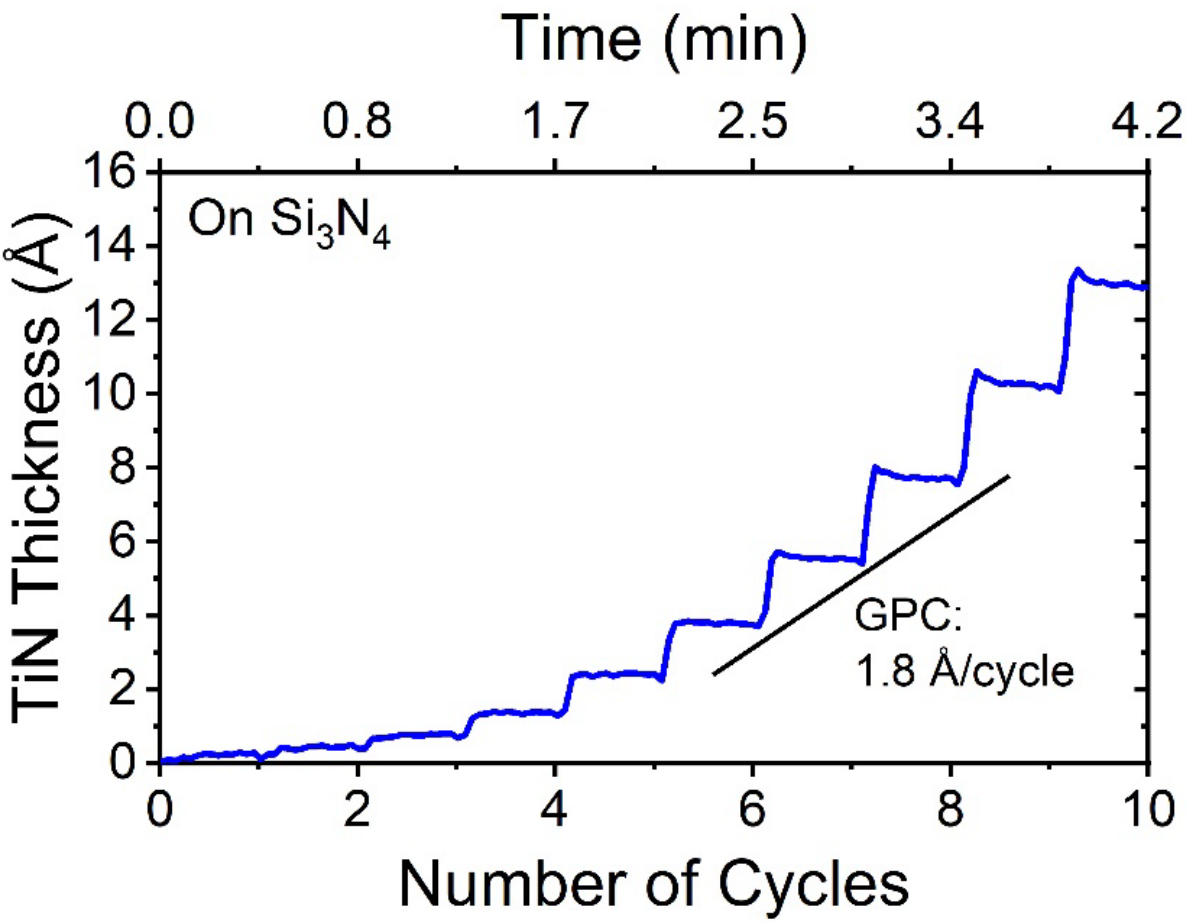

Figure 4-3. Expansion of nucleation region in Figure 4-2 showing first 10 EE-ALD cycles. Growth per cycle of 1.8 Å/cycle was obtained after 6 EE-ALD cycles.

The TiN EE-ALD reaches the GPC of 1.8 Å/cycle after only 6-7 cycles. The small nucleation delay of 7 cycles allows for continuous sub 1 nm films as seen in Figure 4-3.

Additional experiments determined that the TiN EE-ALD growth rates were dependent on the TDMAT precursor exposures. At higher TDMAT precursor exposures, the GPCs could reach >5 Å/cycle. These larger GPCs could be explained by larger TDMAT coverages adsorbed on the growing TiN surface after higher TDMAT exposures. Earlier experiments have confirmed that TDMAT adsorbs with a coverage-dependent sticking coefficient on TiN surfaces.[131] The adsorbed TDMAT then desorbs with a coverage-dependent desorption rate.[131]

There also may be partial decomposition of TDMAT on electron-activated substrates through a mechanism like autocatalytic deposition.[16, 62, 132] This mechanism could lead to the buildup of thick films with partially decomposed TDMAT precursors. To avoid these larger GPCs and higher carbon impurities in the TiN EE-ALD film, most of the results shown in this paper were obtained with shorter TDMAT precursor exposures of 1 s with TDMAT pressures of 0.3 Torr behind the micropulse valve. These TDMAT exposures produced a pressure transient of 4×10^{-7} Torr in an empty reactor.

The TiN EE-ALD films grown using the NH_3 RBG also nucleated rapidly on the Si native oxide. Figure 4-4

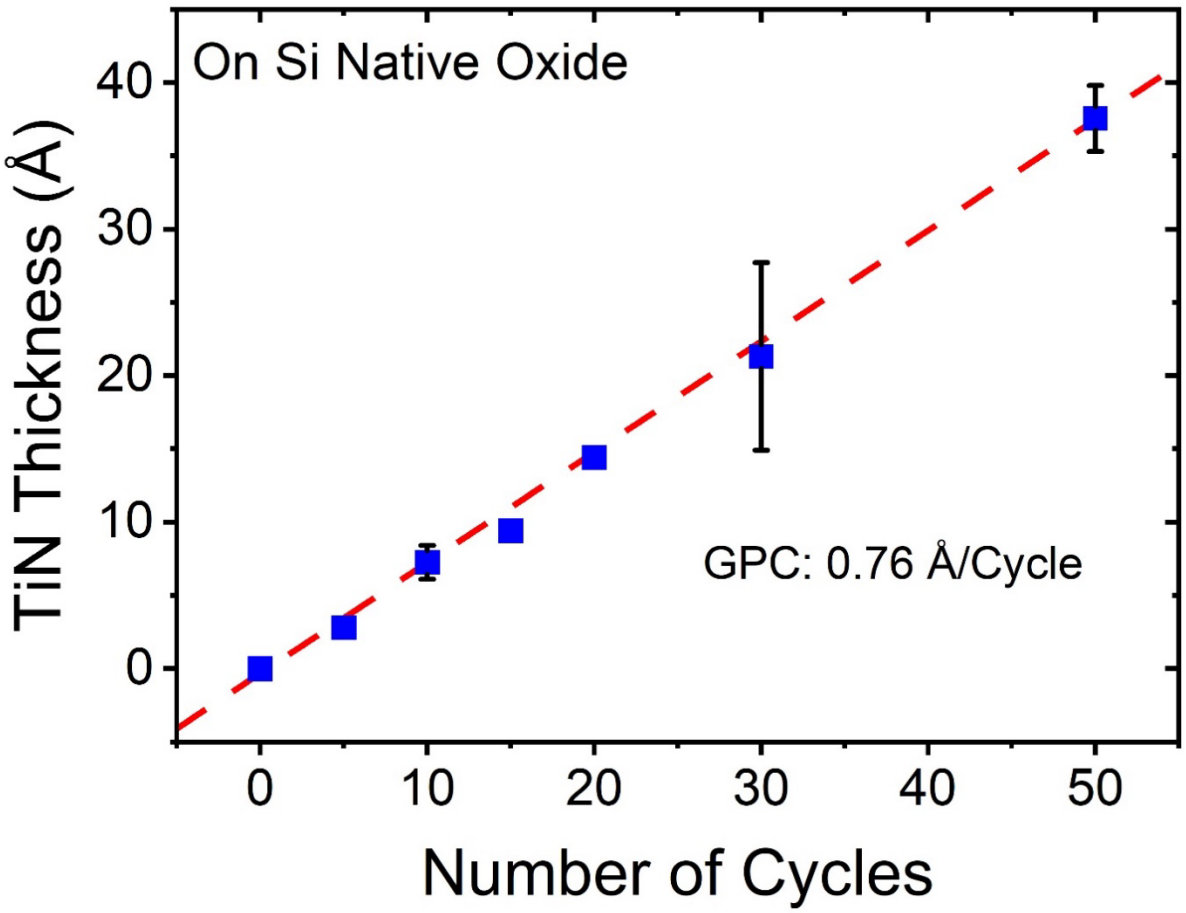

Figure 4-4. TiN EE-ALD film thickness on Si native oxide versus number of EE-ALD cycles measured using in situ ellipsometry. Pulsing sequence in seconds was (1, 2, 20, 1) with NH_3 background pressure of ~1 mTorr. Growth per cycle was 0.76 Å/cycle. Error bars are shown on points with more than one experiment.

displays the TiN thickness versus number of EE-ALD cycles. The dosing sequence was (1-2-20-1) with a TDMAT pressure of 0.3 Torr behind the micropulse valve. Each data point represents a separate sample. The samples were removed from the reactor after a certain number of EE-ALD cycles for subsequent analysis. The TiN thickness increased linearly with increasing number of cycles with a GPC of 0.76 Å/cycle. The GPC was lower because the TDMAT exposure was lower compared with the TDMAT exposures employed for Figure 4-2 and Figure

4-3. A linear regression through the values for the TiN thickness versus number of EE-ALD cycles showed that the x-intercept was at 1 EE-ALD cycle. This x-intercept is interpreted as a nucleation delay of 1 EE-ALD cycle.

The nucleation of TiN EE-ALD on Si native oxide was also explored using in vacuo AES after various numbers of EE-ALD cycles. These AES results are for the same set of samples as shown in Figure 4-4. After each TiN deposition, the main chamber was pumped down to ~$1x10^{-7}$ Torr. The sample was then transferred to the AES chamber, scanned to obtain the AES spectrum, and removed from the reactor for subsequent analysis. This process was repeated for 5, 10, 15, 20, 30 and 50 TiN EE-ALD cycles.

Figure 4-5

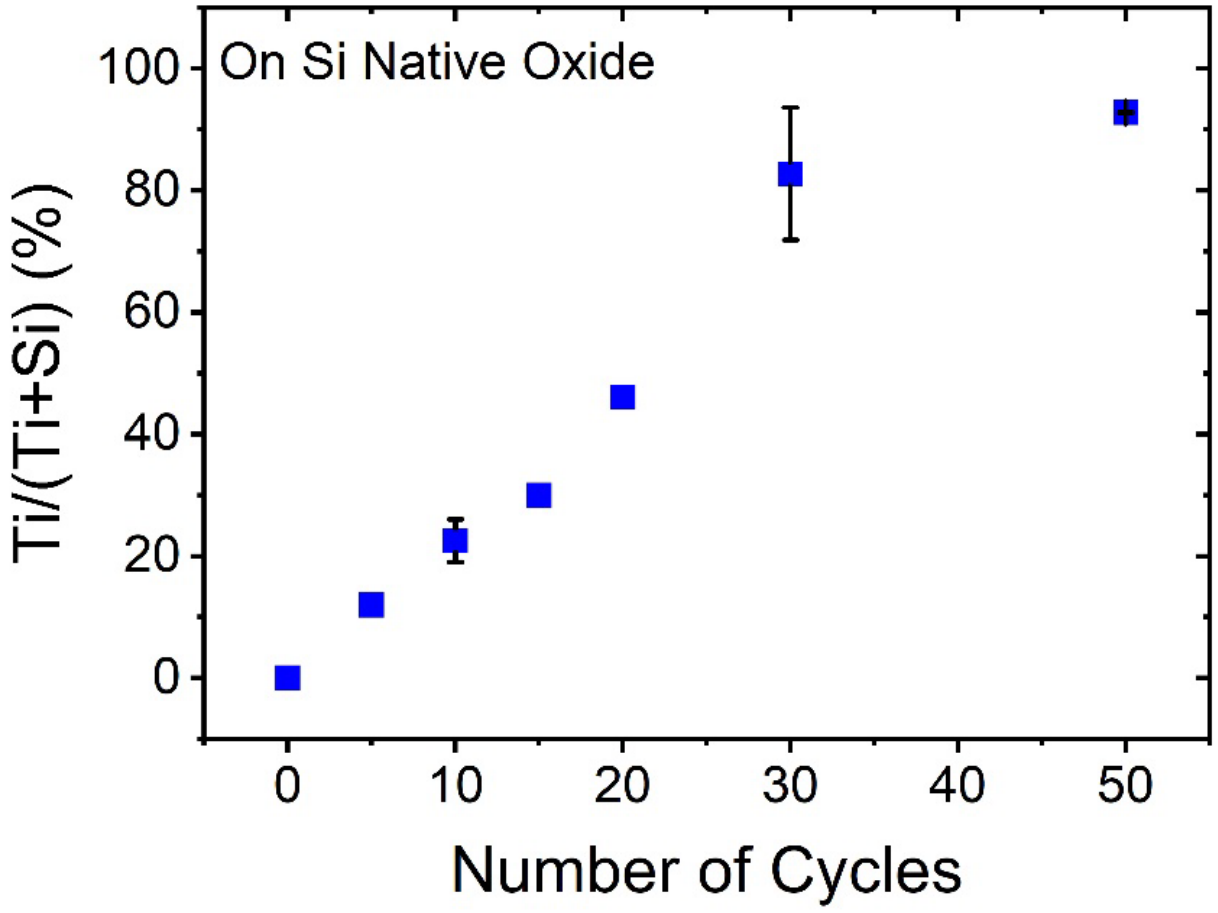

Figure 4-5. In vacuo Auger electron spectroscopy (AES) measurement of ratio of AES signals Ti / (Ti+Si) (%) during TiN EE-ALD on Si native oxide versus number of EE-ALD cycles. Pulsing sequence in seconds was (1, 2, 20, 1) with NH_3 background pressure of ~1 mTorr. Ti/(Ti+Si) (%) approaches 100% when TiN EE-ALD film blocks AES electrons from underlying Si substrate.

shows the results for the Ti/(Ti+ Si) ratio of AES signals versus number of EE-ALD cycles. The Ti/(Ti + Si) ratio of AES signals increases linearly with increasing number of cycles over the first 30 EE-ALD cycles. After ~30 EE-ALD cycles, the Ti and Si AES signals reach limiting values because of the finite mean free path for the Auger electrons in the TiN film. The Ti AES signal reaches the limiting value for a bulk TiN film. The Si AES signal becomes completely attenuated by the overlying TiN film. The limiting value for the Ti/(Ti + Si) ratio at values

slightly less than 100% can be explained by noise in the AES spectrum near the Si peak that leads to a finite apparent Si AES signal.

The roughness of the TiN EE-ALD films in the initial nucleation region on the Si native oxide was also studied by ex situ AFM measurements. These roughness results are for the same set of samples as shown in Figure 4-4 and Figure 4-5. Figure 4-6

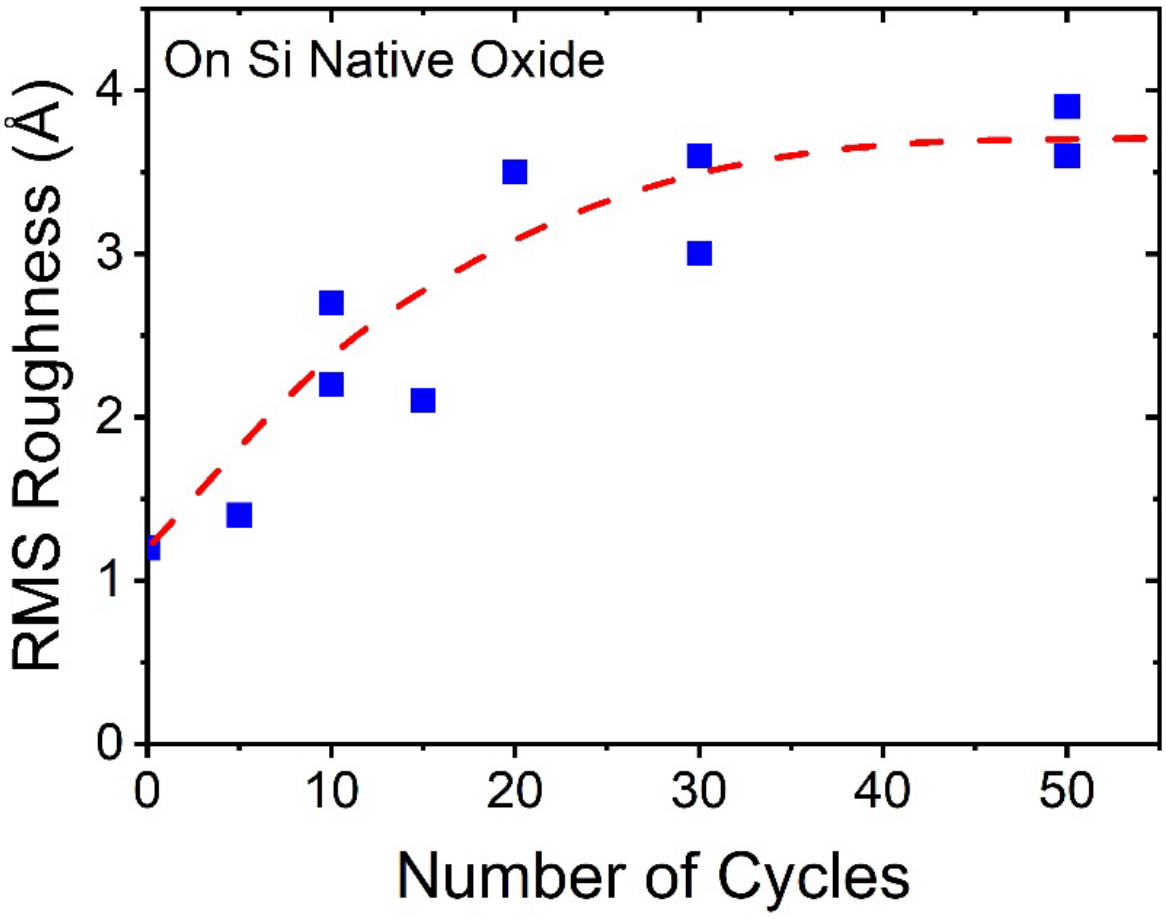

Figure 4-6. RMS roughness measured by AFM for TiN EE-ALD film of Si native oxide versus number EE-ALD cycles. Pulsing sequence in seconds was (1, 2, 20, 1) with NH_3 background pressure of ~1 mTorr.

displays the RMS roughness values measured by the AFM versus number of EE-ALD cycles. The RMS roughness for a bare, cleaned Si coupon was ~4 Å. After a 5-minute electron exposure with NH_3 RBG at ~1 mTorr, the RMS roughness dropped to ~1 Å. This RMS roughness was used for the RMS roughness at 0 cycles of TiN EE-ALD in Figure 4-6. The RMS roughness then increases slowly by ~3 Å over 50 EE-ALD cycles. The resulting RMS surface roughness reaches a limiting value at ~4 Å.

The change in the surface roughness of the Si native oxide resulting from the initial 5-minute electron exposure with NH_3 RBG motivated a study of the change in surface composition using in vacuo AES. One Si native oxide sample was loaded and irradiated with the electron beam and exposed to the NH_3 RBG at ~1 mTorr for 5 minutes with an electron sample current of 20 mA as a control. This control sample showed ~40 at% N on the surface as measured by in vacuo AES. This N AES signal results from surface nitridation by $\bullet NH_2$ species from the electron beam interaction with the NH_3 RBG. In addition, the oxygen and carbon AES signals decreased by factors of 2.7 and 2.3, respectively, relative to initial Si native oxide samples that were not subjected to the electron exposures with NH_3 RBG. These experiments suggest that surface cleaning and smoothing results from the electron exposures with NH_3 RBG. The electrons are required to initiate the deposition of TDMAT and the cleaning effect of NH_3. There is no growth on any substrate if the NH_3 and TDMAT are dosed into the chamber with the HC-PES off.

4.4.2 Steady State Growth for TiN EE-ALD

In situ ellipsometry was used to monitor the TiN EE-ALD in the steady state growth regime using sequential exposures of TDMAT and electrons with a NH_3 RBG in the chamber as illustrated in Figure 4-1. Figure 4-7

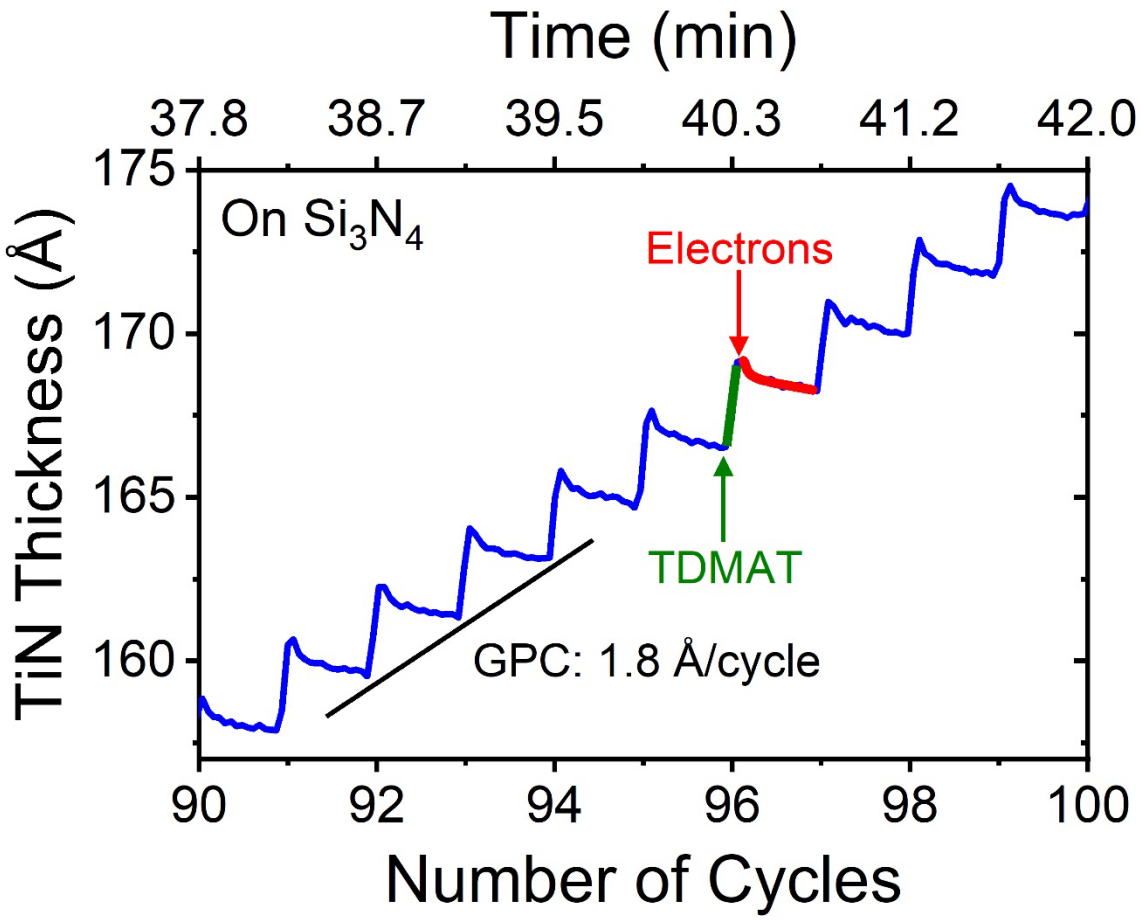

Figure 4-7. Expansion of steady state region in Figure 4-2 showing TiN EE-ALD film thickness on Si_3N_4 versus number of EE-ALD cycles measured using in situ ellipsometry. Pulsing sequence in seconds was (2, 2, 20, 1) with NH_3 background pressure of ~1 mTorr. Growth per cycle was 1.8 Å/cycle.

shows the results for 10 cycles during 90-100 EE-ALD cycles on the in situ grown Si_3N_4 EE-CVD film. These 10 cycles were also displayed at lower resolution in Figure 4-2. The dosing sequence was (2-2-20-1) with a TDMAT pressure of 0.2 Torr behind the micropulse valve. The film thickness increases resulting from TDMAT adsorption during the TDMAT exposures. During the electron exposure, the TiN thickness decreases resulting from the ESD of surface

species. The surface species are believed to be the dimethylamine ligands on the TDMAT adsorption products.

Initially the thickness decreases quickly during the electron exposure. Subsequently, there is a slow decrease of the thickness. This slow decrease may be the additional loss of dimethylamine ligands or removal of fragmented dimethylamine ligands by the NH_3 RBG. An electron exposure of 20 s was chosen because shorter electron exposures led to higher C content in the films. The effect of the electron beam exposure time had a dramatic effect on the purity of the TiN film.

Figure 4-8

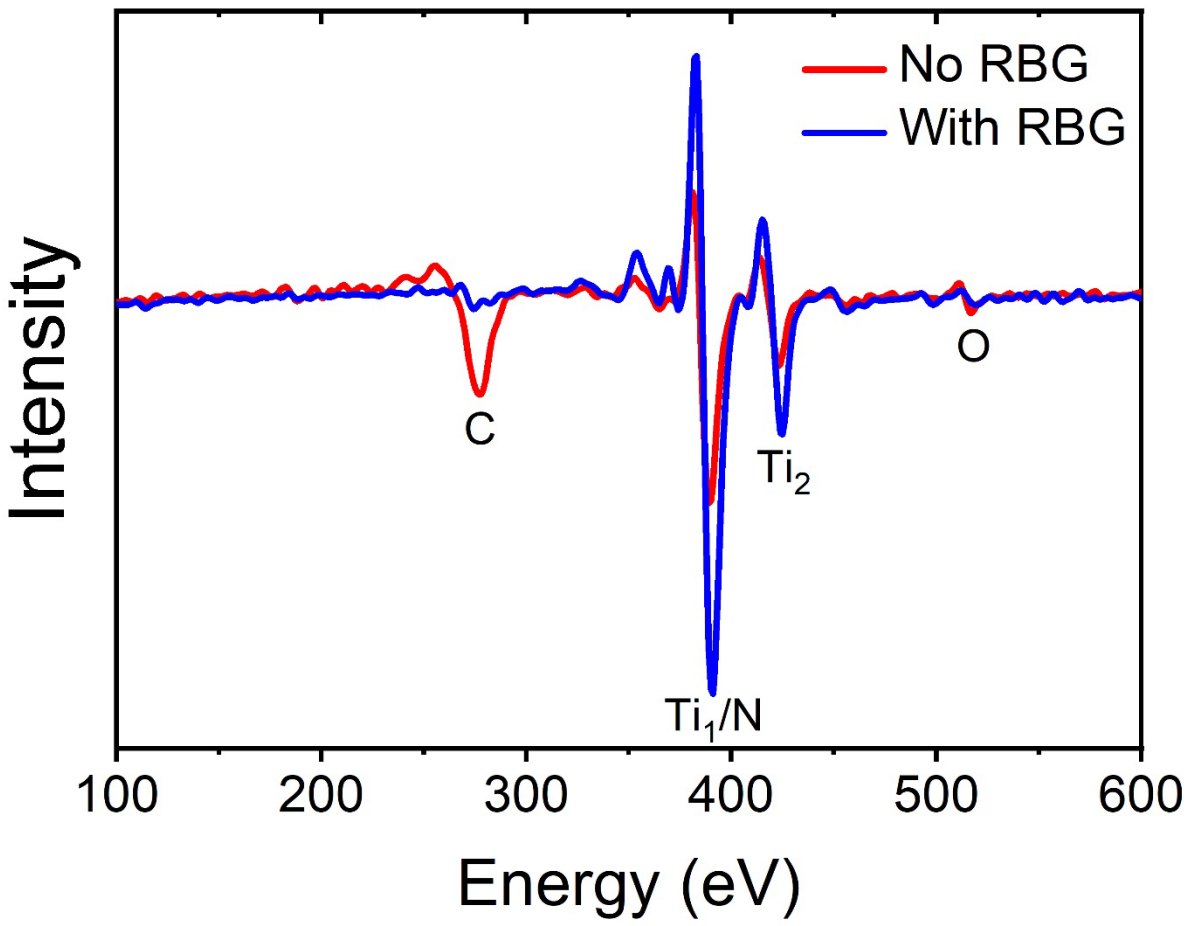

Figure 4-8. In vacuo AES showing AES signals for C, Ti, Ti/N and O for TiN EE-ALD films grown on Si_3N_4. Pulsing sequence in seconds was (2, 2, 20, 1). TiN EE-ALD film grown with no RBG used 27 EE-ALD cycles. TiN EE-ALD film grown with NH_3 RBG utilized 50 EE-ALD cycles. C AES signal is much lower when NH_3 RBG was present at ~1 mTorr.

shows the in vacuo AES results for TiN EE-ALD with and without the NH_3 RBG. The dosing sequence was (2-2-20-1) with a TDMAT pressure of 0.2 Torr behind the micropulse valve. The TiN EE-ALD film grown with no NH_3 RBG used 27 EE-ALD cycles. The NH_3 TiN EE-ALD film grown with the NH_3 RBG utilized 50 EE-ALD cycles. Without an NH_3 RBG, the in vacuo AES measured a C content in the as-deposited TiN film of ~60 at%. In contrast, with the NH_3

RBG, the C content in the as-deposited TiN film was ~3 at%. These results illustrate that the NH_3 RBG greatly enhances the purity of the TiN EE-ALD films.

In vacuo AES measurements also confirmed that the TiN EE-ALD films deposited with larger TDMAT precursor exposures contained more carbon. With the electron exposure held constant, the carbon content in the film increased for larger TDMAT precursor exposures. Carbon compositions of >30 at% were observed when the TiN EE-ALD GPC was 7 Å/cycle. These larger carbon contents were obtained with a TDMAT precursor exposure of 1 s with TDMAT pressure behind the micropulse valve of >0.6 Torr.

AES was able to quantify Si, O, and C using primary AES peaks, and Ti using a secondary AES peak. Unfortunately, the primary N AES peak overlapped with the primary Ti AES peak. There were no other useable N AES peaks. Consequently, ex situ XPS depth profiling was also used to quantify the TiN EE-ALD film composition.

An XPS depth profile revealed very low impurities for a TiN EE-ALD film grown on Si native oxide with a dosing sequence of (1-2-20-1) with a TDMAT pressure of 0.3 Torr behind the micropulse valve. The C and O content were measured at 1.5 and 1.7 at%, respectively. The Ti:N ratio was 1:1.17. This extra nitrogen may have been due to N stuffing at grain boundaries and vacancies. This N content in the grain boundaries may be beneficial for the diffusion barrier properties.[112, 123]

Grazing incidence x-ray diffraction (GI-XRD) was used to determine the crystallinity of the TiN EE-ALD films. Despite low growth temperatures <70 °C, the TiN films display crystallinity. The GI-XRD results are shown in Figure 4-9

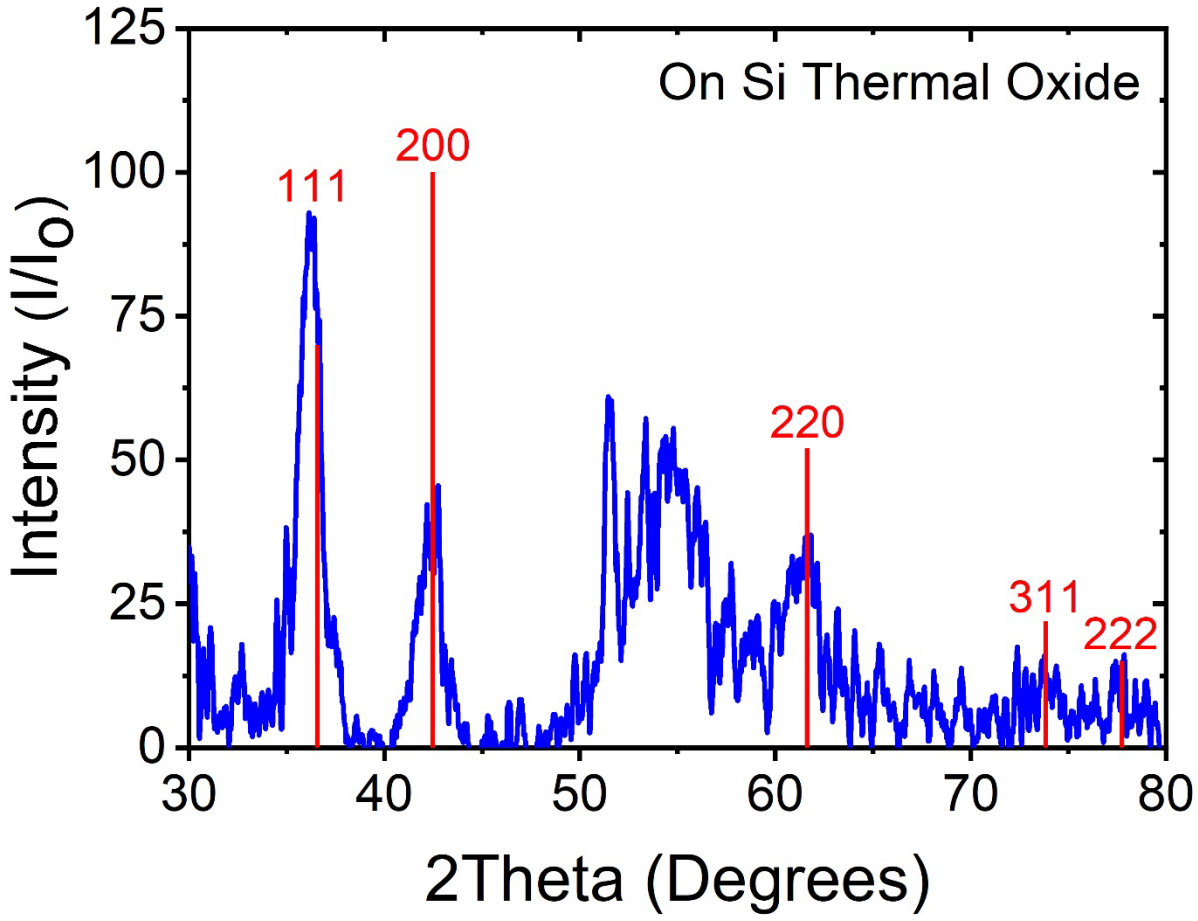

Figure 4-9. Grazing incidence x-ray diffraction (GIXRD) of TiN EE-ALD films grown on Si thermal oxide after 200 EE-ALD cycles. Pulsing sequence in seconds was (1, 2, 20, 1) with NH_3 background pressure of ~1 mTorr. Miller indices of diffraction peaks for crystalline TiN are shown for comparison.

for a TiN EE-ALD film with a thickness of 13.1 nm deposited on Si thermal oxide using 200 EE-ALD cycles. The dosing sequence was (1-2-20-1) with a TDMAT pressure of 0.3 Torr behind the micropulse valve.

The <111> and <200> peaks of crystalline TiN match the diffraction peaks in Figure 4-9.[133] The <220>, <311>, and <222> peaks of crystalline TiN are also discernable above

baseline. The Scherrer equation yields an average grain size of 8.9 nm for all 5 fitted peaks. The broad peak at 2Θ ~55° is attributed to the <311> planes in crystalline silicon.[134]

X-ray reflectometry (XRR) was also used to measure the density of the TiN EE-ALD films. The average density of the films was 5.3 g/cm^3. This density is 98% of theoretical TiN bulk density of 5.4 g/cm^3. This high density suggests that these TiN films will be resistant to oxidation. This oxidation resistance has been confirmed by depth profile XPS measurements where there is minimal O diffusion into the TiN films. This behavior is in contrast to thermal TiN ALD films that display high porosity leading to facile oxidation.[120]

4.4.3 Mechanism for TiN EE-ALD with Reactive Background Gas

The TiN EE-ALD grown with the NH_3 RBG at <70 °C have high purity, high density, and crystallinity. The NH_3 RBG is facilitating the growth of these films. An illustration of TiN EE-ALD using TDMAT and low energy electrons in the presence of a continuous NH_3 RBG is shown in Figure 4-10.

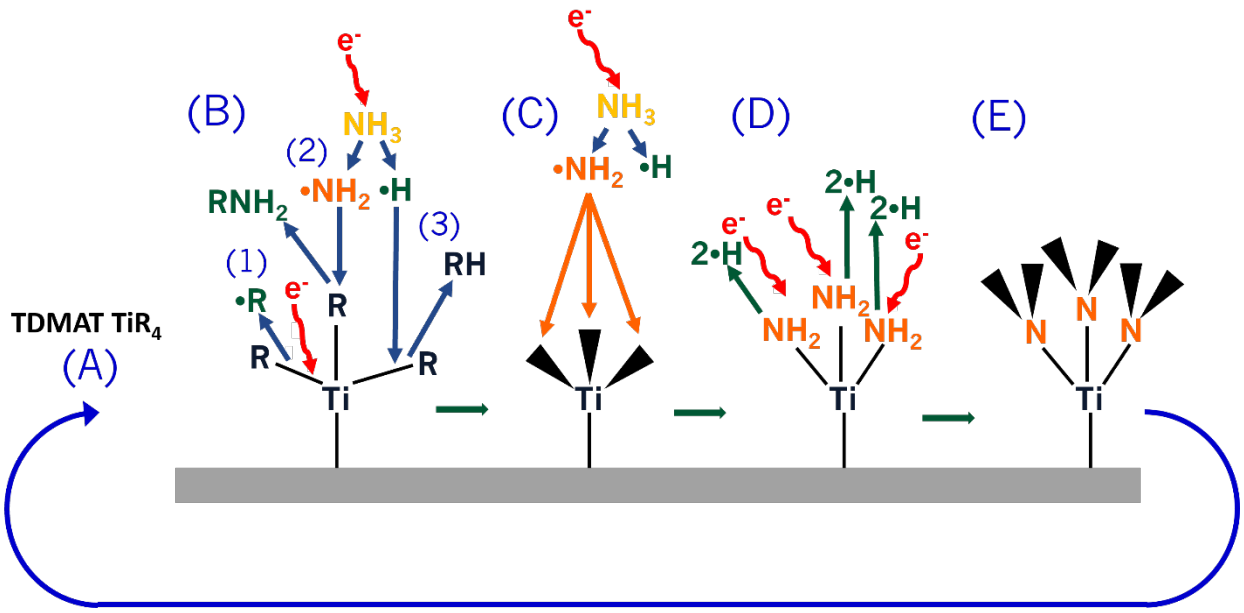

Figure 4-10. Mechanism for TiN EE-ALD showing: (A) adsorption of the TDMAT (TiR_4) precursor; (B) removal of –R ligands by: (1) ESD, (2) $\bullet NH_2$ radicals, and (3) •H radicals; (C) passivation of Ti dangling bonds by $\bullet NH_2$; (D) removal of –H by ESD (shown) or radical abstraction processes (not shown); and (E) activated TiN surface for precursor adsorption.

The electrons are believed to play a key role by dissociating NH_3 in the gas phase to produce $\bullet NH_2$ and •H radicals. These radicals can adsorb onto empty sites on the TiN surface. In addition, these radicals can abstract dimethylamine ligands from TDMAT adsorption products on the surface.

In addition to dissociating NH_3 in the gas phase, the electrons can also desorb H from $-NH_2$ species on the surface. This H ESD produces additional empty sites on the TiN surface. The TDMAT precursor can then adsorb onto these empty sites to add more Ti to the TiN surface. The electrons may also crack dimethylamine ligands on the surface and produce carbon fragments. However, the continuous flux of $\bullet NH_2$ and •H radicals from NH_3 dissociation may be

able to remove this surface carbon as CH_3NH_2 or CH_4. The •H radicals may also provide a pathway for the removal of oxygen impurities as H_2O.

The primary motivation for introducing the NH_3 RBG was to ensure the complete nitridation of the TiN film. The effect of the NH_3 RBG on the film purity was an unexpected bonus that is attributed to the cleaning effect of the $•NH_2$ and •H radicals. In addition, the possibility of introducing various RBGs offers a new parameter to tune the composition of EE-ALD films. Different films could be deposited from a single metal precursor, such as TDMAT, by changing the RBG. For example, the dissociation or adsorption of NH_3, Si_2H_6, CH_4, or B_2H_6 RBGs should form nitrides, silicides, carbides, or borides, respectively, with the metal precursor. The single RBG could also be extended to two or three RBGs to deposit ternary or quaternary EE-ALD films.

4.4.4 Resistivity of TiN EE-ALD Films

The resistivity of the TiN EE-ALD films was characterized using in situ 4 wavelength ellipsometry and ex situ spectroscopic ellipsometry. To confirm that the TiN EE-ALD films were comparable with other TiN films, Figure 4-11

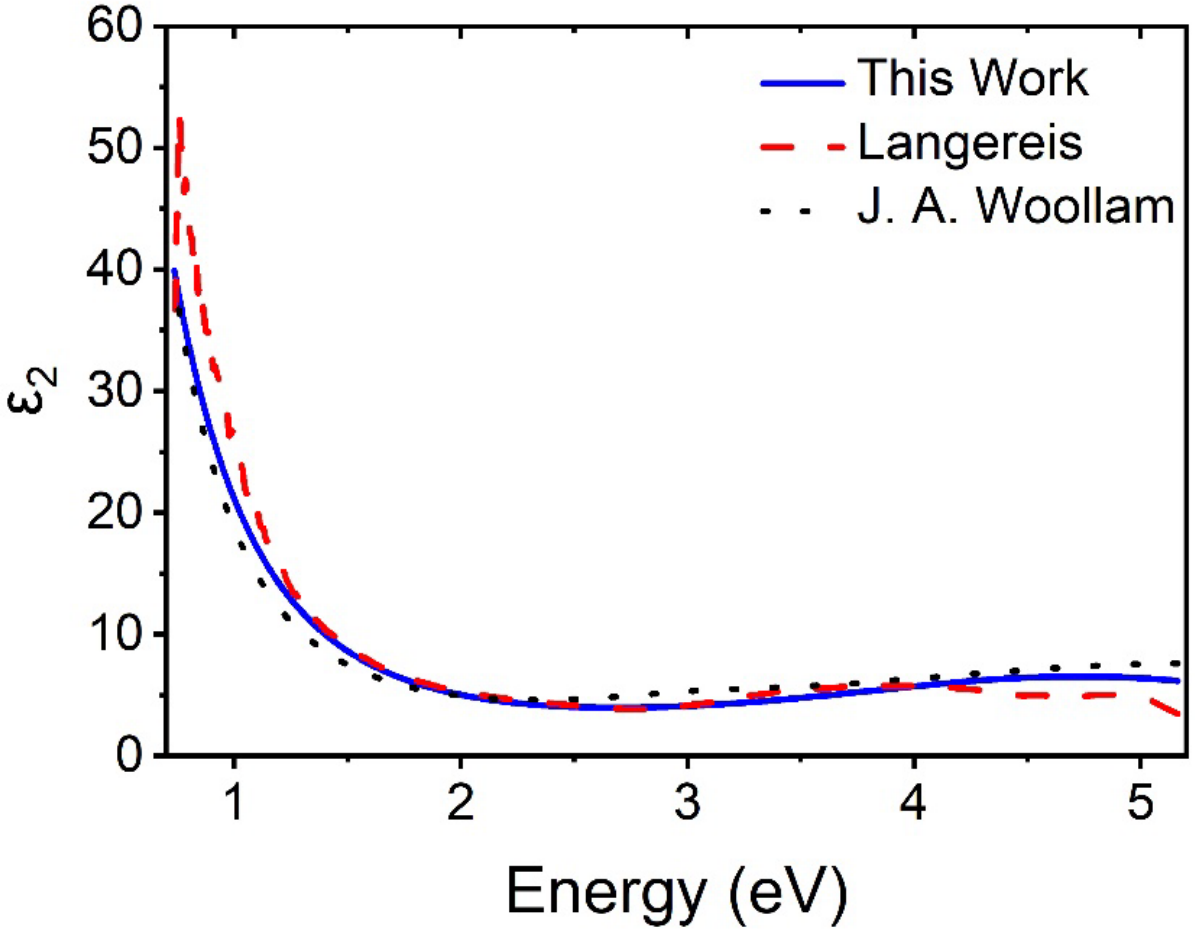

Figure 4-11. Comparison of experimentally measured imaginary part of the pseudo dielectric function (ε_2) between TiN EE-ALD film on SiO_2 thermal oxide (this work), PE-ALD TiN film (Reference [40]) and results for TiN in J.A. Woollam database. For TiN EE-ALD film on SiO_2 thermal oxide, pulsing sequence in seconds was (1, 2, 20, 1) with NH_3 background pressure of ~1 mTorr.

displays the results for the imaginary part of the pseudo dielectric function (ε_2) for the TiN EE-ALD films, TiN plasma-enhanced ALD (PE-ALD) films reported in the literature by Langereis et al.,[40] and TiN films reported in the J.A. Woollam CompleteEASE database. The results shown for the TiN EE-ALD film were obtained using ex situ spectroscopic ellipsometry.

Figure 4-11 shows that there is excellent agreement between these three data sets. This good correlation includes the ε_2 results at low energy where the Drude term in the ellipsometry model is related to the film resistivity. The good agreement between the ellipsometry model employed in this work and the available literature models suggests both that the model used in this work is accurate and the TiN EE-ALD film is high quality TiN.

The in situ ellipsometry results for the thickness and resistivity of a TiN EE-ALD film are displayed in Figure 4-12.

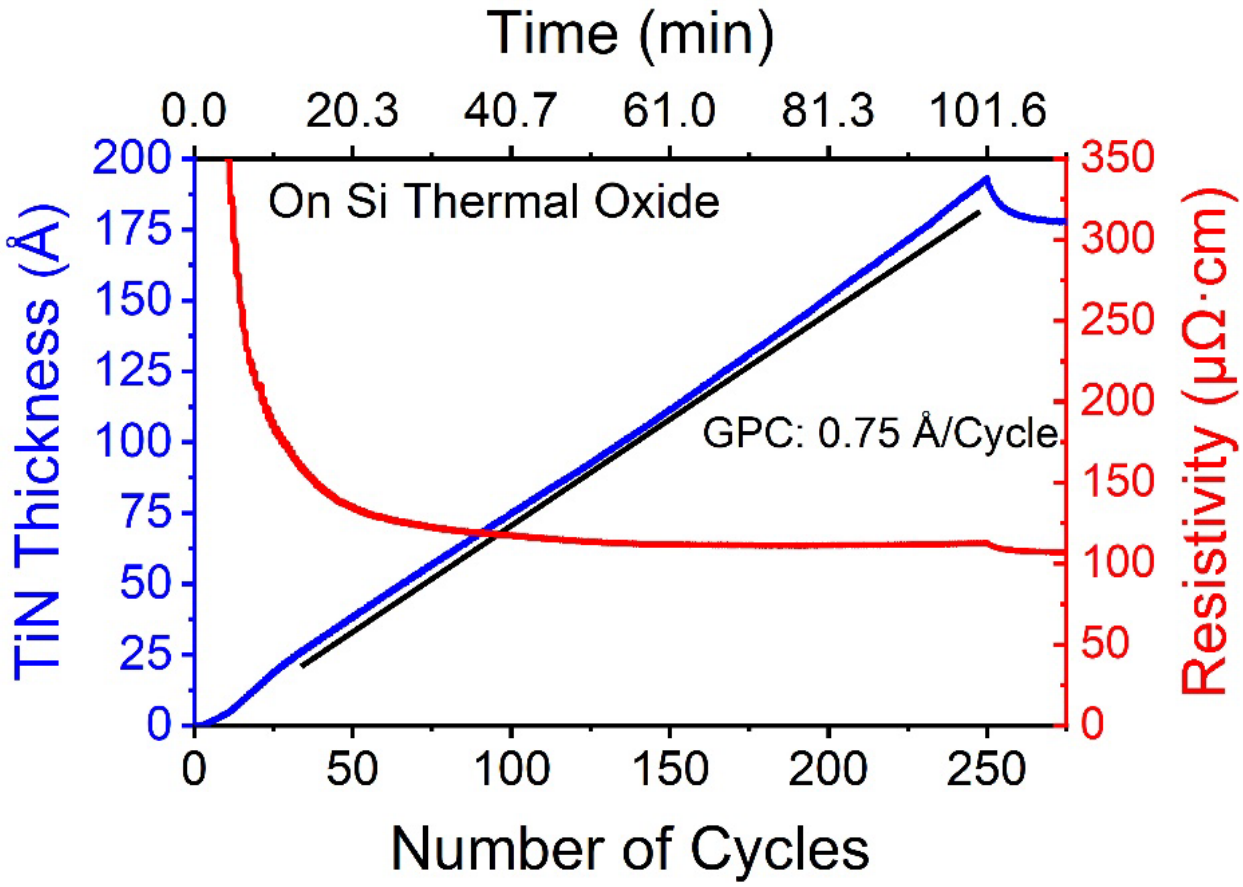

Figure 4-12. TiN EE-ALD film thickness and resistivity on Si thermal oxide versus number of EE-ALD cycles measured using in situ ellipsometry. Pulsing sequence in seconds was (1, 2, 20, 1) with NH_3 background pressure of ~1 mTorr. Growth per cycle was 0.75 Å/cycle. Resistivity reaches a value of ~110 μΩ cm after >100 EE-ALD cycles at TiN EE-ALD film thickness of >60 Å.

These results are for TiN EE-ALD on a Si thermal oxide with a thickness of 400 nm. The dosing sequence was (1-2-20-1) with a TDMAT pressure of 0.3 Torr behind the micropulse valve. Similar to the earlier results in Figure 4-2, Figure 4-3, Figure 4-4, and Figure 4-5, there is rapid nucleation of the TiN EE-ALD film. The TiN film then grows linearly with a GPC of 0.75 Å/cycle over 250 EE-ALD cycles. Figure 4-12 also shows the corresponding resistivity of the TiN film determined from the Drude term in the ellipsometry model.

The film resistivity drops rapidly in the nucleation regime during the first 12-13 cycles. These resistivities are artificially low for film thicknesses <4 nm resulting from the inability of ellipsometry to fully account for electron scattering at grain boundaries and interfaces.[39] The film resistivity continues to decrease progressively and reaches a resistivity of ~130 μΩ·cm after 50 cycles at a film thickness of ~40 Å. The resistivity continues to decrease slowly as the film thickness increases to ~185 Å where the resistivity is ~110 μΩ·cm after 250 cycles.

The EE-ALD is stopped after 250 cycles. Without the electron current impinging on the sample, the film begins to cool slightly from ~65 °C over the next ~10 minutes. This cooling results in an apparent decrease in the model film thickness of ~16 Å and a corresponding decrease in resistivity to 104 μΩ·cm. The apparent decrease in the model film thickness is associated with the temperature change of the film. The electronic properties change with temperature. The ellipsometry model interprets this temperature change as a change in film thickness.

The TiN EE-ALD film after 250 cycles in Figure 4-12 was also characterized by ex situ spectroscopic ellipsometry. The thickness for this film was calculated to be 173 Å from a 9-point map over a 1.5 x 1.5 cm area of the sample. This thickness is in good agreement with the thickness of 169 Å determined by the in situ ellipsometry after the sample cooled following the

electron exposure. The Drude-Lorentz model used for the ex situ spectroscopic ellipsometry over the same 9 points gave a resistivity of 125 μΩ·cm. This resistivity is in good agreement with the resistivity of 104 μΩ·cm determined by the in situ ellipsometry.

Four-point probe measurements were also employed to corroborate the resistivity measurements from ellipsometry. A geometric correction factor of 0.92 was applied to the raw resistivity data to account for the small coupon size. A resistivity of 131 μΩ·cm was obtained from 10 locations at the center of substrate immediately after removal of the sample from the deposition chamber. This resistivity is also in good agreement with the resistivity from the ellipsometry measurements. There was a negligible increase in resistivity from the four-point probe measurement over a 24-hour period after removing the film from vacuum. No increase in resistivity after prolonged air exposure suggests a dense TiN film that is resistant to oxidation.

Additional experiments were conducted on a 400 nm Si thermal oxide with 150 and 200 TiN EE-ALD cycles. These experiments were performed using the same reaction conditions as employed for the 250 TiN EE-ALD cycles shown in Figure 4-12. The results from the in situ ellipsometry, ex situ spectroscopic ellipsometry and four-point probe measurements are given in Table 1.

Number of Cycles	Thickness (Å)	4PP Resistivity (μΩ-cm)	Ex Situ Ellipsometry Resistivity (μΩ-cm)	In Situ Ellipsometry Resistivity (μΩ-cm)
150	82	148 ± 14	130	118
200	132	135 ± 39	119	110
250	173	131 ± 8	125	105

Table 1. TiN EE-ALD film thickness and resistivity for TiN EE-ALD films grown using 150, 200 and 250 EE-ALD cycles. TiN EE-ALD films were grown on SiO_2 thermal oxide using a pulsing sequence in seconds of (1, 2, 20, 1) with NH_3 background pressure of ~1 mTorr. Resistivity was obtained using four-point probe techniques and ex situ and in situ ellipsometry measurements.

There is good agreement between all the resistivity values indicating that the in situ ellipsometry results shown in Figure 4-12 are reliable.

The TiN EE-ALD film deposits on insulating as well as on conducting samples. Electron currents on an insulating substrate might be expected to charge the substrate negatively. This negative charge would then repel additional electron current. However, if the secondary electron yield is greater than unity, then the sample would charge positive. This positive charge could then pull back secondary electrons to maintain charge neutrality. Secondary electron yields greater than unity have been measured for SiO_2 and Si_3N_4 for primary electron energies from ~100-1000 eV.[5, 135] A wide range of insulating materials, such as Al_2O_3, also have secondary electron yields greater than unity.[136-138] These high secondary electron yields should allow EE-ALD to be performed on insulating substrates.

4.5 Conclusions

TiN EE-ALD was performed using sequential exposures of TDMAT and low energy electrons with a continuous NH_3 reactive background gas (RBG). The TiN EE-ALD was conducted utilizing a hollow cathode plasma electron source (HC-PES) that can deliver a high electron flux into background gases at pressures up to several mTorr. TiN EE-ALD films were grown at temperatures of 30-70 °C using electron energies of ≤100 eV and a NH_3 RBG pressure of ~1 mTorr. Electron scattering in the background gas is not a problem until higher pressures of >5 mTorr.

Rapid nucleation of the TiN EE-ALD films was achieved on a variety of substrates including a native oxide on silicon, an SiO_2 thermal oxide and an in situ deposited silicon nitride film. Growth per cycle (GPC) values of 0.75 to 1.8 Å per cycle were measured using in situ 4-wavelength ellipsometry for different precursor exposures. TiN EE-ALD was accomplished on insulating substrates such as an SiO_2 thermal oxide with a thickness of 400 nm. The TiN EE-ALD is thought to be achievable on insulating substrates because the secondary electron yield at electron energies of ~100 eV is greater than unity.

The TiN EE-ALD films were high purity and slightly nitrogen-rich as demonstrated by in situ AES studies and ex situ XPS measurements. Low resistivities of ~120 μΩ-cm for the TiN films with thicknesses of ≥60 Å were measured using in situ ellipsometry analysis. Ex situ four-point probe measurements and spectroscopic ellipsometry confirmed these low resistivities. The TiN films were crystalline as determined by X-ray diffraction investigations. X-ray reflectivity studies also revealed that the thin TiN films had densities similar to bulk TiN films.

The high quality of the TiN EE-ALD films was attributed to the presence of the NH_3 RBG. The low energy electrons and the NH_3 RBG are believed to interact to form $\bullet NH_2$ and $\bullet H$ radical species. These radical species can react with the growing surface during TiN EE-ALD and improve the film purity. The reactive $\bullet NH_2$ and $\bullet H$ species, together with the incident electron flux leading to electron stimulated desorption, facilitate the low temperature growth and high purity of the TiN EE-ALD films. Many other RBGs will be able to extend the possibilities for tuning film composition and properties during EE-ALD.

5 References

1. George, S. M., Atomic Layer Deposition: An Overview. *Chem Rev* **2010,** *110* (1), 111-31.

2. Johnson, R. W.; Hultqvist, A.; Bent, S. F., A Brief Review Of Atomic Layer Deposition: From Fundamentals To Applications. *Materials Today* **2014,** *17* (5), 236-246.

3. Puurunen, R. L., Surface Chemistry Of Atomic Layer Deposition: A Case Study For The Trimethylaluminum/Water Process. *Journal of Applied Physics* **2005,** *97* (12), 121301.

4. Myers, T. J.; Throckmorton, J. A.; Borrelli, R. A.; O'Sullivan, M.; Hatwar, T.; George, S. M., Smoothing Surface Roughness Using Al2O3 Atomic Layer Deposition. *Applied Surface Science* **2021,** *569*, 150878.

5. Fijol, J. J.; Then, A. M.; Tasker, G. W.; Soave, R. J., Secondary Electron Yield of SiO_2 and Si_3N_4 Thin Films for Continuous Dynode Electron Multipliers. *Appl. Surf. Sci.* **1991,** *48-9*, 464-471.

6. Groner, M. D.; Fabreguette, F. H.; Elam, J. W.; George, S. M., Low-Temperature Al2O3 Atomic Layer Deposition. *Chemistry of Materials* **2004,** *16* (4), 639-645.

7. Higashi, G. S.; Fleming, C. G., Sequential surface chemical reaction limited growth of high quality Al_2O_3 dielectrics. *Applied Physics Letters* **1989,** *55* (19), 1963-1965.

8. De Teresa, J. M.; Córdoba, R.; Fernández-Pacheco, A.; Montero, O.; Strichovanec, P.; Ibarra, M. R., Origin of the Difference in the Resistivity of As-Grown Focused-Ion- and Focused-Electron-Beam-Induced Pt Nanodeposits. *Journal of Nanomaterials* **2009,** *2009*, 936863.

9. Junige, M.; Loffler, M.; Geidel, M.; Albert, M.; Bartha, J. W.; Zschech, E.; Rellinghaus, B.; Dorp, W. F. V., Area-selective atomic layer deposition of Ru on electron-beam-written Pt(C) patterns versus SiO2 substratum. *Nanotechnology* **2017,** *28* (39), 395301.

10. De Teresa, J. M.; Fernández-Pacheco, A.; Córdoba, R.; Serrano-Ramón, L.; Sangiao, S.; Ibarra, M. R., Review of magnetic nanostructures grown by focused electron beam induced deposition (FEBID). *Journal of Physics D: Applied Physics* **2016,** *49* (24).

11. Thorman, R. M.; Kumar, T. P. R.; Fairbrother, D. H.; Ingolfsson, O., The Role of Low-Energy Electrons in Focused Electron Beam Induced Deposition: Four Case Studies of Representative Precursors. *Beilstein J Nanotechnol* **2015,** *6*, 1904-26.

12. Engmann, S.; Stano, M.; Matejcik, S.; Ingolfsson, O., The Role of Dissociative Electron Attachment in Focused Electron Beam Induced Processing: A Case Study on Cobalt Tricarbonyl Nitrosyl. *Angew Chem Int Ed Engl* **2011,** *50* (40), 9475-7.

13. Gazzadi, G. C.; Mulders, H.; Trompenaars, P.; Ghirri, A.; Affronte, M.; Grillo, V.; Frabboni, S., Focused Electron Beam Deposition of Nanowires from Cobalt Tricarbonyl Nitrosyl ($Co(CO)_3NO$) Precursor. *The Journal of Physical Chemistry C* **2011,** *115* (40), 19606-19611.

14. Utke, I.; Hoffmann, P.; Melngailis, J., Gas-Assisted Focused Electron Beam And Ion Beam Processing And Fabrication. *Journal of Vacuum Science & Technology B: Microelectronics and Nanometer Structures* **2008,** *26* (4), 1197-1276.

15. van Dorp, W. F.; Hagen, C. W., A Critical Literature Review Of Focused Electron Beam Induced Deposition. *Journal of Applied Physics* **2008,** *104* (8), 081301.

16. Walz, M.-M.; Schirmer, M.; Vollnhals, F.; Lukasczyk, T.; Steinrück, H.-P.; Marbach, H., Electrons as "Invisible Ink": Fabrication of Nanostructures by Local Electron Beam Induced Activation of SiOx. *Angewandte Chemie International Edition* **2010,** *49* (27), 4669-4673.

17. Tilmann, H.; Michael, W.; Renzo, C.; Horst, S.; Laura, A.; Fan, T.; Johannes, S.; Hubertus, M., Pushing the limits of EUV mask repair: addressing sub-10 nm defects with the next generation e-beam-based mask repair tool. *Journal of Micro/Nanopatterning, Materials, and Metrology* **2021,** *20* (3), 031013.

18. Drost, M.; Tu, F.; Berger, L.; Preischl, C.; Zhou, W.; Gliemann, H.; Wöll, C.; Marbach, H., Surface-Anchored Metal–Organic Frameworks as Versatile Resists for Gas-Assisted E-Beam Lithography: Fabrication of Sub-10 Nanometer Structures. *ACS Nano* **2018,** *12* (4), 3825-3835.

19. Perentes, A.; Hoffmann, P., Focused Electron Beam Induced Deposition of Si-based Materials from SiO_xC_y to Stoichiometric SiO_2: Chemical Compositions, Chemical-Etch Rates, and Deep Ultraviolet Optical Transmissions. *Chem. Vap. Deposition* **2007,** *13*, 176-184.

20. Botman, A.; de Winter, D. A. M.; Mulders, J. J. L., Electron-Beam-Induced Deposition Of Platinum At Low Landing Energies. *Journal of Vacuum Science & Technology B: Microelectronics and Nanometer Structures* **2008,** *26* (6), 2460-2463.

21. van Dorp, W. F.; Wnuk, J. D.; Gorham, J. M.; Fairbrother, D. H.; Madey, T. E.; Hagen, C. W., Electron Induced Dissociation Of Trimethyl (Methylcyclopentadienyl) Platinum (Iv): Total Cross Section As A Function Of Incident Electron Energy. *Journal of Applied Physics* **2009,** *106* (7), 074903.

22. Miyazoe, H.; Utke, I.; Kikuchi, H.; Kiriu, S.; Friedli, V.; Michler, J.; Terashima, K., Improving The Metallic Content Of Focused Electron Beam-Induced Deposits By A Scanning Electron Microscope Integrated Hydrogen-Argon Microplasma Generator. *Journal of Vacuum Science & Technology B, Nanotechnology and Microelectronics: Materials, Processing, Measurement, and Phenomena* **2010,** *28* (4), 744-750.

23. Rosenberg, S. G.; Barclay, M.; Fairbrother, D. H., Electron induced reactions of surface adsorbed tungsten hexacarbonyl (W(CO)6). *Physical Chemistry Chemical Physics* **2013,** *15* (11), 4002-4015.

24. Rosenberg, S. G.; Barclay, M.; Fairbrother, D. H., Electron Beam Induced Reactions of Adsorbed Cobalt Tricarbonyl Nitrosyl (Co(CO)3NO) Molecules. *The Journal of Physical Chemistry C* **2013,** *117* (31), 16053-16064.

25. Menzel, D.; Gomer, R., Desorption from Metal Surfaces by Low-Energy Electrons. *The Journal of Chemical Physics* **1964,** *41* (11), 3311-3328.

26. Feibelman, P. J.; Knotek, M. L., Reinterpretation Of Electron-Stimulated Desorption Data From Chemisorption Systems. *Physical Review B* **1978,** *18* (12), 6531-6539.

27. Knotek, M. L.; Feibelman, P. J., Ion Desorption by Core-Hole Auger Decay. *Physical Review Letters* **1978,** *40* (14), 964-967.

28. Seah, M. P.; Dench, W. A., Quantitative electron spectroscopy of surfaces: A standard data base for electron inelastic mean free paths in solids. *Surface and Interface Analysis* **1979,** *1* (1), 2-11.

29. Biemann, K., Mass Spectrometry. *Annual Review of Biochemistry* **1963,** *32* (1), 755-780.

30. Sprenger, J. K.; Sun, H.; Cavanagh, A. S.; George, S. M., Electron-Enhanced Atomic Layer Deposition of Silicon Thin Films at Room Temperature. *J. Vac. Sci. Technol. A* **2018,** *36*, 01A118.

31. Shawrav, M. M.; Taus, P.; Wanzenboeck, H. D.; Schinnerl, M.; Stöger-Pollach, M.; Schwarz, S.; Steiger-Thirsfeld, A.; Bertagnolli, E., Highly Conductive and Pure Gold Nanostructures Grown by Electron Beam Induced Deposition. *Sci. Rep.* **2016,** *6*, 1-10.

32. Haider, A.; Yilmaz, M.; Deminskyi, P.; Eren, H.; Biyikli, N., Nanoscale Selective Area Atomic Layer Deposition of TiO_2 Using E-beam Patterned Polymers. *RSC Advances* **2016,** *6*, 106109-106119.

33. Rohdenburg, M.; Fröch, J. E.; Martinović, P.; Lobo, C. J.; Swiderek, P., Combined Ammonia and Electron Processing of a Carbon-Rich Ruthenium Nanomaterial Fabricated by Electron-Induced Deposition. *Micromachines* **2020,** *11* (8), 769.

34. Regolini, J. L.; Bensahel, D.; Mercier, J.; Scheid, E., Silicon selective epitaxial growth at reduced pressure and temperature. *Journal of Crystal Growth* **1989,** *96* (3), 505-512.

35. Sobell, Z. C.; Cavanagh, A. S.; Boris, D. R.; Walton, S. G.; George, S. M., Hollow Cathode Plasma Electron Source for Low Temperature Deposition of Cobalt Films by Electron-Enhanced Atomic Layer Deposition. *J. Vac. Sci. Technol. A* **2021,** *39*, 042403.

36. Sobell, Z. C.; Cavanagh, A. S.; George, S. M., Growth Of Cobalt Films At Room Temperature Using Sequential Exposures Of Cobalt Tricarbonyl Nitrosyl And Low Energy Electrons. *Journal of Vacuum Science & Technology A* **2019,** *37* (6).

37. Filmsense What is Ellipsometry. https://film-sense.com/ellipsometry-technology/#ellipsometry.

38. Woollam, J. A. Ellipsometry FAQ - J.A. Woollam. https://www.jawoollam.com/resources/ellipsometry-faq#toggle-id-2.

39. Van Bui, H.; Kovalgin, A. Y.; Wolters, R. A. M., On the Difference Between Optically and Electrically Determined Resistivity of Ultra-Thin Titanium Nitride Films. *Appl. Surf. Sci.* **2013,** *269*, 45-49.

40. Langereis, E.; Heil, S. B. S.; Van De Sanden, M. C. M.; Kessels, W. M. M., In situ Spectroscopic Ellipsometry Study on the Growth of Ultrathin TiN Films by Plasma-Assisted Atomic Layer Deposition. *J. Appl. Phys.* **2006,** *100*, 023534.

41. Chang, C. C., Auger electron spectroscopy. *Surface Science* **1971,** *25* (1), 53-79.

42. Pletincx, S. Study of the encapsulation of healing agents for autonomous self-healing coatings. 2014.

43. Chason, E.; Mayer, T. M., Thin film and surface characterization by specular X-ray reflectivity. *Critical Reviews in Solid State and Materials Sciences* **1997,** *22* (1), 1-67.

44. Parratt, L. G., Surface Studies of Solids by Total Reflection of X-Rays. *Physical Review* **1954,** *95* (2), 359-369.

45. Pope, C. G., X-Ray Diffraction and the Bragg Equation. *Journal of Chemical Education* **1997,** *74* (1), 129.

46. Baskaran, S. Structure and Regulation of Yeast Glycogen Synthase. Indiana University, 2010.

47. Segmüller, A.; Noyan, I. C.; Speriosu, V. S., X-ray diffraction studies of thin films and multilayer structures. *Progress in Crystal Growth and Characterization* **1989,** *18*, 21-66.

48. Hollander, J. M.; Jolly, W. L., X-ray photoelectron spectroscopy. *Accounts of Chemical Research* **1970,** *3* (6), 193-200.

49. Physical Electronics, I. XPS/ESCA. https://www.phi.com/surface-analysis-techniques/xps-esca.html.

50. Biesinger, M. C.; Payne, B. P.; Grosvenor, A. P.; Lau, L. W. M.; Gerson, A. R.; Smart, R. S. C., Resolving Surface Chemical States In Xps Analysis Of First Row Transition Metals, Oxides And Hydroxides: Cr, Mn, Fe, Co And Ni. *Applied Surface Science* **2011,** *257* (7), 2717-2730.

51. Wang, X.; Ramirez-Hinestrosa, S.; Dobnikar, J.; Frenkel, D., The Lennard-Jones potential: when (not) to use it. *Phys Chem Chem Phys* **2020,** *22* (19), 10624-10633.

52. Systems, P. True Non-Contact Mode. https://www.parksystems.com/index.php/park-spm-modes/91-standard-imaging-mode/217-true-non-contact-mode (accessed 2022).

53. Lauritsen, J. V.; Reichling, M., Atomic resolution non-contact atomic force microscopy of clean metal oxide surfaces. *Journal of Physics: Condensed Matter* **2010,** *22* (26), 263001.

54. Smits, F. M., Measurement of Sheet Resistivities with the Four-Point Probe. *Bell System Technical Journal* **1958,** *37* (3), 711-718.

55. van Dorp, W. F.; Beyer, A.; Mainka, M.; Golzhauser, A.; Hansen, T. W.; Wagner, J. B.; Hagen, C. W.; De Hosson, J. T., Focused Electron Beam Induced Processing And The Effect Of Substrate Thickness Revisited. *Nanotechnology* **2013,** *24* (34), 345301.

56. Sprenger, J. K.; Sun, H.; Cavanagh, A. S.; George, S. M., Electron-Enhanced Atomic Layer Deposition of Silicon Thin Films at Room Temperature. *J. Vac. Sci. Technol. A* **2017,** *36*, 01A118.

57. Sprenger, J. K.; Sun, H.; Cavanagh, A. S.; Roshko, A.; Blanchard, P. T.; George, S. M., Electron-Enhanced Atomic Layer Deposition of Boron Nitride Thin Films at Room Temperature and 100 °C. *The Journal of Physical Chemistry C* **2018,** *122* (17), 9455-9464.

58. Bekiaris, N.; Wu, Z.; Ren, H.; Naik, M.; Park, J. H.; Lee, M.; Ha, T. H.; Hou, W.; Bakke, J. R.; Gage, M.; Wang, Y.; Tang, J., Cobalt Fill for Advanced Interconnects. *Proceedings of 2017 IEEE International Interconnect Technology Conference (IITC), Hsinchu, Taiwan, May 16-18, 2017.* **2017**.

59. Wu, J.; F., W.; Branagan, S.; Suzuki, H.; van Eisden, J., Mechanism of Cobalt Bottom-Up Filling for Advanced Node Interconnect Metallization. *J. Electrochem. Soc.* **2019,** *166*, D3136-D3141.

60. Ivanova, A. R.; Nuesca, G.; Chen, X.; Goldberg, C.; Kaloyeros, A. E.; Arkles, B.; Sullivan, J. J., The Effects of Processing Parameters in the Chemical Vapor Deposition of Cobalt from Cobalt Tricarbonyl Nitrosyl. *Journal of The Electrochemical Society* **2019,** *146* (6), 2139-2145.

61. Lane, P. A.; E.Oliver, P.; Wright, P. J.; Reeves, C. L.; Pitt, A. D.; Cockayne, B., Metal Organic CVD of Cobalt Thin Films Using Cobalt Tricarbonyl Nitrosyl. *Chemical Vapor Deposition* **1998,** *04* (05), 183-186.

62. Vollnhals, F.; Drost, M.; Tu, F.; Carrasco, E.; Spath, A.; Fink, R. H.; Steinruck, H. P.; Marbach, H., Electron-Beam Induced Deposition And Autocatalytic Decomposition Of Co(CO)3NO. *Beilstein J Nanotechnol* **2014,** *5*, 1175-85.

63. Postler, J.; Renzler, M.; Kaiser, A.; Huber, S. E.; Probst, M.; Scheier, P.; Ellis, A. M., Electron-Induced Chemistry of Cobalt Tricarbonyl Nitrosyl (Co(CO)3NO) in Liquid Helium Nanodroplets. *J Phys Chem C Nanomater Interfaces* **2015,** *119* (36), 20917-20922.

64. Opitz, J., Electron Impact Ionization Of Cobalt-Tricarbonyl-Nitrosyl, Cyclopentadienyl-Cobalt-Dicarbonyl And Biscyclopentadienyl-Cobalt: Appearance Energies, Bond Energies And Enthalpies Of Formation. *International Journal of Mass Spectrometry* **2003,** *225* (2), 115-126.

65. Papp, P.; Engmann, S.; Kučera, M.; Stano, M.; Matejčík, Š.; Ingólfsson, O., An Experimental And Theoretical Study On Structural Parameters And Energetics In Ionization And Dissociation Of Cobalt Tricarbonyl Nitrosyl. *International Journal of Mass Spectrometry* **2013,** *356*, 24-32.

66. Engmann, S.; Stano, M.; Papp, P.; Brunger, M. J.; Matejcik, S.; Ingolfsson, O., Absolute Cross Sections For Dissociative Electron Attachment And Dissociative Ionization Of Cobalt Tricarbonyl Nitrosyl In The Energy Range From 0 Ev To 140 Ev. *J Chem Phys* **2013,** *138* (4), 044305.

67. Venables, J. A., Atomic processes in crystal growth. *Surface Science* **1994,** *299-300* (1-3), 798-817.

68. Baker, L.; Cavanagh, A. S.; Seghete, D.; George, S. M.; Mackus, A. J. M.; Kessels, W. M. M.; Liu, Z. Y.; Wagner, F. T., Nucleation And Growth Of Pt Atomic Layer Deposition On Al2O3 Substrates Using (Methylcyclopentadienyl)-Trimethyl Platinum And O2 Plasma. *Journal of Applied Physics* **2011,** *109* (8).

69. Oks, E. M.; Schanin, P. M., Development Of Plasma Cathode Electron Guns. *Physics of Plasmas* **1999,** *6* (5), 1649-1654.

70. Mulders, J. J.; Belova, L. M.; Riazanova, A., Electron Beam Induced Deposition At Elevated Temperatures: Compositional Changes And Purity Improvement. *Nanotechnology* **2011,** *22* (5), 055302.

71. Briggs, D.; Gibson, V. A., Direct observation of multiplet splitting in 2P photoelectron peaks of cobalt complexes. *Chemical Physics Letters* **1974,** *25* (4), 493-496.

72. Smentkowski, V. S., Trends In Sputtering. *Progress in Surface Science* **2000,** *64* (1-2), 1-58.

73. Madey, T. E.; Yates, J. T., Electron-Stimulated Desorption as a Tool for Studies of Chemisorption: A Review. *J. Vac. Sci. Technol.* **1971,** *8* (4), 525-555.

74. Madey, T. E., Electron- and photon-stimulated desorption: probes of structure and bonding at surfaces. *Science* **1986,** *234* (4774), 316-22.

75. Allen, T. E., Monte Carlo calculation of low-energy electron emission from surfaces. *Journal of Vacuum Science & Technology B: Microelectronics and Nanometer Structures* **1988,** *6* (6), 2057-2060.

76. van Dorp, W. F., The Role Of Electron Scattering In Electron-Induced Surface Chemistry. *Phys Chem Chem Phys* **2012,** *14* (48), 16753-9.

77. Goh, K. E. J.; Chen, S.; Xu, H.; Ballard, J.; Randall, J. N.; Von Ehr, J. R., Using Patterned H-Resist For Controlled Three-Dimensional Growth Of Nanostructures. *Applied Physics Letters* **2011,** *98* (16), 163102.

78. Owen, J. H. G.; Ballard, J.; Randall, J. N.; Alexander, J.; Von Ehr, J. R., Patterned Atomic Layer Epitaxy of Si/Si(001):H. *Journal of Vacuum Science & Technology B, Nanotechnology and Microelectronics: Materials, Processing, Measurement, and Phenomena* **2011,** *29* (6), 06f201.

79. Feng, Y.; Verboncoeur, J. P., Transition from Fowler-Nordheim field emission to space charge limited current density. *Physics of Plasmas* **2006,** *13* (7).

80. Lau, Y. Y.; Liu, Y.; Parker, R. K., Electron emission: From the Fowler–Nordheim relation to the Child–Langmuir law. *Physics of Plasmas* **1994,** *1* (6), 2082-2085.

81. Bayless, J.; Knechtli, R.; Mercer, G., The Plasma-Cathode Electron Gun. *IEEE Journal of Quantum Electronics* **1974,** *10* (2), 213-218.

82. Cothran, C. D.; Boris, D. R.; Compton, C. S.; Tejero, E. M.; Fernsler, R. F.; Amatucci, W. E.; Walton, S. G., Continuous And Pulsed Electron Beam Production From An Uninterrupted Plasma Cathode. *Surface and Coatings Technology* **2015,** *267*, 111-116.

83. Stockhausen, G.; Kock, M., Proof And Analysis Of The Pendulum Motion Of Beam Electrons In A Hollow Cathode Discharge. *Journal of Physics D: Applied Physics* **2001,** *34* (11), 1683-1689.

84. Oks, E. M., Physics And Technique Of Plasma Electron Sources. *Plasma Sources Science and Technology* **1992,** *1* (4), 249-255.

85. Oks, E., *Plasma Cathode Electron Sources: Physics, Technology, Applications*. Wiley-VCH: Weinheim, 2006.

86. Burdovitsin, V.; Oks, E., Hollow-Cathode Plasma Electron Gun for Beam Generation at Forepump Gas Pressure. *Review of Scientific Instruments* **1999,** *70* (7), 2975-2978.

87. Burdovitsin, V. A.; Oks, E. M., Fore-Vacuum Plasma-Cathode Electron Sources. *Laser and Particle Beams* **2008,** *26* (4), 619-635.

88. Burdovitsin, V. A.; Zhirkov, I. S.; Oks, E. M.; Osipov, I. V.; Fedorov, M. V., A Plasma-Cathode Electron Source for Focused-Beam Generation in the Fore-Pump Pressure Range. *Instruments and Experimental Techniques* **2005,** *48* (6), 761-763.

89. Klimov, A.; Bakeev, I.; Oks, E.; Zenin, A., Forevacuum Plasma Source Of Continuous Electron Beam. *Laser and Particle Beams* **2019,** *37* (2), 203-208.

90. Shchukin, V. G.; Konstantinov, V. O.; Morozov, V. S., High-Efficiency Electron Source with a Hollow Cathode in Technologies of Thin Film Deposition and Surface Treatment under Forevacuum Pressures. *Technical Physics* **2018,** *63* (6), 888-893.

91. Osipov, I.; Rempe, N., A Plasma–Cathode Electron Source Designed For Industrial Use. *Review of Scientific Instruments* **2000,** *71* (4), 1638-1641.

92. Muhl, S.; Pérez, A., The Use Of Hollow Cathodes In Deposition Processes: A Critical Review. *Thin Solid Films* **2015,** *579*, 174-198.

93. Walton, S. G.; Boris, D. R.; Hernández, S. C.; Lock, E. H.; Petrova, T. B.; Petrov, G. M.; Fernsler, R. F., Electron Beam Generated Plasmas for Ultra Low TeProcessing. *ECS Journal of Solid State Science and Technology* **2015,** *4* (6), N5033-N5040.

94. Walton, S. G.; Boris, D. R.; Hernández, S. C.; Lock, E. H.; Petrova, T. B.; Petrov, G. M.; Jagtiani, A. V.; Engelmann, S. U.; Miyazoe, H.; Joseph, E. A., Electron Beam Generated Plasmas: Characteristics And Etching Of Silicon Nitride. *Microelectronic Engineering* **2017,** *168*, 89-96.

95. Li, C.; Godyak, V.; Hofmann, T.; Edinger, K.; Oehrlein, G. S., Electron Beam Injection From A Hollow Cathode Plasma Into A Downstream Reactive Environment: Characterization Of Secondary Plasma Production And Si3N4 And Si Etching. *Journal of Vacuum Science & Technology A* **2020,** *38* (3).

96. Bárdoš, L., Radio Frequency Hollow Cathodes For The Plasma Processing Technology. *Surface and Coatings Technology* **1996,** *86-87* (1-3), 648-656.

97. Boris, D. R.; Cothran, C. D.; Compton, C. S.; Amatucci, W. E.; Walton, S. G., On the Mechanism of Pulsed Electron Beam Production From an Uninterrupted Plasma Cathode. *IEEE Transactions on Plasma Science* **2016,** *44* (5), 761-768.

98. Baalrud, S. D.; Hershkowitz, N.; Longmier, B., Global Nonambipolar Flow: Plasma Confinement Where All Electrons Are Lost To One Boundary And All Positive Ions To Another Boundary. *Physics of Plasmas* **2007,** *14* (4), 042109.

99. Laegreid, N.; Wehner, G. K., Sputtering Yields of Metals for Ar+ and Ne+ Ions with Energies from 50 to 600 ev. *Journal of Applied Physics* **1961,** *32* (3), 365-369.

100. Boris, D. R.; Cothran, C. D.; Compton, C. S.; Amatucci, W. E.; Walton, S. G., On the Mechanism of Pulsed Electron Beam Production From an Uninterrupted Plasma Cathode. *IEEE Trans. Plasma Sci.* **2016,** *44* (5), 761-768.

101. Sobell, Z. C.; Cavanagh, A. S.; George, S. M., Growth of cobalt films at room temperature using sequential exposures of cobalt tricarbonyl nitrosyl and low energy electrons. *J. Vac. Sci. Technol. A* **2019,** *37* (6).

102. Sprenger, J. K.; Cavanagh, A. S.; Sun, H.; Wahl, K. J.; Roshko, A.; George, S. M., Electron Enhanced Growth of Crystalline Gallium Nitride Thin Films at Room Temperature and 100 °C Using Sequential Surface Reactions. *Chem. Mater.* **2016,** *28* (15), 5282-5294.

103. Sprenger, J. K.; Sun, H. X.; Cavanagh, A. S.; Roshko, A.; Blanchard, P. T.; George, S. M., Electron-Enhanced Atomic Layer Deposition of Boron Nitride Thin Films at Room Temperature and 100 degrees C. *J. Phys. Chem. C* **2018,** *122* (17), 9455-9464.

104. Baker, L.; Cavanagh, A. S.; Seghete, D.; George, S. M.; Mackus, A. J. M.; Kessels, W. M. M.; Liu, Z. Y.; Wagner, F. T., Nucleation and growth of Pt atomic layer deposition on Al2O3 substrates using (methylcyclopentadienyl)-trimethyl platinum and O-2 plasma. *J. Appl. Phys.* **2011,** *109* (8).

105. Elam, J. W.; Zinovev, A.; Han, C. Y.; Wang, H. H.; Welp, U.; Hryn, J. N.; Pellin, M. J., Atomic layer deposition of palladium films on Al2O3 surfaces. *Thin Solid Films* **2006,** *515* (4), 1664-1673.

106. Hamalainen, J.; Ritala, M.; Leskela, M., Atomic Layer Deposition of Noble Metals and Their Oxides. *Chem. Mater.* **2014,** *26* (1), 786-801.

107. Sobell, Z. C.; Cavanagh, A. S.; George, S. M., Growth of Cobalt Films at Room Temperature Using Sequential Exposures of Cobalt Tricarbonyl Nitrosyl and Low Energy Electrons. *J. Vac. Sci. Technol. A* **2019,** *37*, 060906.

108. Sprenger, J. K.; Cavanagh, A. S.; Sun, H.; Wahl, K. J.; Roshko, A.; George, S. M., Electron Enhanced Growth of Crystalline Gallium Nitride Thin Films at Room Temperature and 100°C Using Sequential Surface Reactions. *Chem. Mater.* **2016,** *28*, 5282-5294.

109. Sprenger, J. K.; Sun, H.; Cavanagh, A. S.; Roshko, A.; Blanchard, P. T.; George, S. M., Electron-Enhanced Atomic Layer Deposition of Boron Nitride Thin Films at Room Temperature and 100°C. *J. Phys. Chem. C* **2018,** *122*, 9455-9464.

110. Uhm, J.; Jeon, H., TiN Diffusion Barrier Grown by Atomic Layer Deposition Method for Cu Metallization. *Jpn. J. Appl. Phys., Part 1* **2001,** *40*, 4657-4660.

111. Rha, S. K.; Lee, W. J.; Lee, S. Y.; Hwang, Y. S.; Lee, Y. J.; Kim, D. I.; Kim, D. W.; Chun, S. S.; Park, C. O., Improved TiN Film as a Diffusion Barrier Between Copper and Silicon. *Thin Solid Films* **1998,** *320*, 134-140.

112. Wang, S. Q.; Raaijmakers, I.; Burrow, B. J.; Suthar, S.; Redkar, S.; Kim, K. B., Reactively Sputtered TiN as a Diffusion Barrier between Cu and Si. *J. Appl. Phys.* **1990,** *68*, 5176-5187.

113. Weber, E. R., Transition Metals in Silicon. *Appl. Phys. A* **1983,** *30*, 1-22.

114. McBrayer, J. D.; Swanson, R. M.; Sigmon, T. W., Diffusion of Metals in Silicon Dioxide. *J. Electrochem. Soc.* **1986,** *133*, 1242-1246.

115. Gall, D., Electron Mean Free Path in Elemental Metals. *J. Appl. Phys.* **2016,** *119*, 085101.

116. Gall, D., The Search for the Most Conductive Metal for Narrow Interconnect Lines. *J. Appl. Phys.* **2020,** *127*, 050901.

117. Paranjpe, A.; IslamRaja, M., Chemical Vapor Deposition TiN Process for Contact/Via Barrier Applications. *J. Vac. Sci. Technol. B* **1995,** *13*, 2105-2114.

118. Zhao, C.; Xiang, J., Atomic Layer Deposition (ALD) of Metal Gates for CMOS. *Appl. Sci.* **2019,** *9* (11), 2388.

119. Elers, K. E.; Saanila, V.; Soininen, P. J.; Li, W. M.; Kostamo, J. T.; Haukka, S.; Juhanoja, J.; Besling, W. F. A., Diffusion Barrier Deposition on a Copper Surface by Atomic Layer Deposition. *Chem. Vap. Deposition* **2002,** *8*, 149-153.

120. Elam, J. W.; Schuisky, M.; Ferguson, J. D.; George, S. M., Surface Chemistry and Film Growth during TiN Atomic Layer Deposition Using TDMAT and NH_3. *Thin Solid Films* **2003,** *436*, 145-156.

121. Musschoot, J.; Xie, Q.; Deduytsche, D.; Van den Berghe, S.; Van Meirhaeghe, R. L.; Detavernier, C., Atomic Layer Deposition of Titanium Nitride from TDMAT Precursor. *Microelectron. Eng.* **2009,** *86*, 72-77.

122. Tiznado, H.; Zaera, F., Surface Chemistry in the Atomic Layer Deposition of TiN Films from $TiCl_4$ and Ammonia. *J. Phys. Chem. B* **2006,** *110*, 13491-13498.

123. Wolf, S.; Breeden, M.; Kwak, I.; Park, J. H.; Kavrik, M.; Naik, M.; Alvarez, D.; Spiegelman, J.; Kummel, A. C., Low Temperature Thermal ALD TaN_x and TiN_x Films from Anhydrous N_2H_4. *Appl. Surf. Sci.* **2018,** *462*, 1029-1035.

124. Wang, L.; Liu, B.; Song, Z.; Feng, S.; Zhou, Z.; Xiang, Y.; Zhang, F., Atomic Vapor Deposition of TiN with Diluted Tetrakis (diethylamido) Titanium (TDEAT) for Phase Change Memory. *ECS Transactions* **2009,** *22*, 167-173.

125. Chen, Z. X.; Li, X.; Li, W. M.; Lo, G. Q., Plasma-Enhanced Atomic Layer Deposition (PEALD) of TiN using the Organic Precursor Tetrakis(ethylmethylamido)Titanium (TEMAT). *MATEC Web of Conferences* **2016,** *39*, 1-3.

126. Profijt, H. B.; Potts, S. E.; van de Sanden, M. C. M.; Kessels, W. M. M., Plasma-Assisted Atomic Layer Deposition: Basics, Opportunities, and Challenges. *J. Vac. Sci. Technol. A* **2011,** *29*, 050801.

127. Anz, S. J.; Margolese, D. I.; Sando, S. F.; Gillis, H. P.; Goddard, W. A., Damage-Free Atomic-Scale Etching and Surface Enhancements by Electron-Enhanced Reactions: Results and Simulations. *Springer Ser. Mater. Sci.* **2021,** *284*, 603-627.

128. Itikawa, Y., Cross Sections for Electron Collisions with Ammonia. *J. Phys. Chem. Ref. Data* **2017,** *46*, 043103.

129. Raju, G. G., Electron-Atom Collision Cross Sections in Argon: An Analysis and Comments. *IEEE Trans. Dielectr. Electr. Insul.* **2004,** *11* (4), 649-673.

130. Tiwald, T. E.; Thompson, D. W.; Woollam, J. A.; Paulson, W.; Hance, R., Application of IR Variable Angle Spectroscopic Ellipsometry to the Determination of Free Carrier Concentration Depth Profiles. *Thin Solid Films* **1998,** *313*, 661-666.

131. Okada, L. A.; George, S. M., Adsorption and Desorption Kinetics of Tetrakis(dimethylamino)titanium and Dimethylamine on TiN Surfaces. *Appl. Surf. Sci.* **1999,** *137*, 113-124.

132. Muthukumar, K.; Jeschke, H. O.; Valentí, R.; Begun, E.; Schwenk, J.; Porrati, F.; Huth, M., Spontaneous Dissociation of $Co_2(CO)_8$ and Autocatalytic Growth of Co on SiO_2: A Combined Experimental and Theoretical Investigation. *Beilstein J. Nanotechnol.* **2012,** *3*, 546-555.

133. Jain, A.; Ong, S. P.; Hautier, G.; Chen, W.; Richards, W. D.; Dacek, S.; Cholia, S.; Gunter, D.; Skinner, D.; Ceder, G.; Persson, K. A., (Card 00-000-0492) in Commentary: The Materials Project: A Materials Genome Approach to Accelerating Materials Innovation. *APL Mater.* **2013,** *1* (1), 011002.

134. Behera, A. K.; Viswanath, R. N.; Lakshmanan, C.; Polaki, S. R.; Sarguna, R. M.; Mathews, T., Thermal Oxidation and Nitridation of Si Nanowalls Prepared by Metal Assisted Chemical Etching. *AIP Conf. Proc.* **2018,** *1942*, 050062.

135. Dionne, G. F., Origin of Secondary Electron Emission Yield Curve Parameters. *J. Appl. Phys.* **1975,** *02173*, 3347-3351.

136. Insepov, Z.; Ivanov, V.; Jokela, S. J.; Veryovkin, I.; Zinovev, A.; Frisch, H., Comparison of Secondary Electron Emission Simulation to Experiment. *Nucl. Instrum. Methods Phys. Res., Sect. A* **2011,** *639*, 155-157.

137. Seiler, H., Secondary Electron Emission in the Scanning Electron Microscope. *J. Appl. Phys.* **1983,** *54*, R1-R18.

138. Tao, S. X.; Chan, H. W.; van der Graaf, H., Secondary Electron Emission Materials for Transmission Dynodes in Novel Photomultipliers: A Review. *Materials* **2016,** *9* (12), 1017.